# IMPROVED NITRIDE-BASED DEVICE PERFORMANCE: AN EPITAXIAL GROWTH APPROACH

By

SEAN DONOVAN

A DISSERTATION PRESENTED TO THE GRADUATE SCHOOL
OF THE UNIVERSITY OF FLORIDA IN PARTIAL FULFILLMENT
OF THE REQUIREMENTS FOR THE DEGREE OF
DOCTOR OF PHILOSOPHY

UNIVERSITY OF FLORIDA

1999

ACKNOWLEDGEMENTS

Were it not for the seemingly limitless patience and understanding of Prof. Cammy Abernathy it is unlikely that I would have persisted as a graduate student, much less completed this PhD dissertation. It is extremely rare to encounter an advisor as thoughtful, insightful, inspiring and generous as she is. I feel extraordinarily fortunate to have had the privilege of working for Prof. Abernathy and only hope that I can continue my scientific career in a manner that honors her renowned reputation. It is impossible to overestimate my gratitude to her.

In order to successfully negotiate a project like this, one requires the integration of talent and equipment from several groups. In particular, the efforts of Prof. Fan Ren, Prof. Stephen Pearton, and the staff at the Major Analytical Instrumentation Center (MAIC) should be recognized as they are deeply appreciated. Additionally, assistance from fellow students Devin MacKenzie, Brent Gila, Mark Overberg and K. N. Lee has been invaluable. Thanks also go to Prof. Stan Bates, Prof. Fred Sharifi, and Prof. Rajiv Singh for serving on my committee.

TABLE OF CONTENTS

ACKNOWLEDGMENTS ..... ii

ABSTRACT ..... v

CHAPTERS

1 INTRODUCTION ..... 1

1.1 Motivation ..... 1
1.2 Group III-Nitrides ..... 3
1.3 Scope of Current Work ..... 5

2 OHMIC CONTACTS: AN OVERVIEW ..... 8

2.1 Description of Ohmic Contacts ..... 8
2.2 The Work Function, Φ ..... 9
2.3 Models for Contact Resistance ..... 11
2.4 History of Contacts to III-Nitrides ..... 14
2.4.1 N-Type ..... 14
2.4.2 P-Type ..... 16
2.5 The Intermediate Semiconductor Layer ..... 17

3 EPITAXIAL GROWTH PRINCIPLES AND APPARATUS ..... 20

3.1 Principles of Epitaxy ..... 21
3.2 Models of Nucleation ..... 26
3.3 Heteroepitaxy ..... 28
3.4 Graded Layers ..... 31
3.5 Comparison of Growth Techniques ..... 32
3.5.1 MBE ..... 33
3.5.2 MOCVD ..... 38
3.5.3 MOMBE ..... 41
3.6 The Varian Gas-Source Gen II ..... 42
3.6.1 Vacuum Pumping Systems ..... 42
3.6.2 Sources ..... 43
3.6.3 MOMBE Safety ..... 49
3.6.4 MOMBE Maintenance ..... 51

4 SAMPLE CHARACTERIZATION ..... 53

4.1 Electrical Characterization ..... 53
4.1.1 The Hall Measurement ..... 54
4.1.2 Capacitance-Voltage (C-V) Measurement ..... 56
4.2 Structural Characterization ..... 57
4.2.1 X-ray Diffraction (XRD) ..... 58
4.2.2 Transmission Electron Microscopy (TEM) ..... 61
4.3 Morphological Characterization ..... 64
4.3.1 SEM ..... 64
4.3.2 AFM ..... 67
4.3.3 Profilometry ..... 70
4.4 Compositional Analysis ..... 71
4.4.1 AES ..... 71
4.4.2 SIMS ..... 75

5 InN EPITAXIAL GROWTH ..... 76

5.1 History of InN Growth ..... 76
5.2 Role of Nitrogen Plasma and Substrate Temperature ..... 80
5.2.1 Sample Loading ..... 80
5.2.2 Sample Growth ..... 81
5.3 Substrate Effects ..... 91
5.4 Indium Precursor ..... 100
5.4.1 TMI Derived InN ..... 102
5.4.2 Solution TMI Derived InN ..... 105
5.4.3 Solid In Derived InN ..... 106
5.5 Summary of InN Growth ..... 109

6 CONTACT STRUCTURES AND PERFORMANCE ..... 113

6.1 Contacts to n-Type Nitride Films ..... 113
6.2 Thermal Stability of n-Type Contact Structures ..... 121

7 NITRIDE DEVICE DEVELOPMENT ..... 126

7.1 GaN/AlGaN HBT Growth ..... 126
7.1.1 Comparison of Aluminum Precursors ..... 127
7.1.2 HBT Fabrication and Performance ..... 136
7.2 P-Type Contact Layers Using GaAs ..... 147

8 CONCLUSIONS, IMPLICATIONS, AND FUTURE WORK ..... 154

REFERENCES ..... 157

BIOGRAPHICAL SKETCH ..... 163

Abstract of Dissertation Presented to the Graduate School
of the University of Florida in Partial Fulfillment of the
Requirements for the Degree of Doctor of Philosophy

IMPROVED NITRIDE-BASED DEVICE PERFORMANCE: AN EPITAXIAL GROWTH APPROACH

By

Sean M. Donovan

December 1999

Chairperson: Professor Cammy R. Abernathy
Major Department: Materials Science and Engineering

An exploration of methods for improving nitride-based device performance using epitaxial growth techniques is made. Particular emphasis is placed on lowering the specific contact resistance, $\rho_c$, of devices using an intermediate semiconductor layer (ISL). Analogous to what has been done with GaAs, where contact layers fabricated from InAs are used to improve contact performance, an ISL based on InN has been developed for wide-gap nitride devices. Additional work addressed the issue of impurity contamination during MOCVD growth of GaN/AlGaN heterostructure bipolar transistors (HBTs) by examining the use of an alternative aluminum precursor.

InN layers were deposited with ultra-high vacuum epitaxial techniques using metalorganic, solid and gaseous sources. Growth conditions were optimized to produce

single-crystal films with smooth surface morphologies. This optimization included the use of a nitridation step prior to growth initiation. Nitridation was accomplished by exposing the heated substrate (>875° C) to reactive nitrogen supplied by a vacuum-compatible plasma cell. All InN films, regardless of substrate type or temperature, nitrogen plasma condition, or indium precursor, exhibit as-grown background electron concentrations on the order of $10^{20}/cm^3$. This characteristic precluded the use of InN ISLs for p-type contacts.

Specific contact resistance was measured using the transmission line method with sputter deposited $WSi_x$ metallization. InN contact layers graded from InAlN were found to be thermally stable to anneals of 600° C, with $\rho_c \sim 6 \times 10^{-6}$ $\Omega$-cm$^2$. Intermixing of W with the underlying contact layer degraded contact performance at higher temperatures.

HBT performance is limited by the large resistance in the p-type base region. A solution utilizing p-GaAs contact layers was explored. Unfortunately, hole transport was restricted due to a valence band offset of ~1.8 eV. This led to the investigation of a digital alloy composed of p-GaAs and p-GaN to simulate a graded layer.

Parasitic reactions in the gas phase leads to low MOCVD growth rates of AlGaN relative to its binary components and to increased impurity incorporation that is detrimental to device performance. Examination of an alternative Al precursor, tri-tertiarybutylaluminum, suggests that adducts formed between the Al precursors and $NH_3$ interact with trimethylgallium, scavenging out these growth nutrients.

# CHAPTER 1
# INTRODUCTION

This dissertation examines methods to improve nitride-based device performance using epitaxial growth techniques. In order to maximize the potential of this emerging technology, several issues must be resolved including minimizing contact resistance, minimizing impurity incorporation and achieving abrupt dopant profiles in heterostructure devices. The first two of these issues are addressed in this work.

## 1.1 Motivation

Simple empirical observation suggests that humankind has been subject to an inexorable urge to elucidate the nature of the universe, how best to control it, and the role of humanity therein. These tendencies have given rise to the theory of evolution, identification of DNA as the code of life, and the advent of space exploration, for example. Incidental to this craving for understanding and control has been the development of complex tools such as computers and radio telescopes. These tools consist in part of interconnected semiconductor devices that precisely regulate electrical current. This technology has been extended to include an array of consumer electronic products. The combination of an innate desire for greater scientific understanding and market driven economics creates a demand for, and leads to ever-improved products based on semiconductor devices. Further impetus for improvement is provided by a yearning for military superiority. Since device performance is a function of the material

it is composed of, new semiconductor devices derived from novel materials must be developed in order to satisfy higher performance requirements. Concomitantly, there is a circular relationship between basic research and product development. As technological advances are introduced in the form of better analytical tools, improvements in research are possible which lead to further advances.

Silicon was the first semiconductor material to gain prominence for integrated circuits. It possesses several outstanding features that make it amenable to device applications including dopability, ease of processing, and relative abundance. However, Si is limited by having an indirect bandgap, which eliminates it as a candidate for light emitting devices (LEDs). Also, clock speeds are limited by the mobility of majority carriers (1500 $cm^2/V \cdot s$ for electrons).[1] These limitations led to the development of GaAs based devices. With its direct bandgap and proper alloying with In, Al, and P, light emitters useful to the fiber-optic communications and data storage industries have been achieved. Faster devices are also possible owing to improved electron mobilities (8500 $cm^2/V \cdot s$ ).[1] For most applications, the capabilities afforded by Si and GaAs-based devices are more than adequate. Nonetheless there are areas of performance unreachable by these traditional semiconductor materials. Areas of special interest include high-power (100-2000 kVA) [2] and high-temperature (>300°C) [3] operation and light emission over the entire visible spectrum into UV. Researchers have turned to large bandgap semiconductors such as SiC, II-VI compounds such as ZnSe and the III-nitrides to address these issues.[4,5,6] This dissertation examines the latter group of semiconductors.

## 1.2 The Group III-Nitrides

Elements from group III in the periodic table, especially Al, Ga and In, combined with nitrogen constitute a family of compound semiconductors commonly known as III-N semiconductors, or more simply, nitrides. Table I lists some important materials properties of AlN, GaN and InN. Silicon, GaAs and SiC are included for comparison.

Table I. Important Material Parameters for Electronic Devices.

| | **Band-Gap (eV)** | **Lattice Contstant (Å)** | **Electron Mobility ($cm^2/Vs$)** | **Saturation Velocity ($cm/s \times 10^7$)** | **Breakdown Field ($V/cm \times 10^7$)** |
|---|---|---|---|---|---|
| **Si** | 1.12 | 5.4 | 1500 | 1.0 | 3.0 |
| **GaAs** | 1.42 | 5.65 | 8500 | 1.0 | 6.0 |
| **4-H SiC** | 3.26 | 10.05 (c)<br>3.07 (a) | 1140 (6-H) | 2.0 | 30 |
| **GaN** | 3.4 | 5.19 (c) | 1000 | 2.5 | 50 |
| **AlN** | 6.2 | 4.98 (c) | 135 | 1.4 | - |
| **InN** | 1.9 | 5.7 (c) | 3200 (calc) | 2.5 | - |

Of principal interest are the large band-gap, high saturation velocities and high breakdown fields of the nitrides which can lead to superior device performance over Si and GaAs based technologies. This class of semiconductors possesses excellent thermal stability as well. Further, the direct band-gap of the III-N's permits fabrication of light emitting devices. To date, long lifetime continuous wave operation blue laser diodes have been introduced.[7] Work has also led to the development of UV LED's and laser

diodes as well. [8] Proper selection of alloy composition of $In_xGa_{1-x}N$ can result in optical emission over the full visible spectrum. Figure 1-1 illustrates the possible alloys and band gaps of the wurtzitic nitrides. Included for comparison are other relevant semiconductor systems.

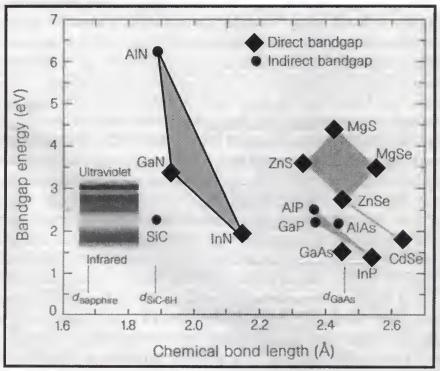


Figure 1-1. Bandgap energy versus bond length for important semiconductors illustrating range of alloy compositions and related optical spectrum.

Owing to their outstanding physical properties, III-nitrides have been intensely studied in recent years as candidates for high power, high frequency and high temperature electronic devices, with the first GaN MESFET reported by Khan *et al.*[9] Such a high level of interest exists that many conference symposia proceedings and other compilations of recent work are routinely published.[10, 11, 12]

As is the case with any emerging technology, the nitrides require improvement in critical areas, especially with ohmic metallization. Metal contacts are an integral part of electronic and optoelectronic devices that allow electrical current to flow into and out of a device with a minimum of power loss. Suitable ohmic contact formation to large band-gap materials such as the III-nitrides is particularly troublesome because high p-dopant activation levels are difficult to achieve. Moreover, interfacial energy barriers to carrier transport arise which are exacerbated as the band-gap increases. A deeper discussion is presented in chapter two. Currently, device performance is hampered by high contact resistance that causes degradation of the contact and reduced operation lifetimes. This degradation arises from $I^2R$ heating at the contact region which promotes spiking of metal through the active region of the device. In order to take full advantage of the high temperature capabilities of the III-Nitrides, thermally stable ohmic contacts must be developed.

## 1.3 Scope of Current Work

This dissertation details research done to improve nitride-based device performance using epitaxial growth techniques. Special emphasis was placed on developing thermally stable ohmic contacts for large bandgap nitrides. Thin semiconductor films of InN were developed for use as an intermediate semiconductor

layer (ISL) as an aid to reducing contact resistance. The bulk of this effort was directed toward optimizing InN film growth using metalorganic molecular beam epitaxy (MOMBE) techniques.

A survey of ohmic contact physical principles is presented in Chapter 2. Models of specific contact resistance are reviewed along with the history of contacts for large bandgap nitrides. The basis for using an InN ISL to improve contact resistance to nitride semiconductors is developed.

Chapter 3 discusses issues pertinent to epitaxial film growth with a description of nucleation and growth models. Comparisons of MOMBE, metalorganic chemical vapor deposition (MOCVD), and molecular beam epitaxy (MBE) growth equipment and techniques are made. A detailed description of the MOMBE system utilized for this work is presented.

Chapter 4 reviews characterization techniques used to analyze samples for this work. Samples were analyzed using scanning electron microscopy (SEM), atomic force microscopy (AFM), secondary ion mass spectroscopy (SIMS), Auger electron spectroscopy (AES), transmission electron microscopy (TEM), x-ray diffraction (XRD) and Hall measurements.

Chapter 5 starts with a review of efforts to develop InN films to date. An investigation of the origin of n-type behavior in as-grown InN is then presented in three parts. First, the effect of varying nitrogen plasma characteristics on electrical properties of InN films is studied. Next, substrate effects such as substrate choice and pregrowth treatment are examined. Finally, the role of In precursor on film characteristics is presented.

Contact performance results based on InN ISLs are presented in Chapter 6. Thermal stability of contact structures is examined for n-type material.

Chapter 7 presents work done to develop nitride-based heterojunction bipolar transistors (HBTs). Growth conditions for the GaN/AlGaN heterostructure are given and an analysis of certain gas phase interactions during growth of AlGaN is made. These interactions reduce the growth rate, allowing increased impurity incorporation. HBT device performance is presented, which is limited by high specific contact resistance in the p-type base region. Experiments with p-GaAs contact layers were conducted in an effort to ameliorate this problem.

Chapter 8 offers conclusions drawn from and implications of this body of work, with suggestions for future research .

# CHAPTER 2
# OHMIC CONTACTS: AN OVERVIEW

This chapter will examine the physical principles of metal-semiconductor interfaces and the basis for constructing ohmic contacts to the large-gap nitrides. A review of work done to date on contacts to GaN is presented to act as a foundation for the current path of investigation.

## 2.1 Description of Ohmic Contacts

In order for a semiconductor device to operate it must be able to accept and emit electrical current. Current is brought into and out of the device by metal wires which are physically attached to the semiconductor device at special contact regions. A successful ohmic contact is one which has a small resistance relative to the device itself and follows the familiar Ohm's Law, V=IR. Contacts of this type will exhibit linear current density (J) vs V behavior around the operating voltage of the device as seen in figure 2-1, curve A. This seemingly straightforward idea is complicated by energy barriers that may exist when a metal and semiconductor are brought into intimate contact and results in rectifying behavior, exhibited in curve B of figure 2-1.

In order to reach thermodynamic equilibrium, the Fermi levels of the metal and semiconductor must come into alignment. This causes the conduction and valence bands to bend at the interface as shown in figure 2-2 for the case of an n-type semiconductor. Note that this is the case for an n-type semiconductor contacted to a metal whose work function is greater than that of the semiconductor, the typical situation for nitrides. There

exists an energy barrier to carrier transport across the interface, $\Phi_B$, defined as the difference in energy between the Fermi level in the metal and the bottom of the conduction band in the semiconductor at the interface. This value is related to the difference in work function between the semiconductor and metal.

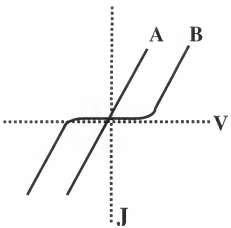


Figure 2-1. Current density versus voltage curves showing Ohmic behavior (A) and rectifying behavior (B).

## 2.2 The Work Function, $\Phi$

The work function of a material is defined as the difference between that material's Fermi energy and ionization energy. This is the energy required to remove an electron from the material and place it an infinite distance away, figure 2-3 is a schematic illustration.

When selecting metals for ohmic contacts to n-type semiconductors, the desired case is $\Phi_M < \Phi_S$ in order to avoid formation of an energy barrier, $\Phi_B$, to electron transport.

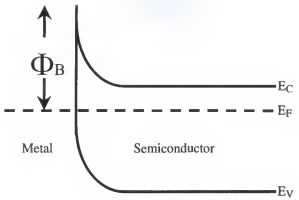


Figure 2-2. Band diagram of metal/semiconductor interface showing energy barrier to carrier transport, $\Phi_B$.

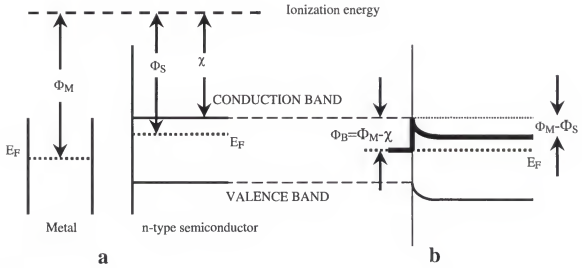


Figure 2-3. Energy bands for a metal with work function, $\Phi_M$, and n-type semiconductor with work function, $\Phi_S$, (a) before and (b) after intimate contact. $\chi$ is the electron affinity. The energy barrier to electron transport, $\Phi_B$, is outlined with bold lines.

Table II. Work functions for some typical contact metals. [after references 13 and 14]

| **Metal:** | Ag | Ti | Cr | Au | Pd | Ni | Pt | Al | W |
|---|---|---|---|---|---|---|---|---|---|
| **Work Function(eV):** | 4.3 | 4.33 | 4.5 | 4.9 | 5.13 | 5.15 | 5.65 | 4.08 | 4.55 |

For p-type semiconductors, $\Phi_M > \Phi_S$ is desired. Table II lists some typical contact metals and their work functions. The work function of n-GaN is around 4.1 eV. Unfortunately, in the case of GaN there does not exist a suitable contact metal that avoids barrier formation. Although Al has a smaller work function than n-GaN, contacts directly to Al have been shown to be rectifying after annealing.[13] This is likely due to the formation of AlN at the metal-semiconductor interface. Since no metal exists that would allow unimpeded carrier flow across the contact interface, carriers must be thermally excited over the barrier (thermionic emission), quantum mechanically tunnel through it (field emission) or move via a combination of the two (thermionic field emission).

## 2.3 Models for Contact Resistance

Murakami and Koide have explained the fundamental models describing specific contact resistance, $\rho_c$.[14] There are three cases, for light, medium, or heavy doping. Figure 2-4 illustrates the band-diagrams for these three cases. The dominant conduction mechanism will be a strong function of the doping concentration and temperature. Thermionic emission will occur for the case of light doping, $N_D < 10^{17} cm^{-3}$. Here the

depletion width in the semiconductor at the interface is large and carriers are unable to tunnel through the barrier. The current flow is a function of temperature and the contact

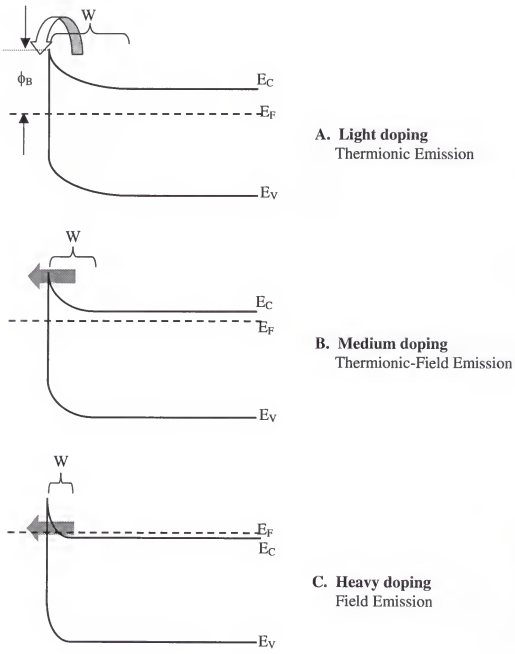


Figure 2-4. Band diagrams for an n-type semiconductor with different doping levels and depletions widths, W. The block arrows indicate the predominant conduction mechanism. See text for details

resistance, $\rho_c$, can be described, after the Wentzel-Kramers-Brillouin (WKB) approximation as

$$\rho_c = C_1 \exp\left(\frac{q\phi_B}{kT}\right)$$

where $C_1$ is a function of temperature, q is the electronic charge, k is Boltzmann's constant and T is temperature.

Thermionic field-emission occurs when doping is at an intermediate level, $10^{17}$ to $10^{18}$ $cm^{-3}$. The depletion region becomes narrower and charge carriers can breach the interfacial barrier with some thermal activation. The specific contact resistance here is modeled by

$$\rho_c = C_2 \exp\left[\frac{\phi_B}{\sqrt{N_D}\coth\left(\frac{E_{00}}{kT}\right)}\right]$$

where $E_{00} = \frac{qh}{4\pi}\sqrt{\frac{N_D}{m^*\varepsilon}}$ .

$C_2$ is a function of $\Phi_B$ and T, h is Planck's constant, $\varepsilon$ is the dielectric constant of the semiconductor, m* is the effective mass of the tunneling electron and $N_D$ is the doping concentration.

Finally, when the doping level is high, $>10^{18}$ $cm^{-3}$, the depletion width becomes narrow and the carriers are able to tunnel through the interfacial barrier. Here the contact resistance is governed by field emission and given by

$$\rho_c = C_3 \exp\frac{q\phi_B}{E_{00}}$$

where $C_3$ is a weak function of temperature.

## 2.4 History of Contacts to III-Nitrides

Now that a description of the physical principles governing contact performance has been made, a review of work on contacts to III-nitrides will be rendered. Since most of the important optical and electronic devices based on III-N materials rely on GaN, this section will examine the current state of the art for that material. The figure of merit for contacts is the specific contact resistance, $\rho_c$, with units of $\Omega$-cm$^2$.

### 2.4.1 N-Type

The first reported contacts to GaN were made by Foresi and Moustakas. employing a Au or Al contact directly deposited on GaN yielding $\rho_c \sim 10^{-3}$ $\Omega$-cm$^2$.[15] Subsequently, Lin *et al.* used an Al/Ti bilayer metallization scheme to achieve $\rho_c = 8 \times 10^{-6}$ $\Omega$-cm$^2$.[16] Their approach utilized a 20 nm layer of Ti e-beam deposited on GaN followed by a 100 nm capping layer of Al. A 900° C anneal for 30 s was needed to obtain the best result. Using Pd/Al metallization and a 650° C, 30 s anneal, Ping *et al.* measured $\rho_c = 1.2 \times 10^{-5}$ $\Omega$-cm$^2$.[17] Guo et al. deposited 15 nm of Ti followed by 150 nm of Ag on GaN to obtain an unannealed contact resistance of $6.5 \times 10^{-5}$ $\Omega$-cm$^2$.[18] A multilayer structure was studied by Fan *et al.* that yielded contact resistances as low as $8.9 \times 10^{-8}$ $\Omega$-cm$^2$.[19] Their approach starts with an RIE etch of the GaN surface followed by deposition of Ti (15 nm), Al (220 nm), Ni (40 nm), and Au (50 nm). This was followed by an RTA of 900° C for 30 s. Cole *et al.* studied the thermal stability of W ohmic contacts to GaN.[20] The 50 nm W contacts were sputtered onto etched GaN samples and annealed at 1000° C for one minute. An interfacial W-N phase was

observed that was considered responsible for the thermal integrity of the contacts, which had an $\rho_c$ = 8.0 X $10^{-5}$ $\Omega$-cm$^2$ . Miller and Holloway studied several metallization schemes including Ag, Au, TiN, Au/Ti, Au/Mo/Ti, and Au/Si/Ti.[21] Their results showed Ag and Au diffuse across the GaN interface for anneals >500° C but the other contact schemes were thermally robust even with 30 minute anneals at 500° C. Their results indicate the formation of an interfacial TiN is essential to obtaining a useful contact. Smith *et al.* examined Al contacts at room temperature and 500° C.[22] Values of 8.6 X $10^{-5}$ $\Omega$-cm$^2$ were obtained at room temperature with 6.2 X $10^{-5}$ $\Omega$-cm$^2$ at 500° C. These values rose after samples received 60 s annealing treatments at 550 or 650° C. It was discerned through high-resolution TEM and electron energy loss spectroscopy that an interfacial Al nitride or Al oxynitride had formed. Further investigation of the importance of an interfacial TiN layer was conducted by Wu *et al.*[23] Their study used a 2-step Ti deposition capped by a 200 nm layer of Au. First, 20 nm of Ti was deposited and annealed at 975° C for 30 s followed by another 20 nm of Ti. This scheme yielded contact resistances of 3 X $10^{-6}$ $\Omega$-cm$^2$ . SIMS data showed the presence of an interfacial TiN layer. These samples also proved resistant to HCl and HF.

Work has also been done with alloys of In, Ga, and Al nitride. Vartuli et al. has examined the conduction mechanism for W and $WSi_x$ contacts to InGaN and InN.[24] The dominant mechanism for annealed samples was concluded to be field emission as determined by temperature dependent contact resistance measurements. The exception was with as deposited metal on InN which exhibited thermionic emission.

2.4.2 P-Type

It should be noted that the contact resistances for p-GaN are several orders of magnitude higher than n-GaN because of the difficulty in achieving high carrier concentrations. This stems from the low activation fraction of acceptor impurities (~10%) and the presence of compensating defects like N vacancies. The approach to forming contacts to p-type GaN has thus far been largely identical to that used for n-type material. That is, a metal such as Ni, Au or Pt is deposited and then annealed, forming an interfacial metal-nitride layer.

Trexler *et al.* compared the efficacy of Ni/Au, Pd/Au and Cr/Au contacts to p-GaN having a carrier concentration of ~$10^{17}$/cm$^3$.[25] The structures consisted of 50 nm of Ni, Pd or Cr capped with 100 nm of Au. All contacts were rectifying as deposited with the Cr/Au contacts becoming ohmic after an RTA of 900° C for 15 s. The specific contact resistance for these contacts was ~ 4.3 X $10^{-1}\Omega$-cm$^2$. Koide *et al.* confirmed the relationship between contact resistance and metal work function for contacts to p-GaN.[26] However, they concluded that the non-alloyed contacts (Ni and Ta) used for their study did not provide low enough resistance for blue laser diodes. This work was corroborated by that done by Ishikawa *et al.*[27] and Mori *et al.*[28] The temperature dependence of Pt/Au contact resistance was elucidated by King and coworkers.[29] They found rectifying behavior at room temperature changed to Ohmic above 200° C. A minimum $\rho_c$ of 4.2 X $10^{-4}$ $\Omega$-cm$^2$ was obtained at 350° C. The dopant was not activated until after metal deposition when an anneal at 750 °C for 10 min in $N_2$ was performed. It is believed that dopant activation may damage the p-GaN surface, creating compensating defects like N vacancies. By using only one thermal treatment to both activate dopant species and

anneal the contact, compensation is minimized. Kim *et al.* used e-beam evaporated Pd/Au contacts to achieve $\rho_c = 9.1 \times 10^{-3}$ Ω-cm$^2$ after annealing.[30] Diffusion of Cr into p-GaN is believed by Yoo *et al.* to explain a $\rho_c = 1.2 \times 10^{-4}$ Ω-cm$^2$ for Cr/Au annealed at 500 °C for 1 min.[31] A tri-layer scheme consisting of Ni/Cr/Au was found by Kim *et al.* to have $\rho_c = 8.3 \times 10^{-2}$ Ω-cm$^2$ to p-GaN and $\rho_c = 2.6 \times 10^{-4}$ Ω-cm$^2$ to n-GaN, demonstrating the ability to make ohmic contacts to both n- and p-GaN simultaneously.[32]

The literature indicates that ohmic contact research has been largely limited to studying the effect of various metal deposition and annealing techniques. The use of refractory metallization schemes useful for high temperature applications has been ignored. Some consensus has developed that the formation of an interfacial nitride is required for thermally stable n-type contacts.

## 2.5 The Intermediate Semiconductor Layer

A re-examination of the equations describing specific contact resistance presented above reveals that the contact resistance can be lowered by reducing the interfacial energy barrier that exists at the metal/semiconductor (M/S) interface or by creating a highly doped layer in the semiconductor. The best approach to achieve either condition is by creating an intermediate semiconductor layer (ISL) between the underlying active layer and the contact metal, as illustrated in figure 2-5. The ISL must have a smaller band-gap than the active layer in order to reduce the interfacial energy barrier. Further, to promote tunneling of carriers, the ISL must have the capacity for being highly doped.

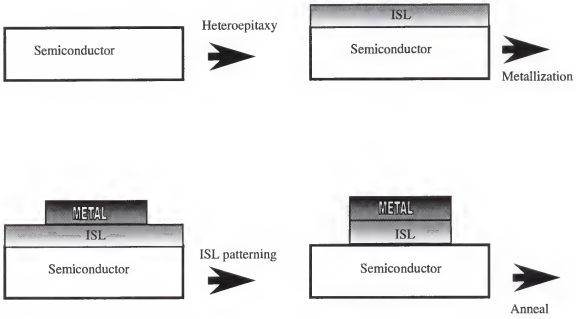


Figure 2-5. Schematic of ohmic contact formation to large bandgap semiconductor using an intermediate semiconductor layer (ISL).

This approach has been successfully employed with GaAs devices utilizing a GaInAs ISL.[33] Analogous to what has been done with GaAs, InN based contact layers will be explored for the nitrides. In addition to achieving low specific contact resistance, thermally stable contacts are required to fully exploit the high-power and high-temperature applications accessible by III-nitride based devices. This dissertation will discuss fabrication of an ISL that reduces the energy barrier at the M/S interface, as this method is required for large band gap semiconductors where dopant activation is low.

There are several techniques available to fabricate thin film semiconductor layers suitable for ISLs. Metalorganic molecular beam epitaxy (MOMBE), metalorganic chemical vapor deposition (MOCVD), and molecular beam epitaxy (MBE) are three common approaches. The principles of these crystal growth techniques and their relative merits will be examined in the following chapter.

# CHAPTER 3
# EPITAXIAL GROWTH PRINCIPLES AND APPARATUS

This chapter will present the basic principles of growing high quality semiconductor films, the basis for forming low resistance ohmic contacts using the ISL approach. The bulk of the work done for this dissertation centered on selecting and refining film growth conditions leading to epitaxial layers using molecular beam sources. The term "epitaxy" is used to denote deposited layers that are in crystallographic registry with the underlying single crystal substrate. That is, the deposited film adopts the long-range atomic order associated with the position of atoms in the substrate. It is essential to select film deposition parameters that result in epitaxial growth in order to realize optimal semiconductor carrier transport properties. Crystalline defects such as dislocations, antiphase domains, and grain boundaries degrade carrier mobility and contact performance and should therefore be minimized. The degree to which epitaxial growth is achieved is a function of the film growth conditions used and substrate choice.

The latter sections of this chapter will cover the three primary types of equipment used to develop epitaxial films. Epitaxial growth equipment is generally very complex, expensive, and difficult to maintain. Finally, a description of the hybrid apparatus employed for this work is made.

## 3.1 Principles of Epitaxy

This section will present a qualitative development of the fundamental processes leading to epitaxial film growth. A rigorous quantitative discussion is omitted because the focus of this work is with experimental results, and the complexities of nitride semiconductor growth are not amenable to precise modeling. Consequently, predictions of film attributes derived from mathematical formulae are of little practical value. This being the case, a qualitative, rather than quantitative treatment of growth theory is more consistent with the realities of nitride epitaxy.

Epitaxial growth requires the confluence of several kinematic processes involving the arrival, interaction and departure of atomic or molecular species at a heated surface. Epitaxial films are grown under non-equilibrium conditions where an overpressure of precursor species exists above the growing film. This gives rise to the formation and growth of nuclei on the substrate and subsequent film growth. The growth rate is determined primarily by the substrate temperature and the flux of film constituents reaching the surface. An important point to emphasize is that final film characteristics are the result of overall system energy minimization during growth. Hence, epitaxial quality will be constrained by kinematic processes. The five salient features are as follows:

1. The arrival and adsorption of molecular or atomic species to the substrate or growth surface.
2. Decomposition of molecular species.
3. Surface diffusion of adatoms.
4. Desorption of adatoms away from the surface.
5. Incorporation of adatoms into the growing film.

These five processes are illustrated in figure 3-1.

The arrival rate of precursors is determined by the temperature of effusion ovens when solid sources are used, and the gas flow rate when gaseous sources are used. Section 3.5 will provide a description of precursors used for film growth. When growth takes place under conditions where the total pressure is greater than a few torr it is possible to encounter prereactions in the gas phase that can reduce the arrival rate of film constituents.[34] This discussion will be limited to the case of high-vacuum deposition conditions, as found with molecular beam growth techniques, therefore precursor interactions can be neglected. However, parasitic prereactions must be considered when higher pressure techniques such as metalorganic chemical vapor deposition (MOCVD) are used.

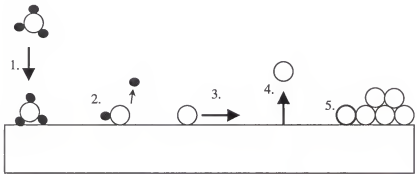


Figure 3-1. Kinetic processes associated with film growth. 1. Arrival and adsorption, 2. Decomposition, 3. Diffusion, 4. Desorption, 5. Incorporation.

Adsorption of chemical species on a surface will occur to reduce the free energy of the adsorbate. As a molecule moves toward a surface, attractive forces arising from coulombic, covalent, and van der Waals interactions are balanced by repulsive forces arising from the overlap of filled electron orbitals. Figure 3-2 shows the resultant energy curve. The force balance results in energy minimization when the adsorbate is a few angstroms from the surface.

Decomposition of adsorbed molecular species will occur if the thermal energy imparted by the heated substrate is sufficient to break chemical bonds comprising the adsorbate. When metalorganic precursors are developed, care is taken to synthesize molecules that will readily decompose at normal substrate temperatures (400-900° C). It is possible for multi-component species to only partially decompose. This increases the possibility of incorporating unwanted elements into the growing film, especially carbon and oxygen. Usually, substrate temperatures are selected to maximize decomposition of the precursor while maintaining a sufficient growth rate.

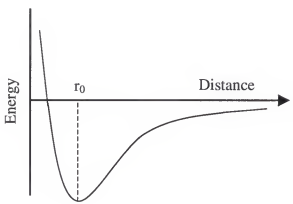


Figure 3-2. Energy curve resulting from summation of attractive and repulsive forces on an adatom at a surface. The minimum energy position indicates the equilibrium adatom distance, $r_0$.

Surface diffusion of adatoms occurs when adatoms acquire sufficient thermal energy to breach energy barriers imposed by the periodic array of atoms in the substrate. Figure 3-3 illustrates schematically the activation energy required for an adatom to translate to neighboring lattice sites. Usually this energy is much less than that needed for desorption of the adatom, which requires bond breaking. Diffusivity is a function of substrate temperature and the distance an adatom migrates will increase with temperature (up to the point when desorption becomes dominant). For epitaxy to occur the adatom must have sufficient surface diffusivity to incorporate at low energy surface sites. In

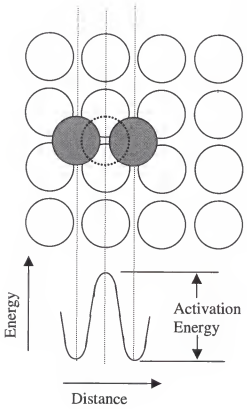


Figure 3-3. Schematic representation of adatom diffusion illustrating energy barrier to site hopping.

some cases, surfactants may be utilized to lower the activation energy associated with surface diffusion. This results in an increased diffusion length, thereby increasing the probability of adatom incorporation at low energy lattice positions. Otherwise the adatom may incorporate at sites resulting in amorphous or polycrystalline material.

Low energy sites correspond to crystallographic lattice positions that occur at ledges or kinks on the surface, as illustrated in figure 3-4. The lower energy is a consequence of the adatom retaining fewer dangling bonds at ledges or kinks as compared to terrace positions. Once the adatom encounters a ledge or kink position, it is no longer energetically favorable to continue migrating and it will incorporate into the growing film.

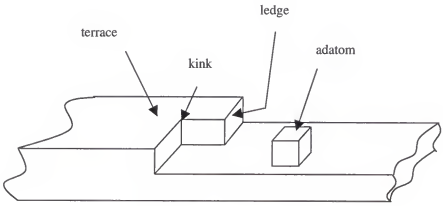


Figure 3-4. Schematic of growth surface showing possible incorporation sites for the adatom.

Desorption of adatoms can be described by a desorption frequency, $\nu_{des}$ that is a function of the atomic vibrational frequency, $\nu_0$ ($\sim 10^{13}$/s) and an activation energy which is characteristic of the escape process, $\Delta G_{des}$. The relationship is of the form:

$$\nu_{des} = \nu_0 \exp\left(\frac{-\Delta G_{des}}{kT_s}\right)$$

where k is Boltzmann's constant. The growth rate of the epilayer will begin to decrease when $T_S$ becomes high enough to promote desorption of adatoms over surface diffusion.

## 3.2 Models of Nucleation

The most important stage of film growth is nucleation. Nucleation determines the resulting structural characteristics of a film and whether epitaxy will result. There are three widely accepted modes of film nucleation leading to epitaxial growth, shown schematically in figure 3-5. Three-dimensional island formation on a bare substrate (Volmer-Weber or 3D), layer-by-layer deposition (Frank-van der Merwe or 2D), and island formation on a thin uniform layer (Stranski-Krastanov). The mode of nucleation is determined by surface energy minimization criteria, as discussed qualitatively below.

The variables $\sigma_s$ and $\sigma_e$ represent the surface energy of the substrate and the epilayer, respectively. Generally, Volmer-Weber (VW) growth will dominate when $\sigma_s<\sigma_e$. System energy is minimized when the epilayer forms islands. This leaves as much of the low energy substrate exposed as possible while minimizing the surface area of the high energy epilayer. Crystal surface energy is typically anisotropic, meaning

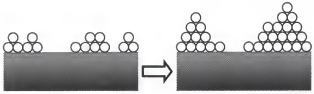

**Volmer-Weber (VW), islanding**

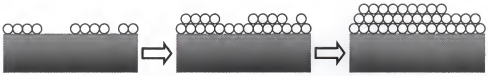

**Frank- van der Merwe (FM), layer by layer**

**Stranski-Krastanov (SK), layer-island**

Figure 3-5. The three nucleation mechanisms leading to epitaxial growth.

some crystal planes have higher surface energy than others. The shape of an island will be one that maximizes the area of low energy facets while minimizing high energy ones.

Frank-van der Merwe (FM) growth is favored if $\sigma_s > \sigma_e$. Energy minimization is accomplished by complete coverage of the substrate by the epilayer. In some cases, interfacial energy differences between substrate and epilayer and between monolayers in the film will favor Stranski-Krastanov (SK) growth. This situation implies there is relatively high interfacial energy between the first and second monolayers of the film. Energy is minimized by island formation on top of a thin uniform layer.

Ideally, 2-D (FM) growth is desired for thin film semiconductor layers. This results in smooth, uniform layers with fewer antiphase domains, dislocations, or grain boundaries. Epilayer smoothness is especially important when multi-layer structures are utilized as film roughness can be translated to, and exacerbated by, subsequent deposition. High surface roughness can contribute to irregular metallization behavior. Microscopic thickness variations in metal contacts cause current density variations leading to spiking of metal into the active region of a device.

## 3.3 Heteroepitaxy

Additional issues must be considered when film growth is attempted on a substrate that is unlike the film, i. e. GaN/sapphire. It is not always possible to find a substrate that has a lattice dimension matching that of the epilayer, $a_f$. The atoms in the epilayer will attempt to match the atom spacing of the substrate, $a_s$, via bond distortion, creating strain energy. The strain energy is a function of film thickness and can be described by

$$\sigma_s = \frac{Y}{2} d f^2 .$$

Young's modulus is Y, d is film thickness and $f = (|a_f - a_s|)/a_{avg}$ is the degree of lattice mismatch. The critical thickness, $d_c$, occurs when the strain energy matches the energy required to form a misfit dislocation in the film. When $d_c$ is exceeded, a misfit dislocation will form that lowers the total energy of the system and the film is considered relaxed. Strained films that are less than $d_c$ will adopt the in-plane lattice parameter of the substrate with a corresponding deformation of the film perpendicular to the interface. Such films are qualified as pseudomorphic, as figure 3-6 illustrates.

The critical thickness, $d_c$, is given by Mathews and Blakeslee as

$$d_c = \frac{b(1 - \mu \cos^2 \theta)}{2\pi f (1 + \mu) \cos \phi} \ln\left(\frac{d_c}{b} + 1\right)$$

where b is a Burger's vector on the order of $a_s$ and $a_f$, $\mu$ is Poisson's ratio, $\theta$ is the angle between the dislocation line and b, $\phi$ is the angle between the slip direction and the direction in the film plane which is perpendicular to the line of intersection of the slip plane and the interface.[35]

By way of example, a film with f=1.0% will start generating misfit dislocations at $d_c \approx 30$nm. This corresponds to a misfit dislocation every 30 to 50 nm along the interface between film and substrate. Dislocations are known to be deleterious to device performance, as they act as non-radiative recombination centers for photons and scattering sites for current carriers. Therefore, it is desired to minimize the opportunity for these defects to form, usually by finding substrates that offer f< 1.0%. Given $f_{GaN/sapp}$

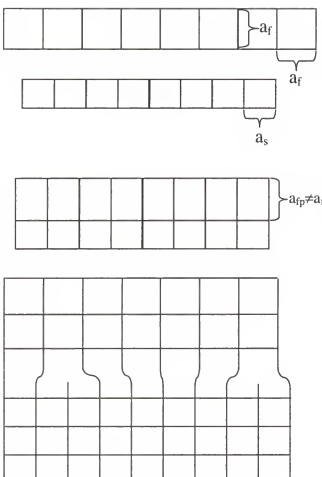


Figure 3-6. Illustration of substrate and free standing (unstrained) film (top). Heteroepitaxial growth leading to a pseudomorphic film (middle). Film thickness exceeding critical thickness, $d_c$, causing misfit dislocations (bottom).

≈ 14% would seem to eliminate sapphire as a useful substrate for GaN growth. However, nitride devices have shown a unique ability to withstand defect densities orders of magnitude greater than devices fabricated from traditional semiconductors.

Heteroepitaxial films may face the problem of thermal mismatch as well. Differences in thermal expansion coefficients between the film and substrate can generate strain when the film is cooled from the growth temperature. In some cases the strain developed during cool-down can result in cracking of the epilayer.

## 3.4 Graded Layers

Heteroepitaxy can also refer to film growth on a dissimilar epilayer that has been previously deposited. Compound semiconductor devices rely on the ability to construct unique band structures through multiple epilayer deposition. The conduction band and valence band positions at a heterointerface in part determine the operating characteristics of a device. Figure 3-7 illustrates the three types of band offsets that can occur at a heterointerface. Note that this schematic represents offsets that occur before thermal equilibrium has been established between the two films. The quantities $\Delta Ec$ and $\Delta Ev$ represent the conduction band and valence band energy differences, respectively. After thermal equilibrium is established, band bending will occur at the interface. The final shape of the band diagram will depend on the initial position of the Fermi energy in each layer. For certain systems, the heterointerface will contain an energy barrier to charge transport across the interface. It is possible to ameliorate the effects of this barrier through the use of a graded layer.

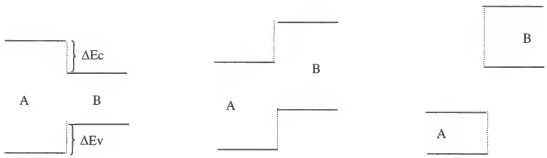


Figure 3-7. Types of band offsets at a heterointerface. Straddling (left), staggered (middle), and broken-gap (right). [after reference 36]

A graded layer involves continuously varying the composition of an intermediate layer to form a smooth transition between two films having different components. For example, to grade between films consisting of AQ and BQ, one would grow a layer of $A_{1-x}B_xQ$ with $0 \leq x \leq 1$ (see figure 3-8). The graded layer thickness is on the order of 10nm. The graded layer removes or reduces spikes in the band structure at the interface, augmenting carrier transport across the junction. This technique will be employed for improved ohmic contact performance to nitrides, as discussed in Chapter 6.

## 3.5 Comparison of Growth Techniques

Thus far, the basic concepts of epitaxial film growth have been presented. This section will introduce and discuss the apparatus utilized for epitaxial film growth. A comparison of the three most common growth systems: MBE, MOCVD, and MOMBE is outlined.

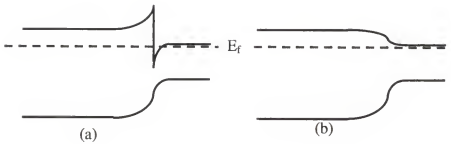


Figure 3-8. Diagram of band structure at a heterointerface without (a) and with (b) a graded layer.

3.5.1 MBE

Molecular beam growth implies that the ambient pressure above the growth surface is low enough that gas phase interactions are essentially nonexistent. Source atoms or molecules entering the growth chamber can be directed toward the substrate in a near collimated beam and arrive at the substrate unimpeded. This condition is considered the molecular flow regime. Background chamber pressure (not during growth) can approach $10^{-11}$ torr. During growth, pressures of $10^{-6}$ torr are typical. Because of the extremely low pressures involved, MBE growth is highly sensitive to contamination and great lengths are extended to avoid introducing unwanted substances into the growth chamber.

Molecular beam epitaxial growth systems typically consist of an ultra-high vacuum (UHV) deposition chamber, a buffer chamber and load-lock. Vacuum levels are achieved with several types of pumps including mechanical, turbo, cryo, ion, effusion and turbomolecular. The use of a load-lock and buffer chamber allows substrates to be introduced to the growth chamber without contaminating it. The growth chamber is continually maintained at UHV conditions unless sources need replenishing or repairs must be made.

Solid sources are contained in an effusion cell that is directed toward the heated substrate, see figure 3-9. The effusion cell assembly is bolted to a stainless steel source flange on the growth chamber. An inert ceramic insert holds the source and is heated with a resistive coil. Temperature is monitored with a thermocouple that is part of a feedback loop attached to a temperature control unit. This way, a temperature setpoint can be entered and the control unit will automatically adjust the voltage and current to the heater coil to reach and maintain the prescribed setpoint. When not in use, a setpoint of ~100° C is maintained to prevent adsorption of unwanted contaminants onto the cell. The effusion cell is outfitted with a shutter that can be opened or closed rapidly, starting or stopping the flux of atoms as needed. This permits the fabrication of abrupt interfaces when growing multilayer structures. The flux, $F_s$ of atoms of molecular weight M, impinging on a substrate a distance $l$ from the aperture with area A, at temperature T and cell pressure P is given by

$$F_s = 1.12 \times 10^{22} \frac{PA}{l^2 \sqrt{MT}} \text{ molecules/cm}^2\text{s}.$$

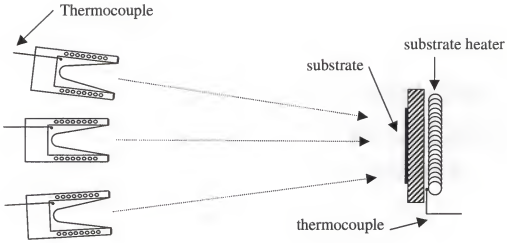


Figure 3-9. Schematic of MBE effusion cell and substrate arrangement.

If solid Ga (M = 70) is used as a source, for example, the vapor pressure will be $2.2 \times 10^{-3}$ torr at a cell temperature of 970° C. Given a source to substrate distance of 15 cm and an opening of 4 $cm^2$ on the effusion cell, $F_s$ will be $\approx 1.5 \times 10^{15}/cm^2s$. This corresponds to a growth rate of ~1.5 monolayers, (8Å) per second. Commonly, an overpressure of the group V (i. e. nitrogen) element is maintained because it will adhere only to an existing layer of group III atoms and is therefore self limiting. The arrival rate of the group III species is usually rate limiting.

It is common to find gaseous sources used in conjunction with solid sources for some semiconductor growth systems. For example, hydrides such as arsine, $AsH_3$ and phosphine, $PH_3$ are used as sources for arsenic and phosphorous. Ultrapure $N_2$ is generally used for growth of nitride semiconductors. The gas is passed through a plasma

generator prior to injection into the growth chamber to provide active monatomic nitrogen species. More on this will be presented in section 3.6. Gas flows are controlled using a mass flow controller (MFC), with typical flow rates ranging from 1.0 to 20 standard cubic centimeters/s (sccm).

Even though great pains are taken to ensure a pristine growth environment, invariably impurities will persist. Unwanted contaminants such as carbon and oxygen may be incorporated into the growing film. The likelihood of contaminant incorporation will be a function not only of their relative abundance but also of the gettering ability of the arriving growth constituents. As the bond strength of the source atoms increases, the probability of their bonding with and incorporating impurities increases. Table III compares bond strengths of some common constituents. Included for comparison are methyl bonded precursors that are typical of MOCVD and MOMBE. The relatively high bond strength of nitrogen can lead to high impurity incorporation levels making nitride growth especially difficult.

Because of the possibility of contamination, the growth rate should be as high as possible without sacrificing material quality. Typical MBE growth rates range from several hundred to several thousand angstroms per hour, depending on the layer to be deposited.

The UHV environment associated with MBE growth is amenable to a variety of in-situ characterization techniques. A residual gas analyzer (RGA) or quadrapole mass spectrometer (QMS) can be attached to the growth chamber allowing for analysis of constituents present during growth. This is possible because there are unincorporated species that will remain in the growth chamber long enough to be detected by the analysis

equipment. Another powerful analytical tool is reflective high-energy electron diffraction (RHEED). Here, an electron gun is positioned on one side of the growth chamber to send a beam of electrons to the substrate or film surface at a glancing angle. The diffracted beam is collected on a phosphor screen on the opposite side of the growth chamber. Information about surface condition can be discerned such as degree of crystallinity. Further, spot intensity variations over time can be used to determine growth rate during the early stages of film growth.

Table III. Relative bond strengths of constituents commonly found in MBE, MOCVD and MBE. The stronger the bond, the easier the impurity incorporation. [after reference 37]

| Bond | Bond Strength (kcal/mole) |
|---|---|
| In-O | <77 |
| Ga-O | 85 |
| Al-O | 122 |
| As-O | 115 |
| N-O | 151 |
| Me-In$(Me)_2$ | 49 |
| Me-N$(Me)_2$ | 75 |
| Me-Al$(Me)_2$ | 75 |

MBE is an excellent method of producing complex multilayer structures where precise control of dopant concentration, layer thickness and interface abruptness is required. Unfortunately, source replenishment can be a long and difficult process usually

involving venting the entire growth chamber. Once the growth chamber has been exposed to air, the inside walls and components will be coated with moisture and everything else found in the ambient. The removal of such unwanted adsorbates requires heating the evacuated growth chamber over a period of days. Usually, a bake-out will be done prior to venting as well in order to reduce the chances of introducing hazardous adsorbed material into the atmosphere. The whole process can take up to a week, making source replenishment a significant drawback to MBE growth.

### 3.5.2 MOCVD

Metalorganic chemical vapor deposition, sometimes referred to as organometallic vapor phase epitaxy (OMVPE), has emerged as the most common apparatus for nitride growth. The technique relies on the decomposition and reaction of a metalorganic group III species (i. e. trimethylgallium, TMG) with a hydride group V species (i. e. ammonia, $NH_3$). Chemical decomposition and reaction take place on a heated substrate. For GaN growth, a typical reaction might be

$$Ga(CH_3)_3 + NH_3 \Rightarrow GaN + 3CH_4.$$

As in MBE growth, the group V species will be in excess over the group III species. The substrate temperature will be well above that required for pyrolisis of the precursors, making the arrival rate of group III constituents rate limiting. The operating pressures are orders of magnitude greater than that found with MBE systems, typically 10 to several hundred torr.

Metalorganic sources are available as solids or liquids. The chemical is contained in a stainless steel bubbler having an inlet and outlet manual valve. The bubbler is immersed in a chilled water bath that maintains a constant temperature. A temperature is

selected that will give a partial pressure from a few tenths to several torr. Material is transported to the growth chamber via a carrier gas, usually $H_2$, that flows through the inlet and outlet of the bubbler. The carrier gas flow is controlled using an MFC and line pressure is commonly controlled with a capacitance manometer. Carrier gas flows on the order of 100 sccm are common. Hydride flows of up to a few thousand sccm are possible. The relatively high flow of gases into the reactor tends to reduce the incorporation of unwanted impurities by having a gettering effect. The flux of metalorganic, $F_{MO}$, injected into the reactor is given by

$$F_{MO} = \frac{F_{CG} P_{MO}}{P_T - P_{MO}}$$

where $F_{CG}$ is the carrier gas flux, $P_{MO}$ is the partial pressure of the metalorganic, and $P_T$ is the total pressure. The flow of gas above the substrate creates a stagnant boundary layer through which constituents must diffuse.

The key to MOCVD growth is the complex gas handling equipment that allows for switching of sources into the reaction chamber in a precise manner. In addition to the manual valves located on the bubbler, it is common to have electronically controlled inlet, outlet and bypass valves on a bubbler manifold. These are supplemented with carrier gas on/off valves, vent and run valves. Figure 3-10 illustrates the arrangement used in a typical metalorganic delivery system. This arrangement is also found on MOMBE systems including the Varian Gen II used for this study.

MOCVD growth offers the advantage of easy source replenishment. Since the bubblers can be valved off from the rest of the system, it is possible to replace them

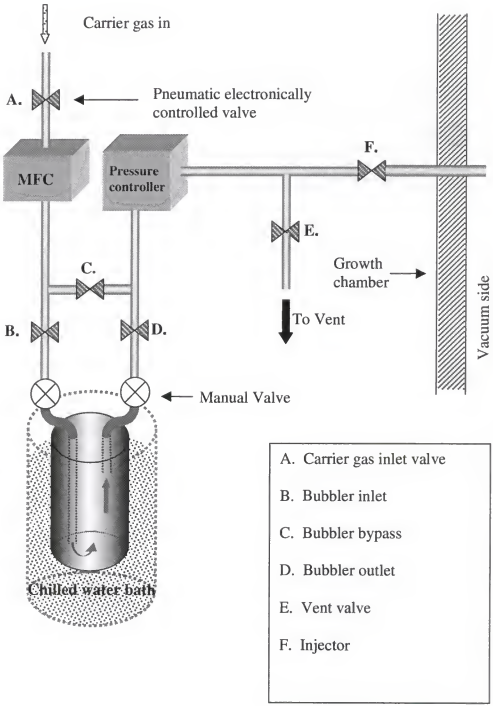


Figure 3-10. Schematic of metalorganic delivery system showing bubbler, carrier gas transport and control elements.

quickly without risk of contaminating the reactor. Moreover, since UHV conditions are not required, massive pumping capacity is unnecessary.

The high pressures employed during growth preclude the use of most in-situ analytical devices such as RHEED and mass spectrometry. The high flow rates can lead to parasitic gas phase prereactions that have a deleterious effect on growth rate. Care must be taken to separate overly reactive precursors until just before reaching the substrate, making hardware design of critical importance. Sometimes it may be necessary to choose alternative precursors to lessen the chance of gas phase reactions. Another major disadvantage is that high substrate temperatures are generally required. For nitride growth, the substrate must be hot enough to decompose a sufficient quantity of $NH_3$ to provide reactive nitrogen. Substrate temperatures of >700° C are usually required. This makes growing films consisting of high vapor pressure elements such as indium very difficult.

### 3.5.3 MOMBE

Metalorganic molecular beam epitaxy is a blending of the two techniques previously discussed. It employs the UHV environment of MBE, making in-situ analysis possible, along with the ease of source replenishment associated with the use of bubblers. This flexibility comes at a price, however, in that the challenges of maintaining a UHV environment are combined with the complexities of gas handling equipment. The pressure regime during growth is higher than standard MBE but is still orders of magnitude less than MOCVD. Metalorganic sources used for MOCVD also work well for MOMBE, although the gas flow rates are much less with the latter system. Figure 3-

11 summarizes the differences in constituent arrival and surface interactions for the three techniques.

## 3.6 The Varian Gas-Source Gen II

This section will describe the specific MOMBE system used for fabricating samples for this work. The equipment is housed at the Microfabritech facility on the UF campus. Figure 3-12 shows the layout of the growth chamber, buffer chamber, load lock, metalorganic bubbler manifold cabinet and pumping systems. The system can accomodate up to six metalorganic sources, four solid sources, and three hydrides. In addition, reactive nitrogen is supplied by either an electron cyclotron resonance (ECR) or radio frequency (RF) plasma generator. A quadropole mass analyzer allows identification and monitoring of growth species artifacts. A schematic of the growth chamber showing the source flange and substrate heater is provided in figure 3-13.

### 3.6.1 Vacuum Pumping Systems

As with MBE systems, the Varian has a host of pumps to handle the high-vacuum needs of the system. Pressure is monitored in the load-lock, buffer and growth chambers with ion gauges. Additional pressure gauges are present on the vent line, fore line and upstream of the molecular drag pump located by the load lock. The load-lock is roughed using a high-vacuum compatible mechanical pump. When the pressure has reached a few torr, a molecular drag pump (MDP) is initiated that will bring the pressure to the $10^{-4}$ torr regime. At this point, a gate valve isolating a CTI 100 cryopump is opened allowing the pressure to reach $<10^{-6}$ torr. The buffer chamber is pumped with an ion pump and reaches a base pressure of $\sim 10^{-8}$ torr. The growth chamber is pumped with a dual rotor, 2200

liter/s Balzers turbopump. This pump is excellent at removing most species including He, and maintains a background pressure of ~$10^{-7}$ torr. The turbopump is backed by a second mechanical pump that is lubricated with special perfluorinated oils that are hydride compatible. During growth, a CTI-8 cryopump is brought into service to assist the turbo with the high pumping capacity required when decomposition products are present in the growth chamber. When not in service, the CTI-8 is isolated with a gate valve. Growth chamber pumping is further assisted by the use of a cryo-shroud. The stainless steel growth chamber is actually a double walled vessel that can be filled with liquid nitrogen prior to growth. The cold inner walls can remove additional decomposition products and other species by condensation. Condensed gasses are then pumped out with the turbo pump after growth is completed and the chamber walls are allowed to return to room temperature.

Aside from the pumps required for achieving and maintaining high vacuum on the load-lock, buffer and growth chambers, there is a second TMP used to evacuate the vent line. This is backed by a third mechanical pump.

### 3.6.2 Sources

As mentioned above, the Varian possesses a variety of sources for epitaxial semiconductor growth and doping. The four solid metal sources are housed in effusion cells exactly as described for use by MBE growth. Gallium and indium are routinely kept charged while the other two sources may be changed periodically, depending on the needs of the users.

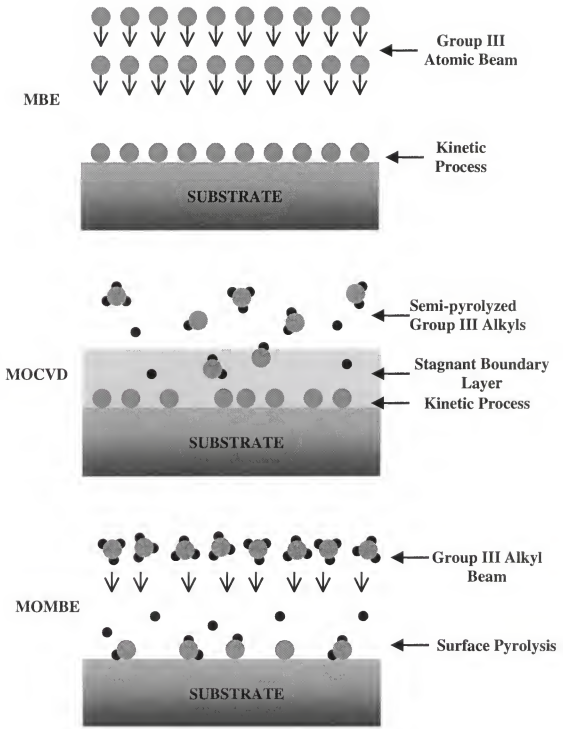


Figure 3-11. Schematic depicting the differences in constituent arrival and surface interaction for three common epitaxial techniques.

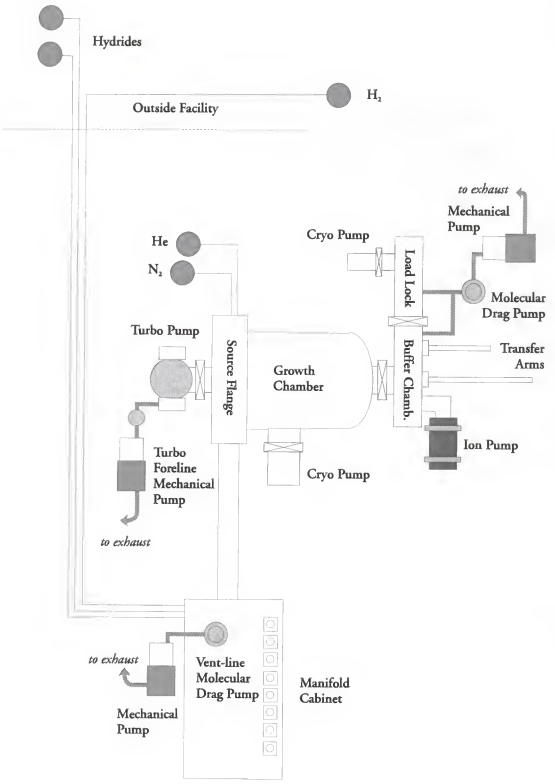


Figure 3-12. Schematic of Abernathy MOMBE lab. [after reference 38]

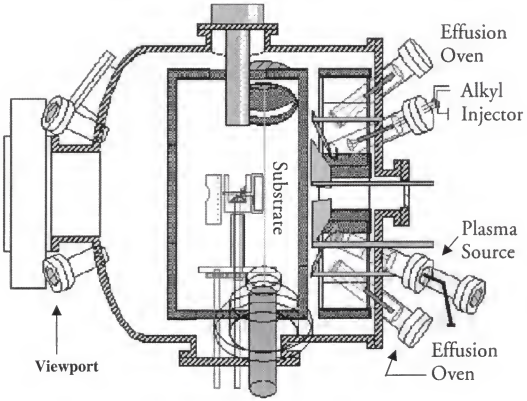


Figure 3-13. Schematic of MOMBE growth chamber. [after reference 39]

Metalorganic sources include trimethylindium (TMI), trimethylgallium (TMG), dimethylethylaminealane (DMEAA), and carbontetrabromide ($CBr_4$) among others. A discussion of the pertinent features of specific metalorganic precursors will be made in chapter five. The chemicals are contained in bubblers, just as described for use in MOCVD (section 3.5.2). Each source is equipped with a full complement of valving as shown in figure 3-10 that is housed inside an evacuated manifold cabinet. Care must be taken when handling these sources as they can be pyrophoric and in some cases toxic. These sources can be changed as needed with relatively little effort.

The Varian has three hydrides, arsine ($AsH_3$), phosphine ($PH_3$) and silane ($SiH_4$). Owing to their extreme toxicity, these gaseous sources are contained in pressurized cylinders housed in a special toxic gas cabinet outside the lab. The gasses are conducted to the growth chamber via double-walled stainless steel tubing especially designed for the task. This tubing is itself enclosed in conduit that is connected to a scrubbed exhaust system. The hydrides pass through a cracker which decomposes them before entering the growth chamber. The cracker consists of a tantalum catalyst with resistively heated coils and a thermal control system similar to that used for solid sources. During growth, a set-point of ~ 1000° C is maintained in order to adequately decompose the hydrides and provide a reasonable flux of As, P or Si. When not in use, the cracker is sustained at ~ 65° C to avoid buildup of adsorbates.

Since $N_2$ is extremely difficult to thermally decompose, and rather unreactive, temperature independent techniques must be adopted to provide a usable nitrogen flux. One way is by forming a plasma from a flow of nitrogen gas. Among other things, a

nitrogen plasma will contain levels of neutral atomic N. It is this highly reactive species that is believed to be important for nitride growth. The Varian has been fitted with either of two types of plasma sources, ECR or RF. These compact plasma generators can be bolted to the source flange in a way similar to a solid source effusion cell and are sometimes referred to as "remote" plasma sources. Initially a Wavemat MPDR 610 ECR plasma source was used for sample development, this was later switched to an SVT Assoc. RF source.

The ECR source consists of a cell that is connected to an ultra-pure, mass flow controlled $N_2$ supply. The cell is surrounded by a series of permanent magnets that generate a field along its axis. Microwave energy at 2.45 GHz is coupled into the source gas ($N_2$) creating a complex mixture of electrons, charged and neutral species. The magnetic field will cause electrons to accelerate in a helical path, promoting further ionization and neutral species generation. Power can be independently controlled with a typical range of 150 to 300 W. Varying the power allows reactive species to escape the cell aperture with various energies. The aperture is covered by a biasable grid that is attached to an independent power supply. This allows charged species to be preferentially selected or excluded from the cell.

The RF plasma source was produced by SVT associates and uses energy at 13.56 MHz. An MFC is used to carefully regulate gas flow into the cell, where energy is coupled to create a plasma. The RF power supply can be varied to control the energy of species effusing out, usually 200 to 400 W.

Using plasma generated reactive nitrogen obviates the need for high substrate temperatures, as would be found with MOCVD growth. This affords the Varian a

distinct advantage over other growth systems by allowing access to much lower substrate temperatures. It would be virtually impossible to grow nitride samples containing significant quantities of high vapor pressure elements (i. e. indium) without a plasma source.

The ability to utilize solid, metalorganic and hydride sources under UHV conditions make the Varian an exceptional semiconductor research tool. The instrument permits the investigation of a variety of unique compounds and complex structures inaccessible by other techniques. It is not unusual to select a path of experimental endeavor based on the research equipment available to the investigator. The development of improved ohmic contacts for nitride based devices using an intermediate semiconductor layer is well suited to the capabilities of the Abernathy MOMBE lab.

### 3.6.3 MOMBE Safety

Considerable effort has been taken to ensure that the toxic and pyrophoric substances associated with MOMBE growth will not pose a threat to the lab and other building personnel. Any areas that could possibly be exposed to hazardous gasses are housed in special enclosures that are evacuated through a facility scrubber designed to decontaminate the gas before being introduced to the environment. This includes the source flange, metalorganic manifold cabinet, and the turbo backing mechanical pump. After passing through the turbopump, residual growth chamber gasses are pumped through Carusorb scrubber material before reaching the mechanical pump. The mechanical pump exhaust is in turn scrubbed by the facility scrubber. Additional scrubber material is used on the vent line.

Toxic gas monitoring points are located in the manifold cabinet, turbo backing mechanical pump covering, injection flange shroud, and other critical areas. Any leaks detected will sound a special toxic gas alarm and emergency personnel are automatically contacted. The toxic gas monitor is interlocked with the Varian gas handling valves which are closed automatically in the event of an alarm. In case of a power failure, a diesel generator is automatically brought on line to maintain monitoring service.

In addition to being interlocked to the toxic gas alarm, all process valves will be automatically closed in the event of a power outage. Because the Microfabritech facility is subject to occasional power dips and transients that may last less than a second, it was necessary to install an uninteruptable power supply (UPS). This battery array conditions all the power going into the various MOMBE components and accommodates any transients in service. When all systems (pumps, power supplies, etc...) are in operation, the UPS can sustain them for up to 20 minutes before the batteries become drained.

When the growth chamber or any other toxic gas exposed equipment is vented, self-contained breathing apparatus (SCBA) is worn to protect the worker from any residual toxic substances that might be inhaled. Also, all others working at the Microfabritech facility are notified of the event and are kept clear of the MOMBE area.

Aside from hazards to the environment and humanity, care must be taken to ensure the service life of MOMBE components. Because high-vacuum components and pumps are extremely costly, it is important to follow proper procedures when working with the MOMBE. Opening valves in the incorrect order, for example, can be detrimental to the functioning of pumps or ion gauges.

3.6.4 MOMBE Maintenance

Owing to the many systems (pumping, power supply, chilled water baths) the MOMBE requires frequent checks and servicing. Some maintenance duties simply involve visual inspection to ensure proper functioning. The recirculating chilled water baths used to maintain bubblers at constant temperature must be kept filled and any ice buildup removed. Occasional addition of ethylene glycol may be necessary. The water levels the bubblers are submerged in must be kept filled.

The two cryopumps must be regenerated on a regular basis. Regeneration entails allowing the pump to warm to room temperature and pumping out all adsorbed species. The frequency depends on how much gas load the pumps have seen, usually once or twice a week. The compressors must be checked to ensure proper He pressure.

Mechanical and turbo pump oil levels and quality must be maintained. If pump oil starts to become cloudy, it must be replaced. This requires the use of SCBA. Used pump oil must be properly labeled and disposed of. All pump oil is considered contaminated and must be handled accordingly.

Once every six months or so, the Carusorb scrubber material both downstream from the turbopump and on the vent line must be replaced. Used Carusorb is considered contaminated and SCBA must be used.

Less frequently, solid sources must be recharged. This requires venting the growth chamber. Prior to venting, the growth chamber bake panels are installed and the system is baked for ~72 hours. This helps remove any volatile species that may have adsorbed onto inner surfaces. Viewports can become coated with residue from metalorganics or solid sources and must be removed and cleaned. Ion-guage filaments

may need replacing. After all work has been completed, the system is pumped down and baked for another 72 hours prior to use.

# CHAPTER 4
# SAMPLE CHARACTERIZATION

This chapter discusses the methods, principles and rationale for the various characterization techniques used to discern the properties of epitaxial thin films grown by MOMBE. It may be the investigators first impulse to perform a full battery of analysis techniques for every sample. However, time and money can be conserved if some thought is given prior to examining a sample.

There are four areas of sample analysis that may be examined: electrical, structural, morphological, and compositional. Within these four areas are techniques that are destructive and non-destructive. Ideally, nondestructive analysis is done first and as little material as possible is consumed by destructive techniques.

It is important to confirm results by making sure the total data set for a given sample is self-consistent. Electrical and compositional information should be complementary, for example. Also, if there is some doubt as to the validity of a measurement, it should be verified by another technique.

## 4.1 Electrical Characterization

In some ways, the electrical properties of a sample (carrier concentration, resistivity, and mobility) are the most relevant for semiconductor research. Ultimately, it is these attributes that determine the utility of a material for use in an electronic device structure. The development of ISLs for improved ohmic contact performance intimately

relies on knowledge of the electrical properties of thin epitaxial films. Therefore it is imperative to have a reliable way of determining these properties.

4.1.1 The Hall Measurement

The resistivity, carrier mobility, and carrier concentration can be determined using a technique based on the Hall effect. Figure 4-1 shows a schematic of a sample illustrating the Hall effect. Here, an n-type semiconductor has current flowing in the + x-direction with a magnetic field in the + z-direction. Electrons will be subjected to a force, known as the Lorentz force, that causes charge accumulation on one side of the sample. This charge separation induces an electric field known as the Hall field or Hall voltage, $\Delta V$.

The sample geometry shown in figure 4-2 is known as the van der Pauw geometry, and gives a resistivity, $\rho$, of

$$\rho = \frac{\pi d}{\ln 2} \frac{(R_{AB,CD} + R_{BC,DA})}{2} f\left(\frac{R_{AB,CD}}{R_{BC,DA}}\right)$$

where R is resistance (=V/I), d is film thickness, and f is an ideality factor based on the symmetry of the contacts and is unity when $R_{AB,CD}=R_{BC,DA}$. For a sample with magnetic field normal to the surface, the Hall voltage is given as

$$\Delta V = \frac{\mu_H B j \rho}{d}$$

where $\mu_H$ is the Hall mobility and j is current flowing from contact A to C. The Hall mobility can be computed by

$$\mu_H = \frac{d}{B} \frac{\Delta R_{BD,AC}}{\rho}$$

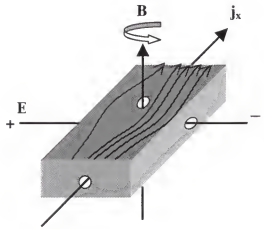


Figure 4-1. Schematic of n-type semiconductor with current, $j_x$, and magnetic field, **B**. Electrons accumulate on one side of the sample creating an electric field, **E**, the Hall field.

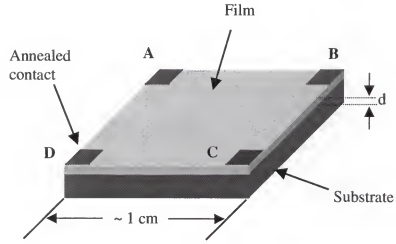


Figure 4-2. Contact geometry of van der Pauw method for performing a Hall measurement.

where $\Delta R$ is the change in resistance caused by the magnetic field. The carrier concentration, n, is then calculated as

$$n = \frac{1}{q\rho\mu_H}$$

with $q=1.6\times 10^{-19}$ coulombs.

Usually, contacts consist of an Hg/In amalgam that has been annealed at 400° C for three minutes under flowing nitrogen. A typical sample size is on the order of 1×1 $cm^2$. This technique is semi-destructive in that the area covered by metal contacts is not recoverable but the rest of the surface can still be examined. In practice, a change in voltage is measured from which $\Delta R$ is calculated, hence it is important that the current used falls within the ohmic region for the sample. Hall measurements are limited by the ability to measure a change in voltage. Usually a variation of several millivolts is required for an accurate measurement. The sample carrier concentration and quality of the contacts will determine the ability to obtain useful data. Samples with less than $10^{16}$ carriers/$cm^3$ will generally not be good candidates for a Hall measurement. In order to avoid carrier depletion problems, films should be at least 200 nm thick (depending on carrier concentration).

4.1.2 Capacitance-Voltage (C-V) Measurement

Another method for determining carrier concentration is based on the fact that semiconductors will acquire a depletion layer capacitance when subject to a reverse bias. The magnitude of the capacitance is a function of the number of carriers. For a one-sided

abrupt junctions. An incremental change in voltage, dV, will result in an incremental increase in charge per unit volume, giving

$$\frac{d(1/C^2)}{dV} \cong \frac{2}{q\varepsilon_s N}$$

where q is the electron charge, N is the carrier concentration, and $\varepsilon_s$ is the permitivity.[40] A plot of $1/C^2$ vs applied voltage will yield a line whose slope gives the carrier concentration. A Hg probe station can be used to quickly and nondestructively form an electrical contact to the sample. No annealing of contacts is required. Commercial systems are available that will interface with the probe station and automatically perform the measurement and calculate a carrier concentration. Sample size can be anywhere from ~1/6 wafer (2") to a full wafer. This method of measurement tends to break down when the semiconductor is degenerate (~$10^{18}/cm^3$)and depletion widths become very narrow.

## 4.2 Structural Characterization

Structural analysis will reveal the overall crystal type of a sample, for example if the film is wurtzitic or zinc blende, and what its lattice constants are. Structural characterization is also performed in order to elucidate the types and number of crystalline defects such as dislocations. Structural imperfections and crystal type will in part determine the electrical and optical characteristics of a semiconductor film. Therefore, crystalline structure information can help develop an understanding of the observed electrical behavior of a sample. Usually, a relationship between the growth

conditions used, the resulting crystalline structure, and electrical behavior can be established. This information can then be used to direct future research.

4.2.1 X-ray Diffraction (XRD)

This technique is based on the diffraction behavior of photons in a crystalline lattice. Bragg established the relationship between wavelength, λ, and lattice dimension, d, as $n\lambda = 2d\sin\theta$, where theta is as shown in figure 4-3. In this construction, it is assumed that specular reflection of the incident radiation occurs. Then, constructive interference of photons will occur when the path difference, 2dsinθ, is an integer multiple, n, of the wavelength. An x-ray diffractometer (see figure 4-4) will scan through all angles theta and detect any reflected energy. When the Bragg condition is satisfied for a family of planes (i.e. (0002) or (0004)), the intensity of diffracted energy collected by the x-ray detector will increase. A plot of detected intensity versus angle can be generated. The instrument used for this study was a Phillips Electronic Instruments APD 3720, located in the Major Analytical Instrumentation Center (MAIC)

The peak positions will be characteristic of a sample with a certain structure and lattice constant. The composition of ternary alloys can be estimated from peak position as well. For example, if a sample of $In_xAl_{1-x}N$ has a peak between the (0002) InN and (0002) AlN peak, it may be inferred from Vegard's law and the relative position of the intermediate peak, what the value of x is.

Intensity peaks will have some broadening from variations in lattice constant due to thermal energy vibration. Peak width can give an indication of the number of linear or planar defects in the sample. This results from variations in the lattice constant around a

defective region. In this case, the Bragg condition will be met for more than one narrow set of angles. The more defective the sample, the broader the characteristic peak.

The signal detected will be a function of the film thickness. Usually, samples should be on the order of 400 nm or more to get useful information. XRD is a completely nondestructive technique that can be done relatively quickly (an hour or less). Samples are mounted onto a glass slide using double-sided tape. This assembly is placed in an enclosed stage that allows x-rays from the source to diffract into the detector. Since x-rays are extremely dangerous, safety protocol must be followed when operating the equipment.

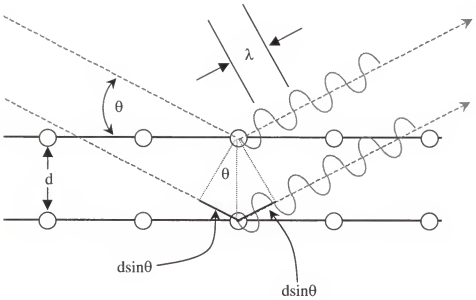


Figure 4-3. Schematic of photon diffraction off of a crystal lattice satisfying the Bragg condition, leading to constructive interference at angle of incidence, θ.

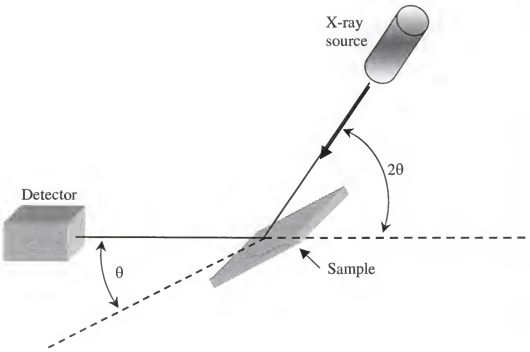


Figure 4-4. Geometry of sample, x-ray source, and detector used for x-ray diffraction studies.

4.2.2 Transmission Electron Microscopy (TEM)

TEM is a powerful tool that relies on the ability of a high-energy electron beam to transmit through a sample. A filament is used to generate a stream of electrons that is collimated by a series of electromagnetic lenses. This beam is then brought to bear on a specimen. More lenses are used to collect the diffracted and transmitted electrons. Contrast is generated by variations in scattering of the electron beam by the sample. Magnification up to 1,000,000X is possible for certain samples when the instrument is in the hands of a competent operator. Information on crystal structure including type, lattice constant, and defect density is obtainable. Figure 4-5 illustrates how contrast formation occurs allowing imaging of line defects. Exceptional imaging of heterostructure interfaces is also possible showing threading dislocations and any residual surface contamination.

Unfortunately, TEM requires samples that are thin enough to allow electrons with energies of ~ 100 KeV to be transmitted. This requires samples to be thinned to approximately 100 nm or less, an often difficult task. Sample prep for cross-sectional imaging starts by gluing a stack of layers together that contains the sample of interest bonded face to face as seen in figure 4-6. This makes handling of the specimen easier for the subsequent thinning steps. Typically, thinning is initiated with sandpaper of increasingly fine grade. Special lapping films and grinders are then used to polish the sample further. A specially designed instrument known as a dimpler is used to etch a concave depression in the sample. Final thinning is done with an ion-mill. Sample preparation is an art that can take years to perfect.

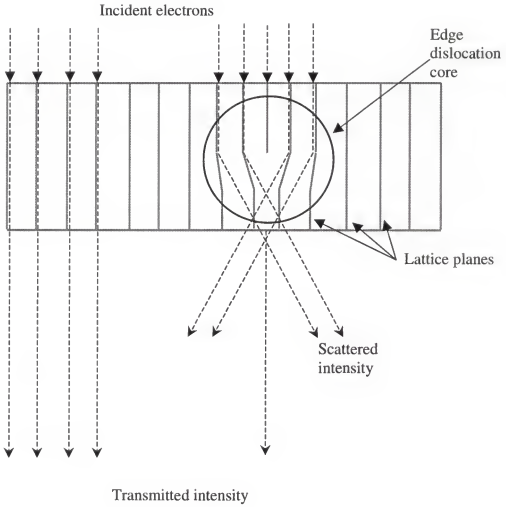


Figure 4-5. Schematic of electron/ sample interactions leading to contrast formation around a dislocation.

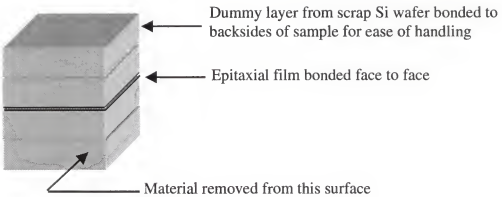


Figure 4-6. Sample stack glued for cross sectional TEM sample prep. Each layer is cut from a wafer and is ~ 5×5 mm.

Along with sample preparation, sample imaging can be a skill that takes many months, if not years to develop. For this reason, only samples perceived as having exceptional qualities are selected for TEM analysis. Sample prep and imaging for this work was conducted by fellow Abernathy lab mate Brent Gila. The instrument used was a JEOL 200CX at MAIC.

## 4.3 Morphological Characterization

Information on surface roughness can be invaluable, especially when film smoothness is critical, as is the case when developing multilayer structures. An examination of the surface of a sample can give clues about growth evolution and film structure. Establishing a relationship between epilayer growth conditions and surface morphology is the desired goal.

Often, surface features of interest may not be revealed with standard optical microscopy. In such cases, scanning electron microscopy (SEM) or atomic force microscopy (AFM) can be used to assess film surfaces.

### 4.3.1 SEM

Most of the SEM images for this work were generated at MAIC on a JEOL 6400 instrument. This machine can usually obtain excellent images up to 25000X for most semiconductor samples studied. Figure 4-7 shows a generalized schematic illustrating the principle of operation for SEM. An electron beam (10 to 20 KeV) is rastered across the sample surface using electronically controlled deflection coils. The electron beam rastering is synchronized with a cathode ray tube so the $x$ and $y$ positions for the electron beam and the CRT are in phase. A secondary electron detector generates a signal that modulates the brightness of the CRT. The intensity of secondary electrons detected will be a function of the sample topography, as illustrated in figure 4-8. Secondary electrons will be deflected toward or away from the detector depending on the slope encountered by the incident electron beam.

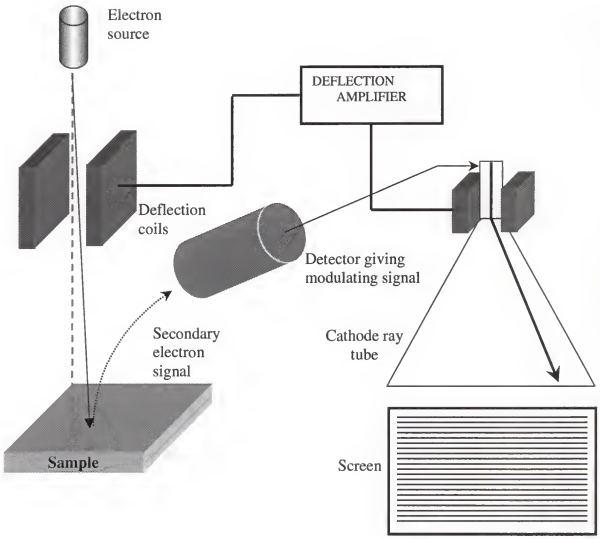


Figure 4-7. Schematic illustration of SEM operation. An electron beam is rastered across the sample in phase with the CRT signal. A secondary electron detector modulates the signal, generating the image on the screen.

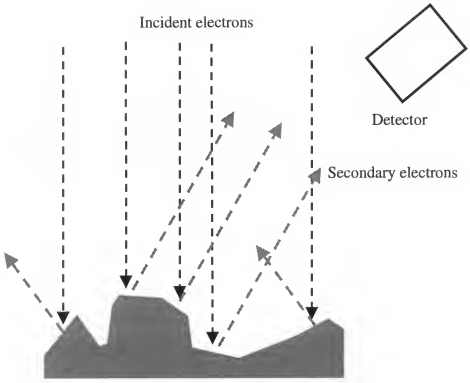


Figure 4-8. Schematic of contrast formation from surface topography. Secondary electrons scattered toward the detector contribute to bright areas on the CRT image.

A sample (as small as can be easily handled, usually ~ 1 $cm^2$) is mounted to an aluminum stub with carbon paint. Carbon paint is required to form electrical contact between the sample and the stub. If the sample is not grounded in this manner, charge will accumulate and degrade image formation. If the sample is insulating it must be coated with a thin film of conductive metal, usually gold/palladium, to avoid charging. Most semiconductor samples examined were conductive enough to bypass this requirement. The properly prepared sample is then loaded into the evacuated SEM column. The internal componentry including electron source, detector, and sample must be housed in an evacuated column to avoid gas phase interactions with the electron beam.

Usually a plan view image is easily acquired in less than 30 minutes. It is sometimes possible to image a cross-section of the sample when the film-substrate interface is oriented normal to the electron beam. When done properly, film thickness can then be accurately evaluated. Having an accurate image of an epilayer surface is the cornerstone of sample analysis and SEM is a relatively operator insensitive and reliable method of obtaining such information.

### 4.3.2 AFM

Atomic force microscopy is a method of acquiring a three-dimensional image of a surface with up to atomic resolution. The primary advantages this technique has over SEM is that it can quantify a root-mean-square (rms) surface roughness and does not require electrical grounding. The technique relies on piezo-driven positioning equipment that can raster an atomically sharp probe tip across a surface as illustrated in figure 4-9. When the probe tip is scanned along a surface, it will deflect the cantilever as it traces over surface roughness. This will cause variations in reflected beam intensity reaching

the quad-photodetector array. Computer software interfaced with the piezo-positioners and photodetectors is able to use this information to develop a three dimensional image of the surface.

The software can also analyze the data and derive numerical descriptions of the surface such as RMS roughness. This is calculated as

$$RMS = \sqrt{\frac{\sum \left(Z_i - Z_{avg}\right)^2}{N}}$$

where $Z_i$ is the current height, and $Z_{avg}$ is the average of N values.

The MAIC facility contains a Digital Instruments Nanoscope III AFM. With this device, it is possible to select a range of scan sizes, usually on the order of 10 × 10 microns. This area is usually sufficient for extracting the most useful information from a sample. Drawbacks of this technique include a sensitivity to operator supplied hardware settings. Large variations in RMS value can be obtained from small changes in the settings used to take data. Additionally, probe tips are extremely fragile and damage to them can yield erroneous images and RMS values. The instrument seems to give differing results for the same specimen on different days or when operated by different users. It is therefore a good idea to support the data derived from AFM with SEM images. This ensures that the AFM is functioning properly and providing useful data. One should also take care in how much meaning is placed on RMS values. For example, vastly different surface

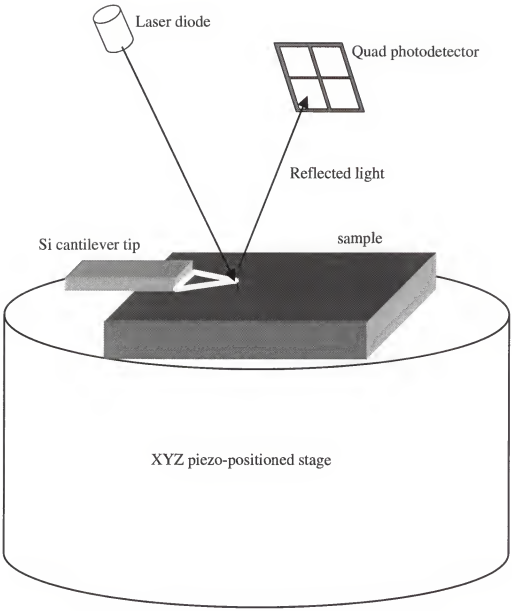


Figure 4-9. Sample and hardware arrangement for AFM

morphologies seen in the SEM might yield very similar RMS roughness values. Also, if surface roughness can be experimentally controlled only to a very crude degree, i. e. rough, medium, or smooth, it makes little sense to report RMS roughness values to a tenth of a nanometer.

4.3.3 Profilometry

One of the easiest and most reliable ways of obtaining sample growth rates is with stylus profilometry. The technique involves measuring film thickness at a step edge using a scanning stylus. A step can be formed in two ways: by masking a small region of the substrate before growth is initiated, or using a selective etch to remove a small area of film down to the substrate.

Substrate masking is done by indium bonding a tiny (~ 2 × 2 mm) scrap piece of Si wafer to the substrate prior to placing it into the load-lock. The key is to use enough indium to bond the Si chip while leaving some surface under the chip uncoated. This allows the chip to act as a shadow mask, leaving a sharp edge that can be traced by the profilometer. Additional care must be taken to ensure the chip is flush against the substrate so growth will not occur beneath it. When growth is completed, the chip is removed by gently heating the substrate to melt the indium. Disadvantages of this approach are that some substrate surface area is sacrificed and the Si chip may de-bond during growth.

When using the selective etch method, a small piece ($< 0.25\ cm^2$) of the sample is cleaved out and masked with an etch resistant polymer such as black wax. For nitrides, a plasma etch is usually necessary to remove the film without affecting the substrate. After

etching, the wax is removed with a solvent, revealing a sharp step. This method is more time consuming than the Si chip method, but tends to be more reliable.

After a suitable step has been formed, the sample can be positioned on the profilometer stage for measurement. The hardware is computer controlled and a film thickness can be determined in just a few minutes.

## 4.4 Compositional Analysis

It is often important to have an accurate assessment of the quantities and types of elements comprising a sample. When constructing ternary compounds, i. e. $In_xAl_{1-x}N$, one selects growth conditions that should yield a film with a prescribed value of x. However, precise compositional control can be difficult, especially in the early stages of investigation, and sample analysis must be conducted to evaluate the relative amounts of its constituents. Moreover, the concentration and types of electrically active impurities must be discerned if a full understanding of the electrical properties of a sample is sought. The two types of information, composition and impurity concentration, may be derived by several means including x-ray photoelectron spectroscopy (XPS), energy dispersive spectroscopy (EDS), wavelength dispersive spectroscopy (WDS), and electron probe microanalysis (EPMA). This section will discuss the two methods most widely employed for this work: Auger electron spectroscopy (AES) and secondary ion mass spectroscopy (SIMS).

### 4.4.1 AES

Auger electron spectroscopy relies on an electron beam probe (3-5 KeV) of a sample that generates Auger electrons possessing characteristic energies which are

collected by an energy analyzer. One example of Auger electron formation is illustrated in figure 4-10. The Auger electron energy will be a function of the binding energy of the intermediate electrons involved and the work function, $\phi$, of the atom. Since $\phi$ is usually much less than the electron binding energy, it can safely be neglected. For a Si atom, as an example, the K shell electrons have a binding energy of ~ 1.8 KeV. A vacancy here will typically be filled by the decay of an L shell electron, binding energy ~ 0.1 KeV. Sometimes, the remaining 1.7 KeV of energy will be relieved by the emission of an X-ray. Usually, the energy will be relieved by the ejection of another L shell electron, whose kinetic energy will be 1.6 KeV after subtracting its binding energy. This process is known as the KLL Auger transition.

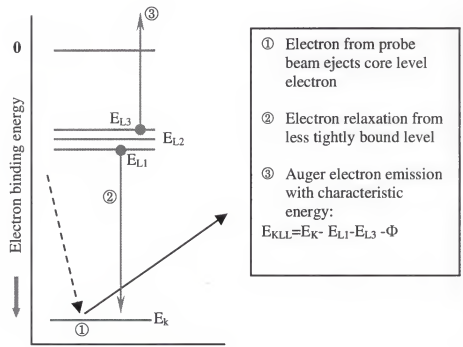


Figure 4-10. Energy diagram showing process leading to Auger electron emission.

A plot of number of electrons detected versus electron energy can be generated. Peak positions and intensities can be used in conjunction with sensitivity factors to obtain quantitative information about composition. The approach is useful for determining the gross composition of a sample to within ± 5 atomic %. The method samples the first few atomic layers of a film (see figure 4-11) and can be used to detect all elements except H and He. Figure 4-11 is a useful guide for judging the volume of a sample probed, and hence resolution attainable, by different electron beam techniques.

The instrument at MAIC used for this work is a Perkin-Elmer PHI 660 Scanning Auger Multiprobe, operated by Mr. Eric Lambers. This device is equipped with secondary electron imaging capabilities and has a lateral resolution of down to 0.5 microns. In addition, an argon ion gun is attached and can be used to sputter samples to obtain composition as a function of depth. This feature is especially useful when analyzing multi-layer structures. When the sputter rate of a sample is known, a plot of composition versus depth can be constructed. Minimum sample size is roughly 3 mm in diameter. No sample prep is necessary but the technique is destructive if sputtering is used. The primary disadvantage of AES is that it can be difficult to analyze samples whose constituents emit Auger electrons with similar energies. This is the case for InN. Here, the In MNN transition is at ~ 410 eV and the nitrogen KLL transition is at ~ 395 eV.

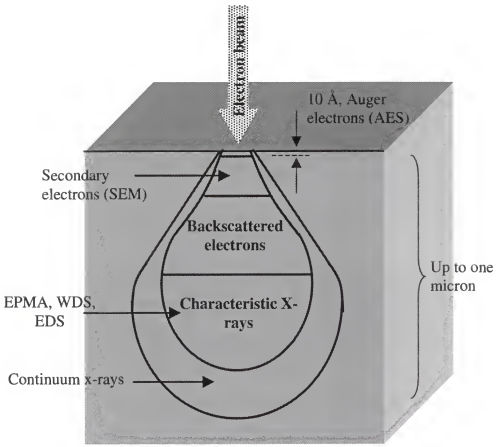


Figure 4-11. Cross-sectional view of interaction volumes for various electron beam probe techniques. The width of the interaction volume represents the resolution of the technique

4.4.2 SIMS

Secondary ion mass spectroscopy is an extremely sensitive technique used to quantitatively measure concentrations as low as $10^{12}$ atoms/cm$^3$, making it ideal for analyzing dopant and impurity levels. The principle of operation is illustrated in figure 4-12. A primary beam of ions, usually oxygen or cesium, with energies from 1 to 20 KeV is impacted on a sample. The transfer of momentum will eject neutral and charged species. Ejected ions can be analyzed in a mass spectrometer where they are separated according to their charge to mass ratio and counted.

SIMS can be used to measure any element from H to U but requires standards to obtain quantitative information. A plot of concentration versus depth can be derived showing matrix and impurity element levels for any structure. Samples as small as a few mm in diameter can be examined. All SIMS analysis done for the Abernathy group was performed by R.Wilson.

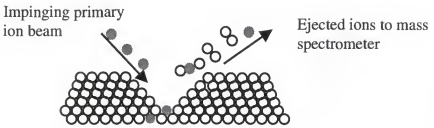


Figure 4-12. Diagram of SIMS sputtering and analysis process.

# CHAPTER 5
# InN EPITAXIAL GROWTH

The primary candidate for an ISL to large-gap nitrides is InN. The relatively small bandgap and potential for grading from other III-N's make it an excellent choice. Figure 5-1 shows an approximate band diagram for an ISL using n-InN. The relative band offsets used to construct the diagram are adapted from Wang *et al.*[41] In addition, the further development of red light emitting devices from the III-nitrides will require the use of InN or very In-rich InGaN active layers. Consequently, understanding the electrical and optical behavior of InN is an important task. A survey of past work on InN thin film growth will be presented. The current chapter examines past methods used to deposit epitaxial InN films and introduces the specific details for InN sample development in the Abernathy lab. Most work focused on optimizing the InN crystal quality and developing an understanding of the origin for the observed n-type behavior of as-grown films.

## 5.1 History of InN Growth

The development of InN is not as mature as GaN in part due to the difficulty of preparing In containing films (owing to indium's low sticking coefficient and the high nitrogen vapor pressure above InN). This section will review the status of InN, focusing particularly on reported mobilities and carrier concentrations. All of the InN films reported in the literature consist of wurtzitic oriented crystallites unless otherwise noted.

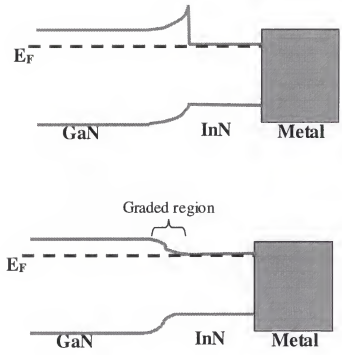


Figure 5-1. Schematic band diagram of ISL using InN. The bottom diagram shows the effect of using a continuously graded region going from GaN to InN.

Indium nitride films were first investigated by Hovel and Cuomo in 1972.[42] They used RF sputtering to obtain polycrystalline films having mobilities on the order of 200 $cm^2/V·s$ with electron concentrations of $7 \times 10^{18}$ $cm^{-3}$. Tansley and Foley[43] reported RF sputtered films with mobilities of >1000 $cm^2/V·s$ at 150 K having an electron concentration as low as $3 \times 10^{16}$ $cm^{-3}$. Sullivan *et al.* used a magnetron sputtering system to deposit poly-InN on glass or fused quartz.[44] They obtained films with 3 to $6 \times 10^{20}$ electrons/$cm^3$ having mobilities of 6 to 10 $cm^2/V·s$. MOCVD was used by Matsuoka *et*

*al.* to deposit nominally single crystal films, as determined by RHEED and XRD, epitaxially on sapphire substrates.[45] Mobilities of 300 to 400 $cm^2/V \cdot s$ were achieved with carrier concentrations of $10^{18}$ $cm^{-3}$. Kistenmacher *et al.* studied the effect of film growth and AlN buffer layer growth temperature on electrical properties of reactively sputtered InN films on sapphire.[46] Samples had ~$2 \times 10^{20}$ $cm^{-3}$ carriers with a maximum mobility of 60 $cm^2/V \cdot s$, largely independent of buffer and film growth temperatures. Strite *et al.* reported the observation of zincblende InN grown on GaAs with MBE.[47] These films appeared to be highly defective single crystal in XTEM micrographs. Mobilities of 220 $cm^2/V \cdot s$ with carrier concentrations of $10^{20}$ $cm^{-3}$ were measured. A modified MBE system was used to deposit films by Sato and Sato.[48] Samples had mobilities of 35 $cm^2/V \cdot s$ with electron concentrations of $3.2 \times 10^{20}$ $cm^{-3}$. Figure 5-2 summarizes the work done to date reported on InN film growth.

One feature common to all InN films is their n-type autodoping. All reported samples, regardless of preparation technique, have very high background electron concentrations as grown. If p-type ohmic contacts to large gap nitrides using an InN ISL are to be fabricated, electron concentration reduction to levels that can readily be compensated by Mg is essential. To illuminate the origin of n-type autodoping, a series of experiments were conducted to determine if the predominant contributor was point defects, structural defects, or impurities. The variables examined were substrate temperature, nitrogen plasma condition, substrate type and pregrowth treatment, and indium precursor.

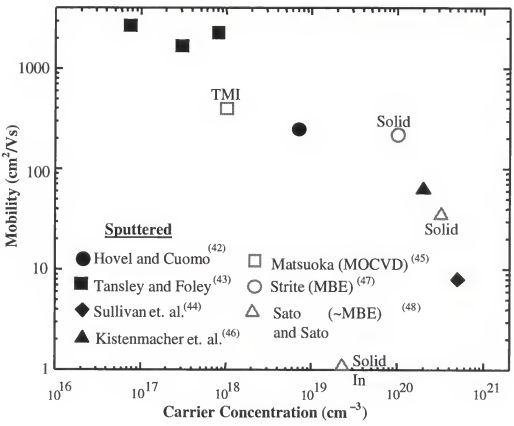


Figure 5-2. Summary of InN film properties reported in literature.

## 5.2 Role of Nitrogen Plasma and Substrate Temperature

The effects of varying nitrogen plasma condition and substrate temperature on the resulting electrical and structural properties of epitaxial InN films have been investigated.[49] Two nitrogen plasma sources were utilized, ECR and RF. Samples were grown on epi-ready (100) GaAs substrates.

### 5.2.1 Sample Loading

Two-inch GaAs wafers were cleaved into quarters and mounted on two-inch Si backing wafers using indium. The Si wafer was heated on a standard hot-plate to melt a small amount of indium. The GaAs piece was carefully placed over the melted indium to avoid thermal shock. Using two sets of stainless steal tweezers, the ¼ wafer was manipulated over the Si until complete indium wetting of both surfaces occurred. Care must be taken to avoid contact with the top surface of the GaAs. Any excess molten indium is scraped away with a razor blade. When growth rate information is needed, a small chip ($< 1$ cm$^2$) of scrap Si is indium mounted for post-growth profilometry. Once the substrate has been indium mounted, the backing wafer is loaded onto a moly block. The block is specially designed to interface with a trolley that transports blocks between the load-lock and buffer chamber. The trolley is placed into the load-lock which is then pumped down. Once the pressure has reached $< 10^{-6}$ torr, the gate-valve separating the load-lock from the buffer is opened and the trolley is moved to the buffer. When the buffer chamber pressure is below $10^{-7}$ torr, blocks are transferred from the buffer to the growth chamber using a magnetically driven transfer rod.

Once in the growth chamber, reactive group V species are introduced, in this case nitrogen from the plasma source. The sample is then rotated from the transfer position to the growth position. Substrate rotation is set to 15 rpm to ensure uniformity across the sample surface. The above mentioned procedure is standard for all work done in the Abernathy MOMBE lab.

5.2.2 Sample Growth

Since no effort is made to clean substrates *ex situ* it is necessary to prepare the GaAs surface by exposing it to nitrogen plasma at ~625° C before growth is initiated. This effectively removes the oxide that resides on the GaAs surface. Substrate temperature is monitored with a thermocouple that is connected to a Eurotherm temperature controller. Temperature set-point is maintained by the automatic adjustment of current or voltage fed to the substrate heater. Differences in set-point and actual substrate temperature can be determined by observing the melting point of InSb (m. p. = 525° C) or GaSb (m. p. = 712° C) chips In mounted to the substrate. When establishing such temperature off-sets, it is essential to maintain a group V flux to avoid decomposition of the calibration chips.

A He carrier gas flow of 7.5 sccm was used to transport trimethylindium (TMI) to the reactor. The TMI bubbler was maintained at 11.4° C and 20 torr. The ECR plasma source (Wavemat MPDR 610) operated at 2.45 GHz and 200 W forward power with ultra-pure nitrogen flowing at 20 sccm. This source is fitted with a TiN coated Mo grid connected to an independently controllable power supply. During growth, a floating bias of –15V is reached, as measured by a portable multimeter. Errors in measurement of this value may occur due to electromagnetic interference from the plasma source. The rf

plasma source (SVT Associates) was operated at 13.56 MHz and 400 W forward power with 5 sccm nitrogen flow.

Figure 5-3 shows SEMs of ECR derived InN grown at 525, 575 and 625° C. Surface roughness, as measured by AFM rms values, also increases with substrate temperature, as plotted in figure 5-4. Caution must be exercised when examining rms roughness values, however. The surface morphologies of samples grown at 525 and 575° C are quite different as seen in the SEMs, but their rms roughness values are very similar (18.1 vs 20.4 nm). Conversely, morphologies of material grown at 575 and 625° C appear similar while having a large difference in rms values (20.4 vs 67.2 nm).

Crystallinity, as measured by the hexagonal (0002) FWHM X-ray peak, increases with substrate temperature, depicted in figure 5-4. The maximum growth temperature is limited, however, by the desorption of indium from the surface. In fact, at 675° C, virtually no growth takes place. A marked increase in electron mobility was observed when the substrate temperature increased from 525 to 575° C, diminishing slightly when increased to 625° C, see figure 5-5. This improvement in mobility is most likely due to the improved crystallinity obtained at higher growth temperatures. The electron concentration varied by less than a factor of two for this temperature range, going from $3.6 \times 10^{20}$ at 525° C to a minimum of $1.6 \times 10^{20}$ at 575° C. It is clear that while the crystallinity, surface roughness and mobility of InN grown by ECR plasma are functions of substrate temperature, the electron concentration is largely invariant.

As with growth temperature, plasma biasing strongly affected the structural quality of InN films. X-ray scans show a decrease in FWHM of the hexagonal (002) peak as the ECR grid was biased more negatively (figure 5-6). RMS surface roughness

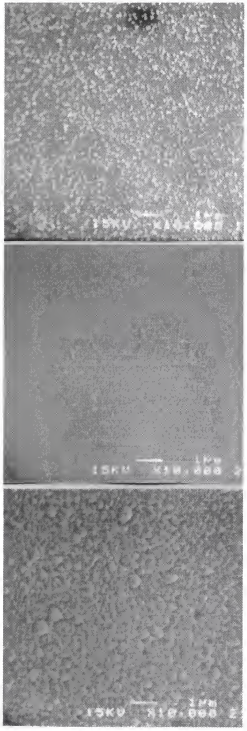


Figure 5-3. Scanning electron micrographs of InN/GaAs derived from ECR nitrogen plasma at different substrate temperatures.

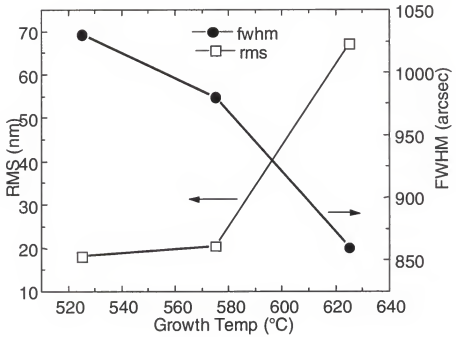


Figure 5-4. RMS roughness and hexagonal InN (002) FWHM vs growth temperature for ECR derived InN.

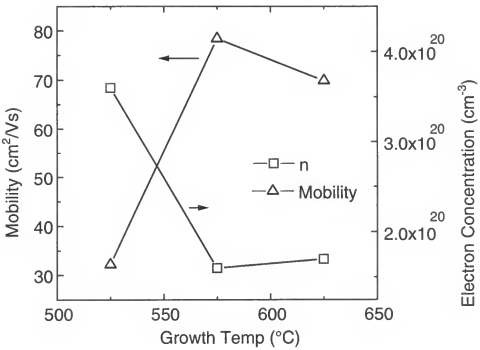


Figure 5-5. Mobility and electron concentration vs growth temperature for ECR derived InN.

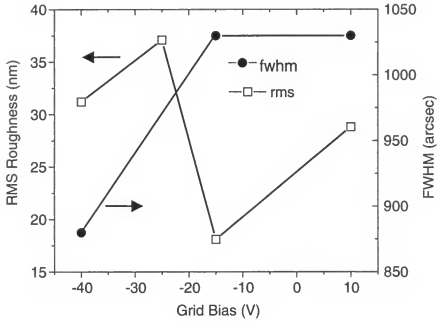


Figure 5-6. RMS surface roughness and hexagonal InN (002) peak FWHM vs grid bias for ECR derived InN.

values do not appear to follow any trend but are of the same order measured for the substrate temperature study. Surface morphologies seen in SEM micrographs are similar for InN grown at – 40 V bias (525° C) and no bias at 625° C (figure 5-7). These samples also share similar crystal quality, having comparable hexagonal (002) FWHM values.

The surface morphology of InN grown at +10 V bias is similar to that grown with a floating bias although there is a reduced density and increase in size of the nodular features. The FWHM of the hexagonal (002) peak is nearly identical for the two films. Electron concentration does not vary significantly with applied grid bias, although the mobility increases by roughly a factor of two for the sample grown under the highest negative bias, as shown in figure 5-8. Carrier concentrations are similar to those found in InN grown at various temperatures with no applied bias.

The fact that the smoothest surfaces, narrowest FWHM hexagonal (002) peaks and highest mobilities are obtained from the ECR plasma biased at – 40 V suggests that increasing neutral N density is beneficial to growth. One way to further examine the role of ions is to compare films derived from ECR plasma with those from rf plasma. The rf source produces higher energy species than the ECR source. RMS roughness values for rf derived InN are similar to those found for samples grown at 625° C using the ECR source. However, the morphology of the two samples is quite different as shown by the SEM micrograph of figure 5-9. The InN grown using rf plasma appears to have hexagonal grains in contrast to the pyramidal grains of ECR derived films. X-ray scans of rf derived material exhibit indications of the zinc-blende phase in addition to the wurtzitic phase prevalent in ECR derived samples. GaN films grown by various methods

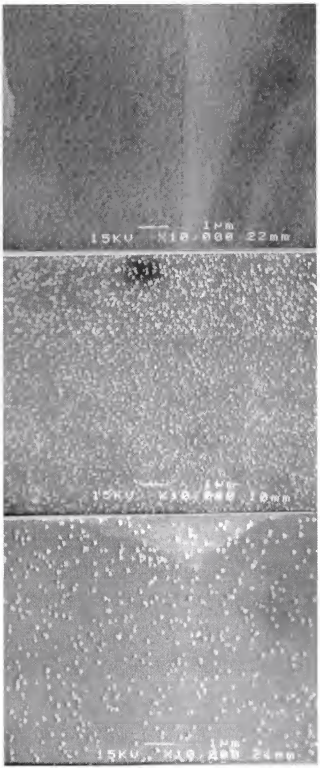


Figure 5-7. SEM micrographs of ECR derived InN grown at 525° C and bias of – 40 V (top), floating (middle), and + 10 V (bottom).

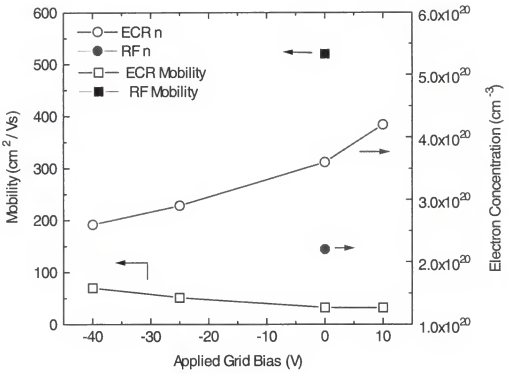


Figure 5-8. Mobility and electron concentration vs applied grid bias for ECR derived InN grown at 525° C. Included are mobility and electron concentration values for rf derived InN grown at 525° C.

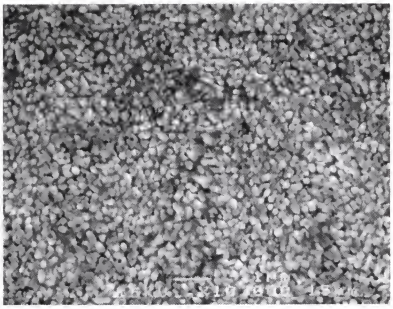

Figure 5-9. SEM micrograph at 10kX of rf derived InN grown on GaAs at 525° C.

on several types of substrates have resulted in mixed phases as well.[50-54] In fact, the rf derived InN did not yield a strong hexagonal (002) peak so such a comparison cannot be made with ECR derived InN. RF derived samples have electron concentrations on the same order as ECR produced samples (figure 5-8) but have significantly higher mobilities, > 500 $cm^2/Vs$. This may indicate that cubic InN has a higher mobility than hexagonal material.

## 5.3 Substrate Effects

Auger electron spectroscopy (AES) was used to examine the nitridation behavior of GaAs, sapphire and lithium aluminate (LAO) substrates exposed to an RF nitrogen plasma.[55]

Four substrates were compared for this study, epi-ready (100) GaAs, c-plane sapphire, LAO (100), and LAO (100) miscut 18°. The miscut LAO is believed to posses matching symmetry as well as lattice dimension for nitride epitaxy. Lithium aluminate has an improved lattice match to III-nitrides with LAO ($a$= 3.13Å) having a near perfect match to AlN ($a$=3.11 Å).[56] This is an important consideration when growing low temperature AlN buffers. The substrates were indium mounted to a Mo block without any *ex-situ* cleaning steps and loaded into the MOMBE system. In order to investigate their nitridation behavior, the substrates were exposed to the RF nitrogen plasma prior to growth initiation. The plasma source was operated at 400 W forward power with 5 sccm $N_2$ flow. Substrates were exposed for five minutes at temperatures of 725°, 775°, 825° and 875°C. Samples were exposed to the plasma during heat-up and cool-down as well. These samples were then removed from the system and analyzed using depth-profile auger electron spectroscopy (AES) and atomic force microscopy.

InN films were grown on the various substrates using trimethylindium (TMI) transported by a He carrier gas. Reactive nitrogen was provided by the RF plasma source operated under the conditions mentioned above. Substrates were maintained at ~525° C giving a growth rate of ~250 nm/hr. Three cases were examined for this study: 1) InN films grown on as received substrates with no prior plasma treatment, 2) InN films grown on substrates that received a plasma exposure of 875° C for five minutes and 3) InN films grown on substrates that received a plasma exposure of 875° C for five minutes and an AlN buffer. The 30 nm AlN buffers were grown at 425° C using dimethylethylamine alane (DMEAA) and RF nitrogen plasma. The DMEAA bubbler is maintained at 9.2° C and 7 torr. A carrier gas of He is used at 10 sccm. Nitrogen plasma is operated at 400 W forward power and 5 sccm nitrogen flow.

Electrical transport properties were obtained from Van der Pauw geometry Hall measurements at 300K using alloyed (400° C, 2 min) HgIn ohmic contacts. Surface morphology was examined by SEM and contact mode AFM.

SEM micrographs of InN grown on sapphire and GaAs are shown in figure 5-10. The top images show InN films grown on as received substrates while the bottom images are of films deposited on RF nitrogen plasma exposed substrates. The surface morphologies of the "no anneal" films are quite rough. The InN surface morphology shows significant improvement in the case of the GaAs substrate that received plasma exposure prior to growth. However, for InN grown on plasma exposed sapphire there is no morphological improvement. The differences in morphology between the two substrates can be traced to differences in nitridation behavior as measured by AES. GaAs samples that received a nitrogen plasma exposure at 875° C for five minutes yield a

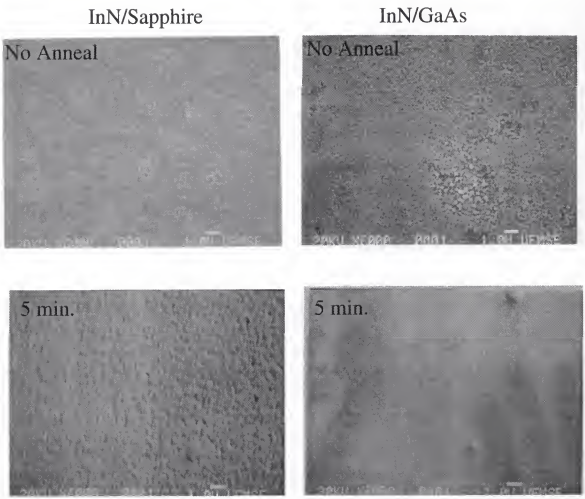


Figure 5-10. SEM micrographs of InN films grown on sapphire (left) and GaAs (right). The top samples were grown on as-received substrates while the bottom samples were grown on nitrogen plasma exposed substrates.

strong nitrogen signal at 385 eV, indicating nitridation of the surface. No such signal is discernible for sapphire substrates given the same treatment. This would suggest that no nitride template is being formed on sapphire under the given nitrogen plasma exposure, resulting in no improvement in morphology. However, work done by Yamamoto *et al.* indicates that nitridation, as measured by electron spectroscopy for chemical analysis, of sapphire can occur under an $NH_3$ flow over a heated (~800° C) substrate.[57] They report a marked improvement in epitaxial InN films grown on nitridated sapphire as measured by in-situ reflection high-energy electron diffraction. Although no nitrogen signal was discernible by AES for sapphire exposed to rf nitrogen plasma, it is evident that plasma exposure prior to growth is important to the final film morphology when an AlN buffer is used. Figure 5-11 shows InN grown over AlN buffers that were deposited on plasma exposed substrates at different temperatures. The importance of substrate temperature during plasma exposure is illustrated by the marked improvement in morphology for samples grown on substrates receiving an 875° C pretreatment.

Next examined were InN films grown on LAO (100). Figure 5-12 shows SEMs of films grown using the three conditions discussed above. The film grown on the as received substrate is seen to be discontinuous and has poor morphology. Notable morphological improvement is seen when the substrate is exposed to nitrogen plasma with even further improvement obtained from the use of an AlN buffer. Figure 5-13 shows SEMs of InN films grown on LAO (100) miscut 18°. Again, the as received substrates yield discontinuous, poorly formed films. Improvements in film continuity are gained by nitrogen plasma exposure prior to growth with best results obtained using an AlN buffer.

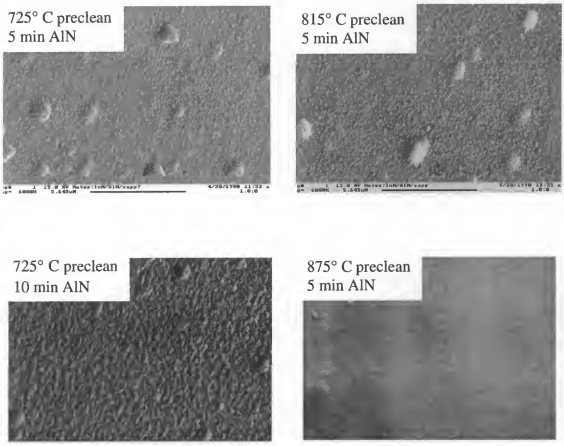


Figure 5-11. SEM micrographs at 6000× of InN grown on AlN buffers. These samples were grown on sapphire substrates using TMI.

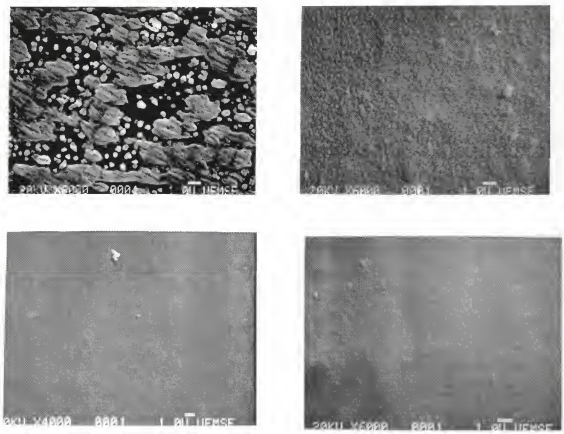

Figure 5-12. SEM micrographs of InN grown on LAO (100) for the three cases discussed in the text. Upper left: no plasma anneal, upper right: 5 min. anneal at 875° C, and lower left: plasma anneal + AlN buffer. InN grown on sapphire using an AlN buffer is shown at lower right for comparison.

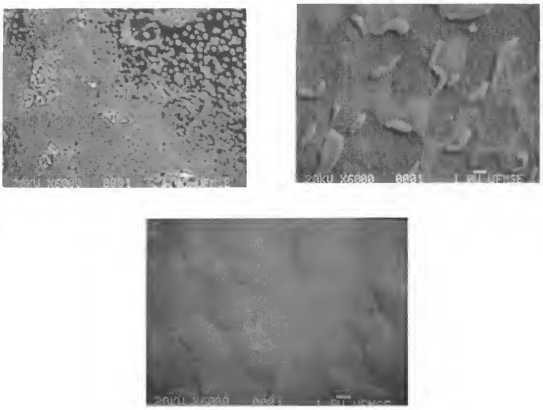

Figure 5-13. InN films grown on miscut LAO (100) for the three cases discussed in the text. Upper left: no plasma anneal, upper right: 5 min. plasma anneal, bottom: plasma anneal + AlN buffer.

AES conducted on LAO (100) exposed to nitrogen plasma for five minutes at 875° C shows no nitrogen peak. This would suggest that although the plasma may not be forming a nitride template as measured by AES, it is affecting the surface in some fashion. Nitrogen termination not detectable by AES may be present, however. Similarly, miscut LAO (100) substrates exposed to an rf nitrogen plasma for five minutes at 875° C do not show evidence of nitridation as measured by AES. The observed differences in morphology between InN grown on as received substrates and plasma exposed substrates may be due to cleaning of adventitious contaminants, though this remains to be verified. The dramatic improvement in morphology produced by the AlN buffers is due to the planar surfaces induced by these layers. InN by contrast tends to island severely when grown on highly mismatched or non-III-V surfaces.

Room temperature Hall measurements yield carrier concentrations on the order of $10^{20}$ $cm^{-3}$ as seen in figure 5-14. The background electron concentration was found to be relatively insensitive to substrate type and to pre-growth surface treatment. By contrast, the mobilities dropped substantially as the surface morphology was improved through the various pre-growth treatments. This effect has also been observed in GaN grown by MOCVD[58] and suggests some form of gettering.

The results of AES on LAO (100), LAO (100) miscut and sapphire substrates exposed to an RF nitrogen plasma for five minutes at 875° C indicate no significant nitridation occurs. Since differences in morphology are observed for InN films grown on exposed versus unexposed substrates, there may be some cleaning effect taking place during exposure. By contrast, GaAs substrates show evidence of nitridation with exposure to the nitrogen plasma. Nitrided GaAs leads to smooth InN growth without the

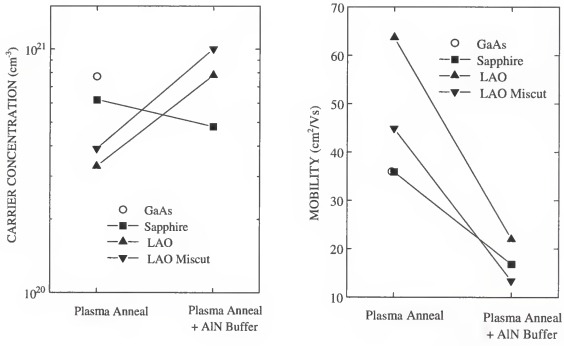


Figure 5-14. Electron concentrations and mobilities of InN films given by room temperature Hall measurements.

use of AlN buffers due to the presence of a smooth GaN template. Comparable InN morphology is obtained when AlN buffers are used on LAO and sapphire substrates. Hall measurements indicate background carrier concentrations are relatively insensitive to substrate type, suggesting that the background electron concentration is probably not related to misfit dislocations since it is expected that these defects would vary significantly for the variety of substrates used in this study.

## 5.3 Indium Precursor

In this section, the effect of using different indium precursors for the growth of InN films is examined. Samples were grown on basal plane sapphire using TMI, solution TMI and solid In. The purpose of this study was to determine what role, if any impurities play in determining electrical properties of InN. Impurities are an especially critical issue for nitride growth owing to the exceptionally high bond strength of nitrogen. Generally, nitrogen vacancies have been attributed to the unintentional doping observed for as-grown InN.[59] However, theoretical studies indicate that impurities such as oxygen or carbon may contribute to the electron background.[60] As well, it is possible to anticipate the behavior of carbon in compound semiconductors from a phenomenological basis. By examining the relative bond strengths of group III species with carbon and group V species with carbon, it is possible to construct a plot using known maximum carrier concentrations that will predict the electrical role of carbon. Figure 5-15 shows such a construction. Because the N-C bond is relatively strong, C would prefer to reside at an In site, acting as a donor.

Examining different precursors that contribute varying quantities of impurities should enable a determination of the role of impurities on the electrical properties of InN.

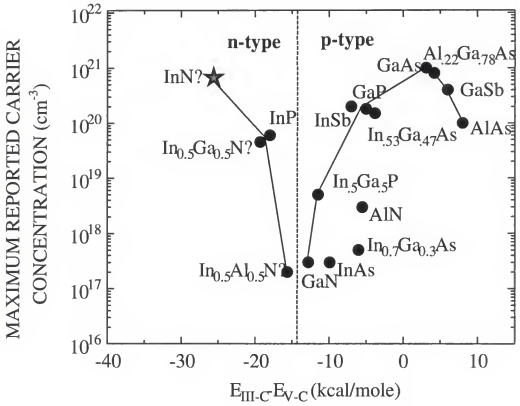


Figure 5-15. Plot of maximum reported carrier concentration versus difference in bond strength for carbon with a group III and group V atom. The carbon atom is expected to reside on an In site, acting as a donor. [after references 61-71]

5.4.1 TMI Derived InN

Samples were grown on 2" silicon back-side coated sapphire. The silicon coating is intentionally rough to facilitate absorption from the substrate heater. Without the silicon, little coupling of the substrate heater energy with sapphire would occur. A He carrier gas (flow = 7 sccm) was used to transport TMI to the growth chamber. The bubbler was maintained at 12.3° C resulting in a growth rate of ~150 nm/hr.

Experimental mapping of growth condition parameters such as substrate temperature, growth rate, and V/III ratio determined the best conditions for InN growth on sapphire. Best results are obtained when an rf nitrogen plasma exposure of the substrate is made, followed by a low-temperature AlN buffer. The substrate exposure is conducted at ~875° C for five minutes with 5 sccm nitrogen and 400 watts forward power. Low temperature buffer layers are grown using conditions previously described.

Figure 5-16 shows a cross-sectional TEM micrograph and its corresponding selected area diffraction pattern for InN derived from TMI using optimized conditions. The sample is a highly defective single crystal with dislocation densities comparable to those found for GaN and AlN grown on sapphire. This is the first TEM observation of single crystal hexagonal InN. All InN films derived from TMI exhibit the familiar n-type autodoping with electron concentrations in the $10^{20}$ to $10^{21}/cm^3$ range. Carrier mobilities similar to those reported for other deposition techniques were measured as illustrated in figure 5-17. SIMS analysis of these films shows both carbon and oxygen to be present in high concentrations, on the order of $10^{20}$ to $10^{21}/cm^3$. The carbon probably arises from

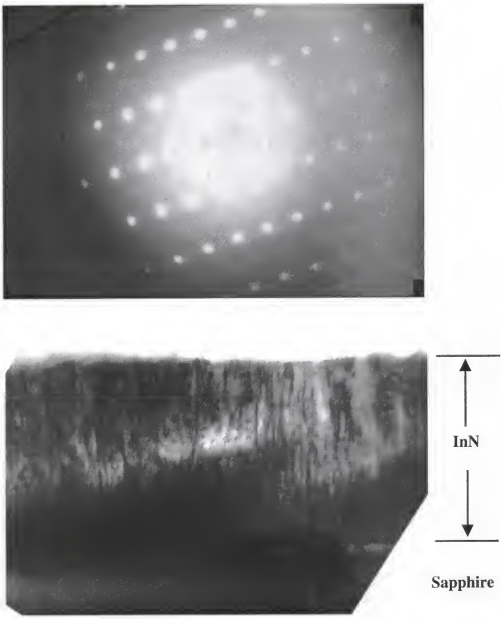


Figure 5-16. XTEM micrograph, bottom, and selected area diffraction pattern, top, of InN derived from TMI on sapphire. The absence of streaks in the SAD pattern is indicative of single crystal material.

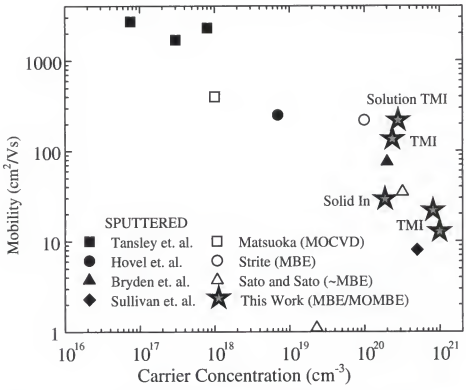


Figure 5-17. Mobility vs. electron concentration for InN grown using various techniques and sources.

methyl radicals released by the pyrolysis of TMI, while oxygen most likely is introduced by residual ether left over from TMI synthesis.

5.4.2 Solution TMI Derived InN

Solution TMI differs from regular TMI in that an ether-free synthesis process is used leading to a modified molecular structure. A comparison of solution TMI with standard TMI is given in figure 5-18. In solution TMI, dimethyldodecylamine (DMDA),

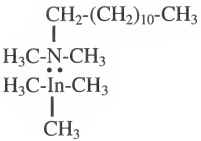


**Solution TMIn**

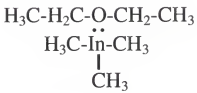


**Standard TMIn**

Figure 5-18. Comparison of TMI with solution TMI molecule. In the solution TMI, the ether group is displaced by dimethyldodecylamine (DMDA).

used to liquefy the TMI, is believed to displace the ether group commonly associated with the molecule. SIMS analysis reveals that carbon levels of $1.9 \times 10^{20}/cm^3$ are present, similar to levels found in samples derived from regular TMI. However, the oxygen background was found to be $8 \times 10^{18}/cm^3$, significantly lower than TMI derived samples. This lends credence to the identification of ether as the source of oxygen in standard TMI derived samples. Hall measurements show carrier concentrations and mobilities for solution TMI derived samples to be comparable with values reported in the literature for other fabrication methods, figure 5-17.

SEM micrographs of solution TMI derived InN films grown on sapphire are shown in figure 5-19. Surface morphologies are seen to be dissimilar to TMI derived samples grown with the same 725° C pretreatment and 5 minute AlN buffer. This may be attributed to differing surface mobilities with the absence of ether in the solution TMI. One would expect a smoother morphology to emerge for samples grown on substrates receiving an 875° C preclean because the liquid and solid versions of TMI should have similar surface mobilities resulting in similar morphologies.

### 5.4.3 Solid In derived InN

Samples were grown on sapphire or GaAs substrates using a standard MBE type effusion oven to provide an indium flux. Figure 5-20 shows micrographs of InN grown on sapphire and GaAs. The sample morphologies illustrate the poor surface mobility of the solid In precursor compared with metalorganic TMI derived films. Even when using the best plasma pretreatment condition (875° C, 5 min), solid In derived samples do not exhibit the smooth surfaces obtained with TMI derived films. The use of a surface-active species to facilitate improved In surface mobility was then attempted. Surfactants are

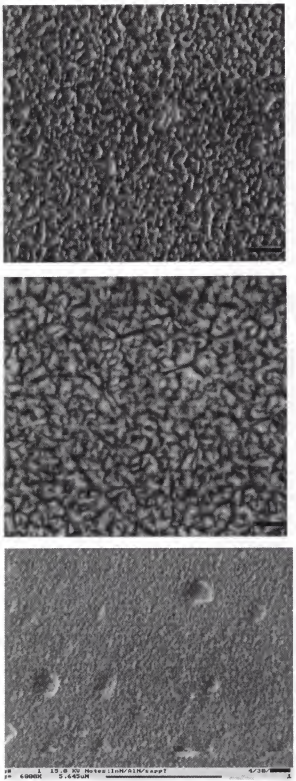

Soln TMI
600 Å/hr
10kX

Soln TMI
2500 Å/hr
10kX

TMI
2000 Å/hr
6kX

Figure 5-19. SEM micrographs of solution TMI derived InN films. For comparison, standard TMI derived material is included that was grown using the same conditions. Micron markers are at bottom right of each image. Note the different scale for the bottom image.

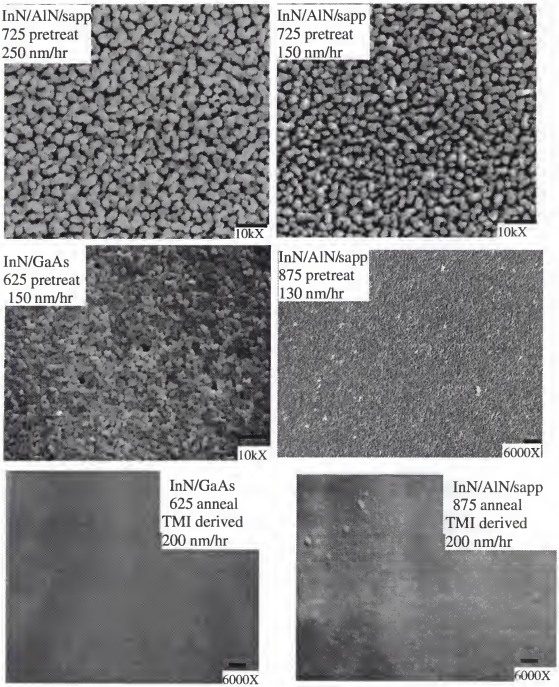


Figure 5-20. SEM micrographs of InN films derived from solid In. The bottom images are of films derived from TMI hilighting differences in In precursor surface mobility. Micron markers are positioned above the magnification.

known to improve surface morphologies by lowering the surface energy of the layer being deposited on. In addition, the surfactant will have a high segregation coefficient severely restricting its incorporation into the growing film. This principle was employed by Copel *et al.* for the growth of Si/Ge multilayers using an As surfactant.[72] For this work, Sb was used as a surface-active agent, provided by an effusion oven held at 500° C. Figure 5-21 shows the resulting morphology for InN deposited on an AlN buffer. The substrate is basal plane sapphire, similar to that used for all other work, receiving a nitrogen plasma pretreatment of 875° C for 5 minutes. As evident in the micrograph of figure 5-21, the morphology was not noticeably improved. Hence, it seems that solid In derived InN may have an unavoidable problem with surface roughness.

Room temperature Hall measurements were conducted on all samples discussed for this section. As with samples derived by other methods, a persistent background electron concentration on the order of $10^{20}/cm^3$ is observed. Mobilities were generally found to be lower, 2 to 6 $cm^2/Vs$, with the highest being ~30 $cm^2/Vs$. The slightly reduced mobility may be attributed to the increased presence of scattering defects in the film. Since the solid In source is expected to introduce fewer C atoms into the growing film as compared to TMI, the observed electron levels are not likely a result of carbon contamination.

## 5.5 Summary of InN growth

The extensive manipulation of growth variables including substrate temperature, nitrogen plasma condition, substrate type and pretreatment, and indium precursor has led to a greater understanding of the nature of epitaxial InN films. Three primary points have been uncovered.

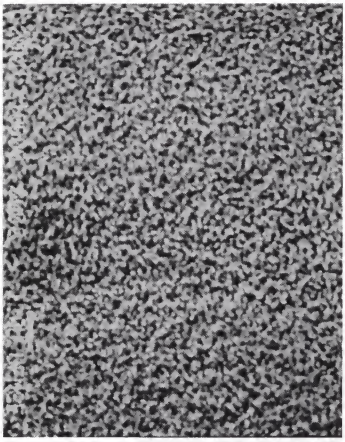

Figure 5-21. SEM micrograph at 10kX of solid In derived InN on sapphire grown with an Sb overpressure.

First, the importance of a high-temperature (~875° C) plasma pretreatment of sapphire prior to growth initiation. Although AES did not detect a nitridated layer, the morphology of resultant films indicates this step is important for obtaining smooth surfaces. It is possible a very thin nitride layer is formed that is beyond the capabilities of AES to detect. Grandjean *et al.* report the development of an AlN layer on sapphire as measured by in-situ reflection high-energy electron diffraction.[73] Their study used $NH_3$ as a nitrogen source with a substrate temperature of 850° C. They report a significant improvement in GaN film morphologies on sapphire receiving a 30 minute nitridation step. The importance of having a nitride template is emphasized when examining InN films grown on plasma exposed GaAs substrates. Here, the nitrogen plasma displaces some As atoms giving a thin GaN layer, which precedes smooth InN growth. Because displacement of As from GaAs is comparatively easy, AES was able to detect a nitrogen signal for those substrates.

Second, the pretreatment must be used in conjunction with a low temperature AlN buffer layer to obtain the best films. It is likely that the nitrogen plasma pretreatment provides an AlN template that facilitates the deposition of an AlN buffer layer. It was observed however, that the AlN buffer layer is ineffectual without the proper nitrogen plasma pretreatment.

Finally, there appears to be no growth condition that will lead to InN films with low background electron concentrations. In order to obtain p-InN it would be necessary to reduce the electron concentration to $<10^{17}/cm^3$ to have a chance at compensating with Mg. Therefore, an alternative to InN must be found to use as an ISL for contacts to p-

type material. The efficacy of p-GaAs contact layers has been investigated and results of its contact performance are reported in Chapter 7.

# CHAPTER 6
# CONTACT STRUCTURES AND PERFORMANCE

This chapter will present the specific contact resistance, $\rho_c$, found for contact structures grown by MOMBE. Contacts to n-type large bandgap nitride films using InN layers were fabricated and their thermal stability was studied. The contact metallization and measurements were conducted by Dr. Fan Ren's group of the UF Chemical Engineering Department.

## 6.1 Contacts to n-Type Nitride Films

InN contact structures were grown on large-gap InAlN, representative of an emitter layer for an HBT.[74] Two basic structures were used for this study, indicated in figure 6-1 to determine the utility of InN contact layers. Since some applications of nitride devices require thermal stability, $WSi_x$ metallization was used for its refractory properties. $WSi_x$ was sputter deposited and patterned for specific contact resistance measurements by the transmission line method (TLM).

The samples were grown on either (0001) sapphire or semi-insulating, (100) GaAs substrates by MOMBE. The group III precursors, DMEAA and TMI were transported by a He carrier gas in order to avoid possible hydrogen passivation effects. The ECR plasma source operating at 2.45 GHz and 200 W forward power was used to provide the nitrogen flux. $N_2$ flows of 5 or 20 sccm were used. Growth temperatures for

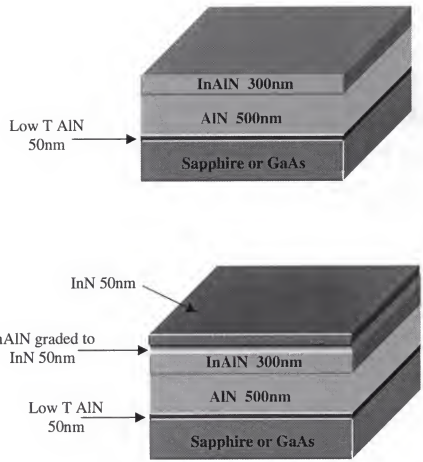


Figure 6-1. Schematic of the two contact structures used for studying InN ISLs. Stucture with no InN cap layer, top, and with cap layer, bottom.

In-containing layers ranged from 500°C to 575°C, while AlN layers were grown at 700°C. The growth sequence on sapphire consisted of a nitrogen plasma exposure step of 5 minutes at 700°C, followed by a low temperature (425°C) 500Å AlN nucleation layer and finally a 5000Å AlN buffer layer. A 500Å graded region between the InAlN and the InN was used to avoid band discontinuities at the InN/InAlN interface. The film compositions were varied by altering the relative group III gas flow rates. Electrical transport properties were obtained from Van der Pauw geometry Hall measurements at 300 K using alloyed (400° C, 2 min) HgIn ohmic contacts. The compositions of the calibration samples were determined by electron microprobe analysis using a 6 kV beam, and by powder x-ray diffraction assuming Vegard's law. Surface morphology was examined by SEM and AFM. X-ray diffraction was used to evaluate the structural quality and to determine that all films grown, including those on GaAs, crystallized in the wurtzite phase.

The initial experiments were conducted on InAlN structures, such as would be used in lattice matched InAlN/InGaN HEMT devices. As shown in figure 6-2, the GaAs substrates produce InAlN surface morphologies comparable to those obtained on sapphire, in spite of the larger lattice mismatch between the GaAs and the epilayer. As expected the addition of the graded region and the InN contact layer roughens the surface considerably, particularly for the structures grown on sapphire. This is also observed for InAs growth on GaAs-based structures and is due in part to the tendency of In materials to island on non-In containing surfaces. This roughening typically becomes worse with increasing In-containing layer thickness, thus limiting the thickness of the contacting

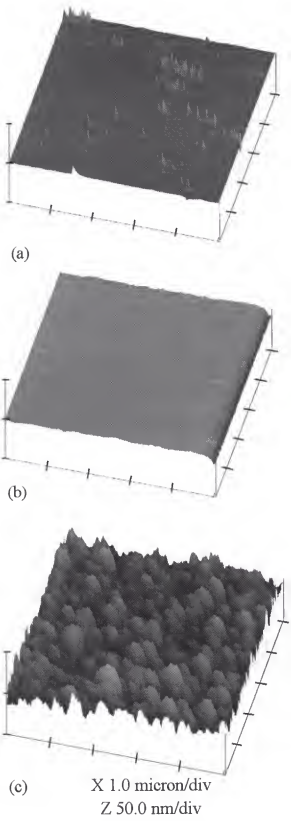


Figure 6-2. AFM scans of InAlN on either GaAs (top) or sapphire (middle), and the InN/InAlN contact structure on GaAs (bottom).

layer which can be used. For this reason the InN layers used in this study were limited to 500Å thicknesses.

In order to evaluate the electrical properties of the materials, Hall measurements were performed on separate 0.3 - 0.5 micron callibration layers grown under the same conditions as those used for the contact structures. This analysis gave mobilities of ~5-15 $cm^2/V\text{-}s$ for InAlN and ~25-50 $cm^2/V\text{-}s$ for InN, and electron concentrations of ~ 1 - 3 × $10^{19}$ $cm^{-3}$ for InAlN films and ~1 - 3 × $10^{20}$ $cm^{-3}$ for InN layers.

Given the similarity in electrical behavior and surface morphology, it was expected that the contact resistances would also be similar in structures grown on the two substrates. However, as listed in Table IV, the structures grown on sapphire produce significantly lower contact resistances. This difference does not appear to be related to doping level as the sheet resistances of the InN cap layers were found to be independent of substrate. It is more likely that the poorer contact behavior is due to the poorer structural quality obtained on GaAs relative to sapphire. XRD analysis of both In- and Al-containing materials shows an approximately twofold increase in FWHM when layers are grown on GaAs rather than sapphire, see Table V. Similar behavior has been reported for GaN as well, with layers grown on GaAs consistently found to be of poorer quality.[75,76] Thus it appears that from the point of view of parasitic resistances, electronic devices fabricated on sapphire will most likely provide superior performance.

Contrary to what has been observed for GaN, where even relatively low In mole fractions ($X_{In}$ ~ 0.25) produce significant improvements in contact resistance,[77] it was found that InAlN contact layers produce unacceptably high contact resistances even at

Table IV. Contact resistance and RMS surface roughness of structures grown using various nitrogen flows and growth temperatures.

| STRUCTURE | CONTACT RESIST-ANCE ($\Omega$-cm$^2$) | AFM RMS ROUGHNESS (nm) | $N_2$ FLOW DURING InN GROWTH (sccm) | InN DEP. TEMP. (°C) |
|---|---|---|---|---|
| InAlN/AlN/Sapphire | $1.9 \times 10^{-5}$ | 1.4 | 5 | 525 |
| InAlN/AlN/GaAs | $1.4 \times 10^{-3}$ | 1.6 | 5 | 525 |
| InN/InAlN/AlN/Sapphire | $4.8 \times 10^{-4}$ | 68.7 | 5 | 525 |
| InN/InAlN/AlN/GaAs | $8 - 9 \times 10^{-4}$ | 7.0 | 5 | 525 |
| InN/InAlN/AlN/Sapphire | $3.6 \times 10^{-5}$ | 20.5 | 20 | 525 |
| InN/InAlN/AlN/Sapphire | $3.5 \times 10^{-6}$ | 54.7 | 20 | 575 |

Table V. Primary XRD peaks for contact layers grown on sapphire and GaAs.

| STRUCTURE | PEAK POSITION (degrees) | PEAK ID | FWHM (arcsec) | $N_2$ FLOW DURING InN GROWTH (sccm) | InN GRTH. TEMP. (°C) |
|---|---|---|---|---|---|
| InN/InAlN/AlN /Sapphire | 31.4 | InN(002) | 1895 | 5 | 525 |
| | 33.5 | InAlN | 12300 | | |
| | 36.1 | AlN(002) | 1420 | | |
| InN/InAlN/AlN /GaAs | 31.4 | InN(002) | 3320 | 5 | 525 |
| | 36.1 | AlN(002) | 2650 | | |
| InN/InAlN/AlN /Sapphire | 35.9 | AlN(002) | 1910 | 20 | 525 |
| | 64.7 | InN(004) | 1800 | | |
| | 76.2 | AlN(004) | 3700 | | |
| InN/InAlN/AlN /Sapphire | 31.4 | InN(002) | 1950 | 20 | 575 |
| | 33.5 | InAlN | 17000 | | |
| | 36.1 | AlN(002) | 1890 | | |

low aluminum concentrations ($X_{Al} \sim 0.25$). Therefore while GaN containing structures may only require fairly low In concentrations for improved performance, structures with

InAlN layers will most likely require pure InN. However, simply adding an InN layer to the growth sequence does not guarantee improved contact performance, as shown in Table IV. While the addition of InN cap layers did reduce the resistance in structures grown on GaAs structures, it actually degraded the performance for structures on sapphire. This may be due to the rougher surface morphology that occurs from the islanding behavior of InN. It was found that by increasing the nitrogen flow from 5 to 20 sccm through the ECR plasma source during growth of the InN the surface roughness could be reduced to values closer to those of InAlN alone, as listed in Table IV. The higher flow also produced significant improvement in the XRD patterns as well, indicating an improvement in the crystal quality. The rough surface and poor structural quality at low nitrogen flow may indicate that growth has occurred under nitrogen deficient conditions, leading to the formation of In-rich regions in which 2D growth does not occur, see figure 6-3. Such behavior is also observed in other In-containing materials such as InAs. Given the improvement in structural quality and morphology, it is not surprising that increasing the nitrogen flow produced a pronounced reduction (~ 10X) in the contact resistance as well.

Further improvement in the contact resistance was obtained by increasing the growth temperature from 525°C to 575°C. This actually degraded the surface roughness slightly, as evidenced by the AFM surface roughness (shown in Table IV) and the SEM micrographs of figure 6-3. However, increasing the growth temperature reduced the as-deposited resistance by an order of magnitude by increasing both the carrier concentration and the mobility. Using these optimized growth conditions, contact

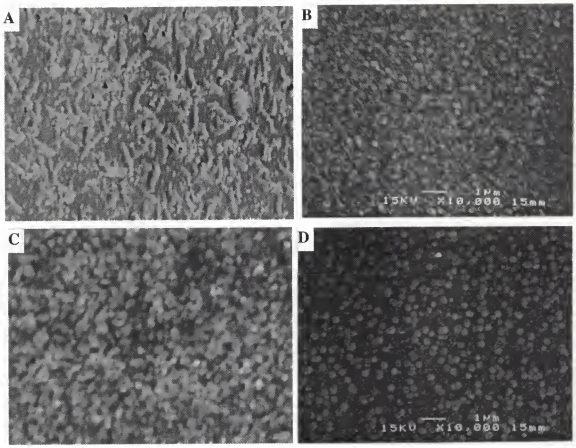


Figure 6-3. SEM micrographs at 10kX of contact stucture grown on sapphire at 525° C and 5 sccm $N_2$ (A), 525° C and 20 sccm $N_2$ (B) and 575° C at 20 sccm $N_2$ (C). Image D shows the effect of using an InN cap layer of 200 nm grown at 525° C and 20 sccm $N_2$. Lower $N_2$ flow rates or thicker cap layers show enhanced tendency toward islanding.

resistances as low as 3.5 x $10^{-6}$ $\Omega$-cm$^2$ were achieved, making these structures suitable for use in either digital or analog applications.

## 6.2 Thermal Stability of n-Type Contact Structures

This section reports on the thermal stability of InN contact stuctures similar to those discussed in 6.1.[78] Here, InN cap layers of 500, 1000, or 2000 Å were grown on InAlN films. Only sapphire substrates were used for this study, as this is more representative of industry standard. As with samples discussed in the previous section, a low T (400° C) 500 Å nucleation layer is deposited, followed by a 5000 Å AlN buffer grown at 700° C. InAlN is grown at 575° C, 3000 Å thick. Again, a graded layer is used between the InAlN and InN cap to mitigate band-offsets.

As shown in figure 6-4, the contact resistance of as-deposited contacts decreases substantially with increasing InN cap thickness up to 2000Å. While annealing of the 500Å structure produces a continual reduction in resistance over most of the range explored, annealing of the 2000Å structures does not appreciably change the electrical performance of the contact at temperatures up to 500°C. Interestingly, annealing at temperatures of 500° - 600°C produces roughly the same contact resistance for all of the InN thicknesses, suggesting that the contact resistance is being controlled by the formation of an interfacial layer at the contact/semiconductor interface or that the contact interface is being improved via intermixing at the interface.

AES analysis of 500Å InN annealed contacts provides some insight into the observed electrical behavior. From the profiles shown in figure 6-5, it would appear that the degradation in contact resistance after annealing at 700°C is most likely due to decomposition of the InN and subsequent diffusion of the In into the $WSi_x$. The contact

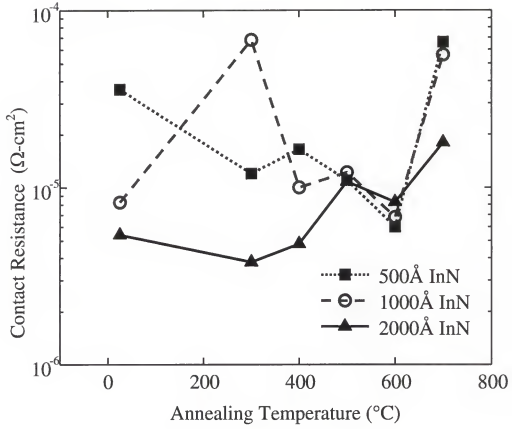


Figure 6-4. Contact resistance vs annealing temperature for structures having 500, 1000, or 2000 Å InN cap layers.

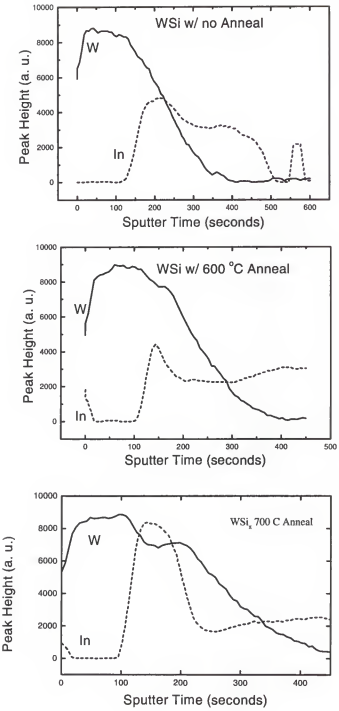


Figure 6-5. Depth profile AES curves of as grown structure (top), contact structure annealed at 600° C (middle), and contact structure annealed at 700° C (bottom).

structure in this case is now comprised of a $WSi_x$/AlInN junction which would be expected to exhibit a poorer contact resistance. Surprisingly, the sample annealed at 600°C does not indicate the formation of an interfacial layer as one might expect based on the reduction in the contact resistance relative to the as-deposited case. As seen in figure 6-5, there does however, appear to be some intermixing of the InN and the $WSi_x$ which could explain the improved contact resistance.

Unfortunately, while annealing at temperatures less than 700°C improves the electrical quality, it can have an adverse effect on the adhesion, which worsens as the InN thickness is increased. For 2000Å structures, even 400°C anneals cause some bubbling of the contact metal, as shown in figure 6-6. This behavior is similar to that observed for InAs-based contacts on GaAs, where increasing thickness has been shown to reduce the maximum allowable processing temperature. This may be due at least in part to the difference in lattice constant and thermal properties of InN relative to the underlying InAlN, and to the strong temperature dependence of the InN equilibrium nitrogen vapor pressure. The best compromise considering both performance and stability appears to be the use of 1000Å layers. This contact structure provided good electrical behavior both with and without annealing while good adhesion was maintained even at annealing temperatures up to 700°C.

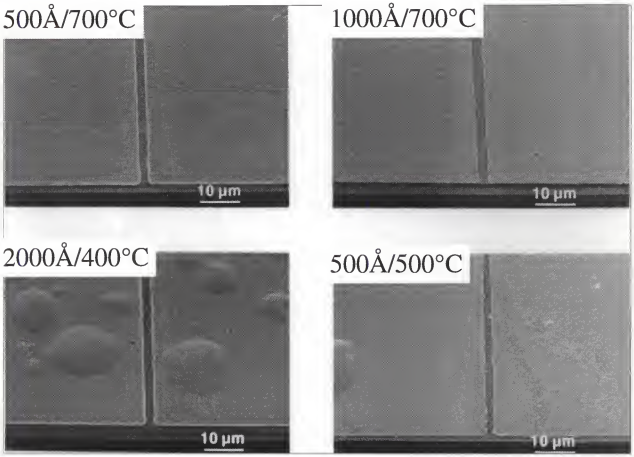


Figure 6-6. SEM micrographs of contact structures showing effect of annealing temperature and InN cap layer thickness on surface morphology: Top left, 500Å InN cap/ 700° C; top right, 1000 Å InN cap/ 700° C; bottom left, 2000 Å InN cap/ 400° C; bottom right, 500 Å InN cap/ 500° C.

# CHAPTER 7
# NITRIDE DEVICE DEVELOPMENT

This chapter discusses growth and fabrication of GaN/AlGaN heterojunction bipolar transistors (HBTs).[79] Wide bandgap semiconductor HBTs are attractive candidates for applications in high frequency switching, communications and radar. While field effect transistors can be used for these same applications,[80-82] HBTs have better linearity, higher current densities and excellent threshold voltage uniformity. The GaN/AlGaN system is particularly attractive because of its outstanding transport properties and the experience base that has developed as a result of the success of nitride based emitters and detectors.[83-85] GaN/AlGaN HBTs have been fabricated with a non-self-aligned, low damage dry etch process based on that developed for the GaAs/AlGaAs, GaAs/InGaP and InGaAs/AlInAs systems.[86]

Device structures were grown at SVT Assoc. using gas-source MBE and at Sandia National Labs using MOCVD. Processing steps including patterning and etching were conducted by the lab groups of Professor Stephen Pearton and Professor Fan Ren. An examination of two specific areas of concern, p-ohmic contacts and parasitic pre-reactions during MOCVD growth is made.

## 7.1 GaN/AlGaN HBT Growth

Structures grown by two different methods were examined. In the first, rf plasma-assisted MBE at a rate of ~0.5 $\mu m\text{-}hr^{-1}$ was used to grow the HBT structure on

top of a 2 μm thick undoped GaN buffer that was grown on c-plane (0001) sapphire. An 8000 Å thick GaN subcollector (Si ~$10^{18}$ $cm^{-3}$) was followed by a 5000 Å thick GaN collector (Si ~$10^{17}$ $cm^{-3}$), a 1500 Å thick GaN base (Mg acceptor concentration ~$10^{18}$ $cm^{-3}$), a 1000 Å thick $Al_{0.15}Ga_{0.85}N$ emitter (Si ~$5\times10^{17}$ $cm^{-3}$), and a 500 Å grade to a 2000 Å thick GaN contact layer (Si ~$8\times10^{18}$ $cm^{-3}$).

The second HBT structure was grown by MOCVD on c-plane sapphire, using trimethylgallium (TMG), trimethylaluminum (TMA) and ammonia as the precursors with high purity $H_2$ as the carrier gas. The basic layer structure is shown in Figure 7-1. Silane ($SiH_4$) and bis-cyclopentadienyl-magnesium ($Cp_2Mg$) were used for n- and p-type doping, respectively. A substrate temperature of 1050° C was used with reactor pressures of 140 torr for GaN and 80 torr for AlGaN layers. Separate p-GaN calibration samples were grown yielding hole concentrations of $7 \times 10^{17}$ $cm^{-3}$. A schematic of the MOCVD reactor is depicted in figure 7-2. Growth rates were ~1.4 μm/h for GaN and ~0.4 μm/h for AlGaN layers. The reduced growth rate of AlGaN results from gas-phase prereactions involving TMG, TMA and $NH_3$ that eliminate nutrients from the growth front. In an effort to elucidate the nature of this problem, a detailed examination of growth behavior was made using TMA and tritertiarybutylaluminum (t-$Bu_3Al$).

7.1.1 Comparison of Aluminum Precursors

It has been observed that the growth efficiency of GaN using TMG and $NH_3$ is comparable to that of GaAs grown in the same reactor.[87] However, the growth efficiency, defined as the growth rate divided by the group III molar flow rate, for AlN is seen to diminish with increased reactor pressure. In addition, gas phase adduct formation ($NH_3$:TMA) causes reduced incorporation efficiency for TMG as well.[88] Figure 7-3

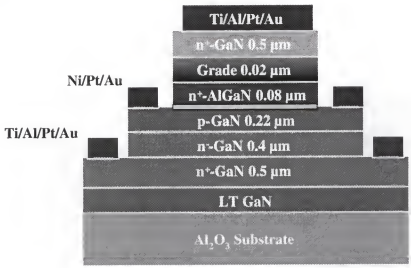


Figure 7-1. Schematic of MOCVD-grown GaN/AlGaN HBT

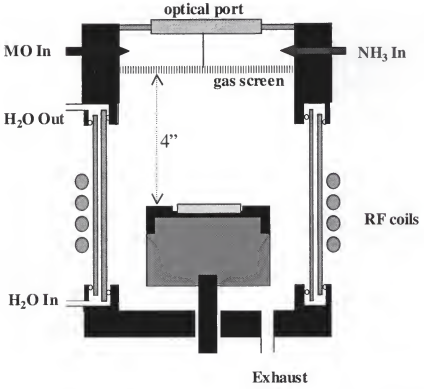


Figure 7-2. Schematic of MOCVD reactor used to grow GaN/AlGaN HBTs.

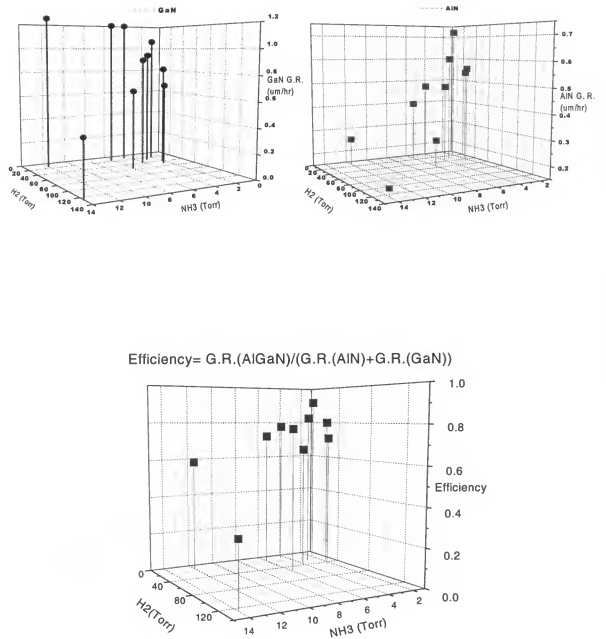


Figure 7-3. Growth efficiency of AlGaN at different gas compositions (bottom). The two top plots are for the binary alloys GaN (left) and AlN (right). As the NH3 pressure is increased, gas phase interactions reduce the growth efficiency of AlGaN. The TMG and TMA flux is held constant.

shows the reduction in AlGaN growth efficiency for fixed TMA and TMG flows with increasing $NH_3$. This result is possibly due to a surface site-blocking effect or a gas phase scavenging effect that sweeps out TMG before it has a chance to react at the growth surface.

In order to better understand this effect, a comparison of aluminum precursors was undertaken involving MOCVD growth of AlGaN with TMA or tritertiarybutylaluminum (t-$Bu_3Al$). Owing to its suitable vapor pressure (0.5 torr at 24° C) and its reported lack of prereaction with TMG, t-$Bu_3Al$ was selected as a potential replacement for TMA.[89] In addition, it is expected that t-$Bu_3Al$ will reduce C incorporation into the final film. SIMS data (figure 7-4) from the GaN/AlGaN HBT shows high incorporation rates of carbon, making metal-organic sources with reduced contamination potential much desired.

Samples of AlGaN were grown on 2" c-plane sapphire in an inductively heated rotating disc reactor at Sandia National Laboratories. A substrate temperature of 1050° C was used with an $NH_3$ flow of 3500 sccm and a TMG flow of 1.66 sccm at a reactor pressure of 80 torr to grow AlGaN films with varying TMA or t-$Bu_3Al$ flows. A hydrogen carrier gas was used to transport metalorganics to the reactor. An additional $H_2$ make-up flow of 4000 sccm is used to maintain reactor pressure.

The AlGaN growth rate is determined by optical reflectance spectroscopy that yields oscillations with a periodicity of $\lambda/2n$. Here, $\lambda$ = wavelength of the light probe and n = index of refraction for the film (interpolated between $n_{GaN} = 2.35$ and $n_{AlN} = 2.05$). Figure 7-5 reveals that the growth rate of AlGaN using TMA or t-$Bu_3Al$ decreases with increased Al fraction in the gas phase. Glancing incidence XRD is used to extract

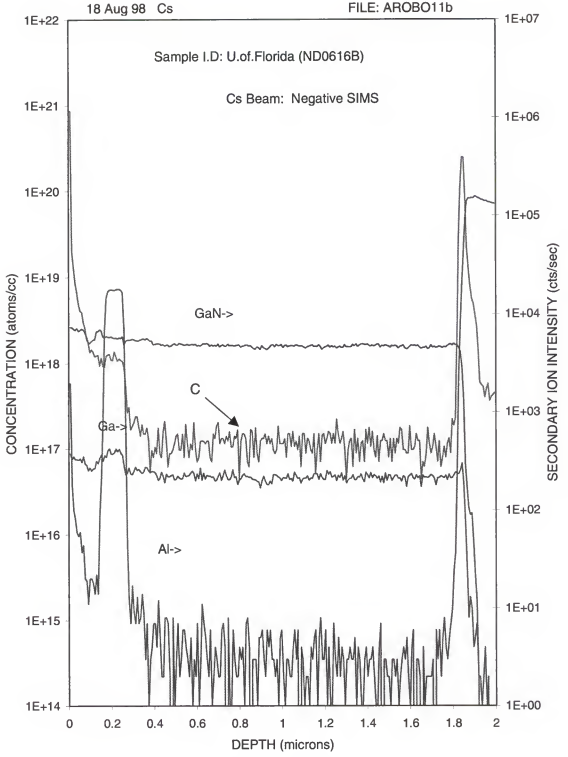


Figure 7-4. SIMS data showing level of C contamination in GaN/AlGaN HBT

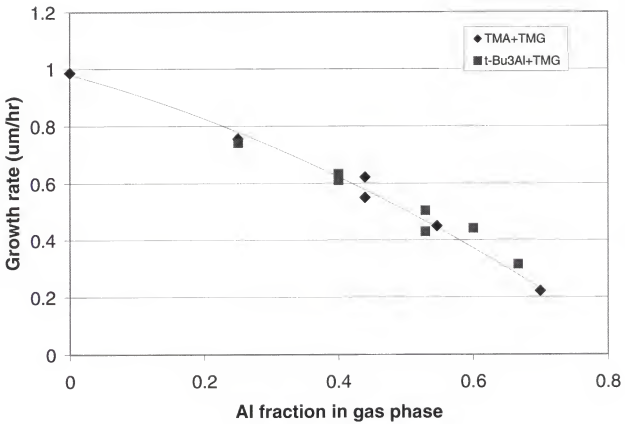


Figure 7-5. Al fraction in gas phase vs growth rate for AlGaN derived from TMA or t-$Bu_3Al$.

strained *c* and *a* lattice parameters for the hexagonal AlGaN films. From these values, an estimate of the unstrained lattice parameters is made using known elastic constants. Once these effective *c* and *a* values are determined, Vegard's Law can be invoked to obtain the Al fraction of the AlGaN. The Al fraction ending up in the film follows a sub-linear relationship with the Al fraction in the gas phase, as seen in figure 7-6. The results plotted in figures 7-5 and 7-6 imply that the TMA and t-$Bu_3Al$ behave similarly in the AlGaN growth environment. This result may be surprising owing to the differences in the physical geometry of the two precursors, compared in figure 7-7. One might expect the bulkier t-$Bu_3Al$ molecule to exhibit steric hindrance effects that would reduce its potential for adduct formation. However, Interante *et al.* report that both these Al precursors will react with $NH_3$ to form six-membered ring-like adducts containing three Al and three N atoms.[90] It should be noted that this earlier work was not done under MOCVD growth conditions but the adducts do easily decompose and readily form AlN crystallites.

Because of the similar growth behavior of TMA and t-$Bu_3Al$ and their known ability to form relatively large ring-like molecules when reacted with $NH_3$, it seems plausible that the mechanism responsible for the observed reduction in AlGaN growth rate is related to surface site blocking. If this were the case, however, it would be expected that the Al fraction in the final film would follow a super-linear dependence with Al fraction in the gas phase. The Al adduct would block the incorporation of TMG at the growth surface and preferentially incorporate itself. Data presented in figures 7-5 and 7-6 does not bear this scenario out. The data suggest that both the Al *and* Ga constituents are being prevented from incorporation for both types of Al precursor. This

implies a more complicated interaction between Al adducts and TMG that is not sensitive to differences in adduct geometry.

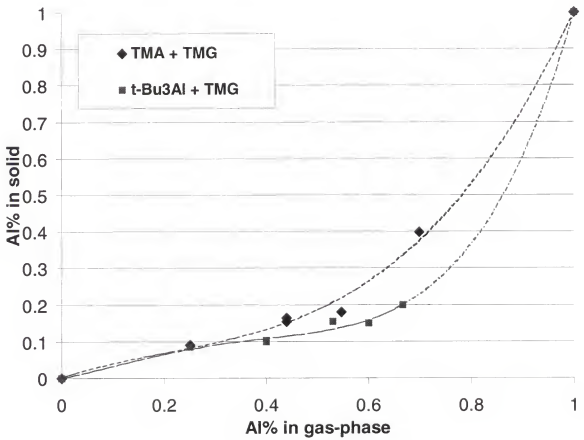


Figure 7-6. Al fraction in the gas phase vs Al fraction in the final AlGaN film.

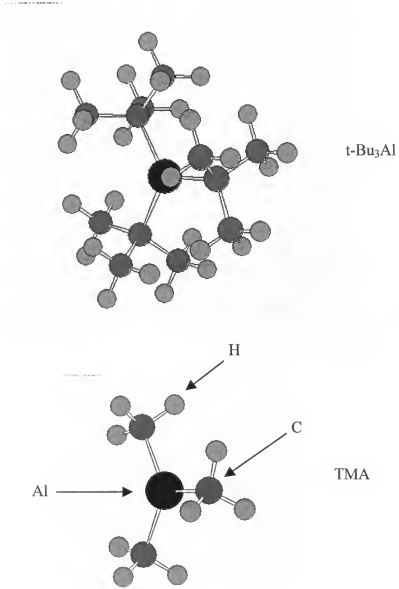


Figure 7-7. Models of t-$Bu_3Al$ and TMA.

An examination of SIMS data obtained from a special multilayer AlGaN structure fabricated using t-$Bu_3Al$ or TMA indicates the two Al sources contribute similar concentrations of C to the films, figure 7-8. Unexpectedly, the AlGaN layer derived from t-$Bu_3Al$ shows lower Si concentrations. This may be due to differences in residual Si contamination of the TMA and t-$Bu_3Al$ bubblers.

Although t-$Bu_3Al$ was reported to have no prereactions with TMG and potential for reduced C incorporation, the study done here indicates problems still exist. Another variable that may contribute to poor growth performance is reactor geometry. It may be necessary to experiment with various hardware configurations (especially gas inlets) to obtain optimized growth.

7.1.2 HBT Fabrication and Performance

The process flow for device fabrication is shown schematically in Figure 7-9. First the emitter metal (Ti/Al/Pt/Au) is patterned by lift-off and used as an etch mask for the fabrication of the emitter mesa. The dry etching was performed in a Plasma Therm 770 Inductively Coupled Plasma (ICP) system using $Cl_2$/Ar discharges. The process pressure was 5 mTorr, and the source was excited with 300 W of 2 MHz power. This power controlled the ion flux and neutral density, while the incident ion energy was controlled by application of 40 W of 13.56 MHz power to the sample chuck. Base metallization of Ni/Pt/Au was patterned by lift-off, and then the mesa formed by dry etching. The etch rate of GaN under these conditions was ~1100 Å-$min^{-1}$, and was terminated at the sub-collector where Ti/Al/Pt/Au metallization was deposited. The contacts were alloyed at 700-800 °C, as described later. Figure 7-10 shows scanning electron micrographs of the completed devices – the emitter diameter is ~90 μm.

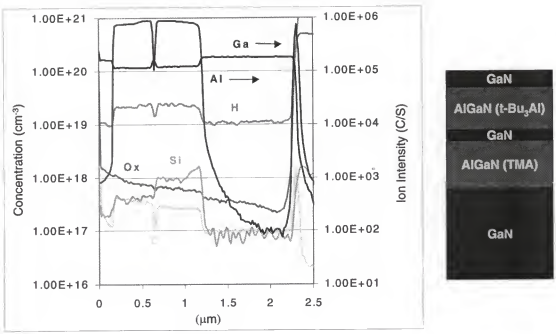


Figure 7-8. SIMS data for the multilayer stucture shown at right. The AlGaN derived from t-$Bu_3Al$ has lower [Si].

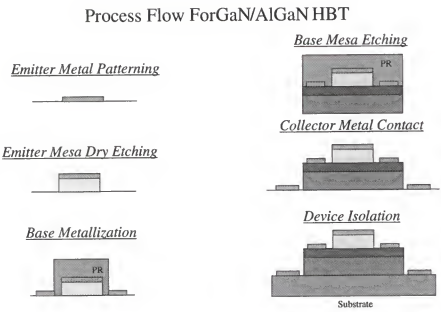


Figure 7-9. Schematic of process sequence for GaN/AlGaN HBT.

It has been firmly established that high specific contact resistivities are a limiting factor in GaN-based device performance, particularly those arising from the p-ohmic contact. The alloying temperature dependence of the current-voltage (I-V) characteristics for several different p-metal schemes was examined. A typical set of results is shown in figure 7-11 for Au/Ti/$WSi_x$/Ni and Au/Ti/$WSi_x$/Pd. Basically similar results were obtained for the Ni/Pt/Au, namely that the as-deposited contacts are rectifying. Annealing at progressively higher temperatures produced a significant improvement, but even for 800 °C anneals the contacts were not purely ohmic when measured at room temperature. This is consistent with past data, showing that p-metallization on GaN is

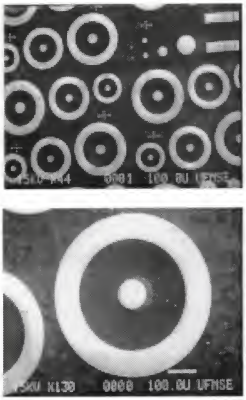


Figure 7-10. SEM micrographs of complete GaN/AlGaN HBT.

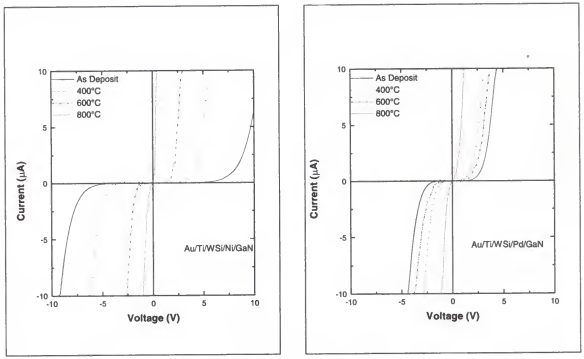


Figure 7-11. Annealing temperature dependence of I-V characteristics for Au/Ti/WSi/Ni and Au/Ti/WSi/Pd contacts on P-GaN.

often better described as a leaky Schottky contact. As the measurement temperature is increased, the hole concentration in the p-GaN increases through higher ionization efficiency of the Mg acceptors. For example the hole concentration would increase from ~10% of the acceptor density at 25 °C to ~60% at 300 °C, based on Fermi-Dirac statistics. Figure 7-12 shows that the p-contact becomes truly ohmic at ≥300 °C. This indicates that the GaN/AlGaN HBT will perform better at elevated temperatures, where the base contact resistivity is lower.

The device performance of both the MBE and MOCVD grown devices was similar, namely a gain of ≤3 at 25 °C, increasing to ~10 at 300 °C. A Gummel plot from the MBE device is shown in figure 7-13 and from the MOCVD device in figure 7-14. In both devices the performance was still limited by the base resistance, and methods to increase the base doping and lower the extrinsic resistance in this region will be critical for future efforts in this area. (See for example the I-V base characteristic from the MOVCD device in figure 7-15).

Another important aspect for the optimization of GaN/AlGaN HBTs is confinement of the Mg doping to the base. If the p-type spills over into the relatively lightly doped emitter, then the junction is displaced and the advantage of the heterostructure is lost. Figure 7-16 shows SIMS profiles of Mg in working devices from MOCVD (top) and MBE (bottom) material. The base layer is well defined in the MOCVD structure, while there is more incorporation of Mg into the overlying layers in the MBE sample. This may be a result of a higher Mg flux used for the MBE derived material. Also, the higher temperature associated with MOCVD may tend to volatilize segregated Mg during deposition of the base.

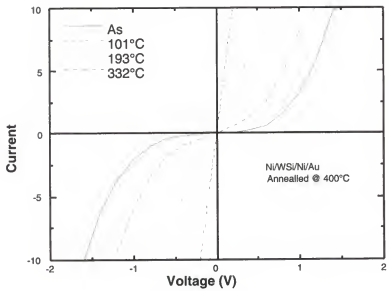


Figure 7-12. Measurement temperature dependence of I-V characteristics for Au/Ti/Wsi/Ni contact on p-GaN.

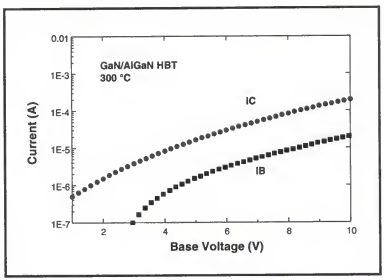


Figure 7-13. Gummel plot measured at 300° C for MBE GaN/AlGaN HBT.

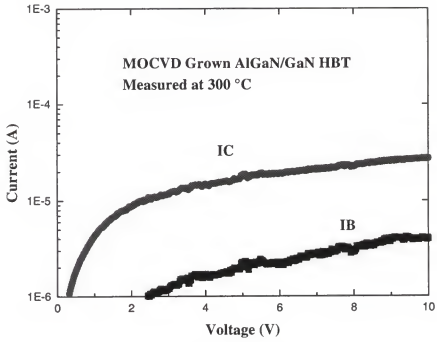


Figure 7-14. Gummel plot measured at 300° C for MOCVD GaN/AlGaN HBT.

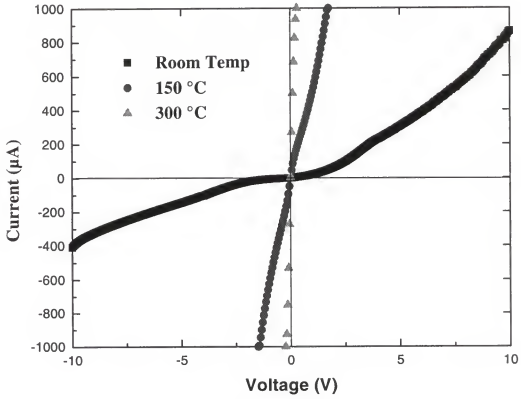


Figure 7-15. Base I-V ohmic contact characteristics on MOCVD device, as a function of measurement temperature.

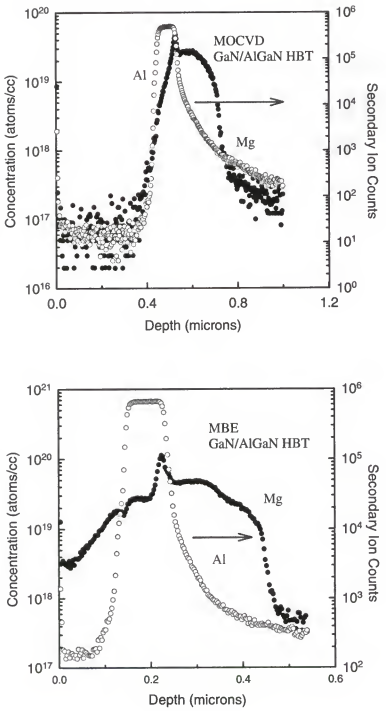


Figure 7-16. SIMS profiles of Mg in MOCVD (top) and MBE (bottom) GaN/AlGaN HBT structures.

Figure 7-17 shows SIMS profiles from a non-working device grown by MOCVD. Here, non-working implies that the gain was less than one due to high recombination rates in the base. In this case the Mg spill-over was more severe and compensated the emitter and emitter contact layers. These devices showed poor n-contact properties. Hydrogen concentrations of ~2-6×$10^{18}$ $cm^{-3}$ decorating the base region, as shown at right in the figure are typical. This is the case even after the in-situ activation anneal standard for all GaN device structures containing p-layers. It is assumed by analogy with the behavior of H in other compound semiconductor systems that this anneal dissociates the $(Mg\text{-}H)^{o}$ neutral complexes, producing $Mg^{-}$ acceptors and inactive $H_2$ molecules. Thus, while the hydrogen is still present at a significant concentration in the base, it is not in an active form, and does not effect the electrical properties.

In summary, GaN/AlGaN HBTs have been fabricated both on MBE and MOCVD grown material, and they display similar performance, i.e. a gain of ~10 when operated at ~300 °C. The fabrication process developed previously for other compound semiconductor systems works well for the GaN/AlGaN system, with the main difference being higher annealing temperatures required for the ohmic contacts. The device performance is still limited by the base doping for both MBE and MOCVD structures. It should be possible to improve device performance by using an ISL at the p-type base to lower its specific contact resistance. Since p-InN has not been achievable, an alternative ISL based on p-GaAs might hold promise. The next section presents work done to examine the feasibility of this approach.

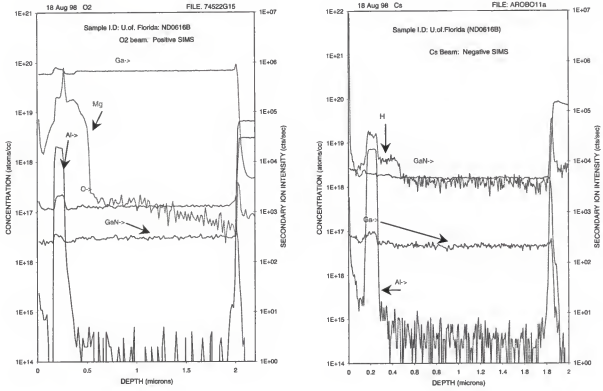


Figure 7-17. SIMS profiles showing Mg spill-over (left) and H (right) in an MOCVD GaN/AlGaN HBT structure.

## 7.2 P-Type Contact Layers Using GaAs

The band offsets of GaN and InN would suggest InN to be a perfect match for p-type contact layers to the larger-gap semiconductor. Unfortunately, as revealed in chapter five, p-InN does not seem to be obtainable with conventional growth techniques. This being the case, an alternative intermediate semiconductor layer for improved contact performance must be developed. GaAs is a logical candidate owing to its relatively small band-gap and amenability to p-doping.[91]

A calibration sample of GaAs:C was grown using triethylgallium (TEG) and arsine ($AsH_3$). The TEG, maintained at 9.3° C, was transported to the growth chamber using a He carrier gas flowing at 2.3 sccm at a bubbler pressure of 11.7 torr. An arsine flow of 2 sccm through a 1000° C cracker was used to provide an As flux. To induce p-type doping from carbon, carbon-tetrabromide ($CBr_4$) at 0° C and 65 torr was transported via a He carrier gas of 1.7 sccm. A semi-insulating GaAs substrate temperature of 600° C was used to grow 240 nm of epi-GaAs:C at 720 nm/hr. Room temperature Hall measurements indicate these conditions yield a hole concentration of $\sim 3 \times 10^{19}/cm^3$. Using e-beam deposited TiPtAu contacts, a transmission line method derived specific contact resistance of $\sim 14 \times 10^{-6}\ \Omega\text{-cm}^2$ was measured for this sample. All TLM measurements for this work were conducted at 250° C using 100 × 150 micron pads spaced 2, 4, 8, 16, and 32 microns apart, as shown in the SEM micrograph of figure 7-18. Mesas were etched in the GaAs using $HH_4OH:H_2O_2$ to prevent current spreading. After an RTA of 800° C for 15 s, $\rho_c$ for this sample was reduced to $\sim 6 \times 10^{-6}\ \Omega\text{-cm}^2$.

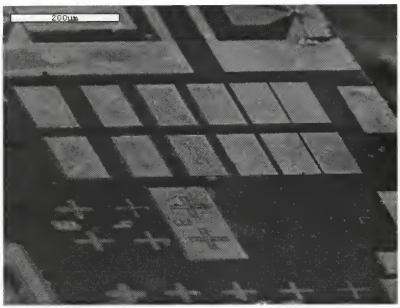


Figure 7-18. SEM micrograph of TLM pattern on GaAs/GaN structure.

A one micron thick layer of magnesium doped GaN deposited by MBE on sapphire was provided by SVT associates for p-GaAs contact deposition. NiAu contacts patterned for TLM yielded an unannealed $\rho_c$ of $8 \times 10^{-2}$ $\Omega$-cm$^2$ for the as-received p-GaN which was reduced to $4 \times 10^{-3}$ $\Omega$-cm$^2$ after annealing at 800° C for 15 s under flowing nitrogen. This surface was cleaned *ex situ* using an HCl dip followed by a UV-ozone treatment prior to loading into the MOMBE. Growth conditions for the GaAs:C heterolayer were the same as for the calibration sample except the He flow through the $CBr_4$ bubbler was increased to 6.8 sccm in order to maximize the hole concentration. A 120 nm contact layer was grown having $\rho_c = 7 \times 10^{-3}$ $\Omega$-cm$^2$. This value was reduced to $2 \times 10^{-3}$ $\Omega$-cm$^2$ after annealing. A summary of these results is presented in table VI.

Table VI. Specific contact resistance values for GaAs:C, GaN:Mg and GaAs:C/GaN:Mg, measured at 250° C.

| **Sample** | $\rho_c$ ($\Omega$-cm$^2$) **unannealed** | $\rho_c$ ($\Omega$-cm$^2$) **with 800° C anneal** |
|---|---|---|
| GaAs:C/GaAs | $14 \times 10^{-6}$ | $6 \times 10^{-6}$ |
| SVT GaN:Mg | $8 \times 10^{-2}$ | $4 \times 10^{-3}$ |
| GaAs:C/SVT GaN:Mg | $7 \times 10^{-3}$ | $2 \times 10^{-3}$ |

Although $\rho_c$ in the annealed sample was decreased slightly when the p-GaAs ISL was used, the expected degree of improvement was not observed. This may be due in part to the high oxygen concentration measured by SIMS at the GaAs/GaN interface. Residual oxygen may persist or reappear even though the GaN was cleaned with 1:1 HCl:$H_2O$ prior to loading into the growth chamber. The use of UV ozone cleaning may

generate such a thick oxide that the thermal deoxidation step was insufficient for its removal. Impurities such as oxygen may compensate acceptors or otherwise disrupt carrier transport leading to an increased $\rho_c$. Another area of concern originates from the high surface roughness found for the sample, as seen in the SEM micrograph of figure 7-19. The poor morphology is probably a result of surface roughness of the GaN:Mg, shown in the SEM micrograph of 7-19 and the difference in crystal structure between GaAs and GaN. Moreover, carrier transport across the GaAs/GaN interface is diminished as a result of the conduction band offset between the two layers. Figure 7-20 shows a schematic of the band offset that occurs for the two layers, including the effects of interface states that are likely to occur at highly mismatched interfaces such as this one. The valence band offset of ~1.8 eV has been determined from synchrotron-radiation photoemission spectroscopy by Ding *et al.*[92]

Typically, one would use a continuously graded ternary layer to ameliorate the effects of band offset between the GaN and GaAs. Unfortunately, the miscibility of the mixed group V species is very low, on the order of a few percent, disallowing growth of a graded layer. One way to circumvent the low miscibility problem is by fabricating a "digital alloy". This technique involves growing alternating layers of the two binary alloys, varying the relative thicknesses of the layers to approximate a graded layer. A schematic of this concept is depicted in figure 7-21. An attempt was made to generate such a structure using solid Ga, RF nitrogen plasma, $AsH_3$, and $Cp_2Mg$ as sources for the layers of p-GaN and p-GaAs. The structure contains 19 layers starting with ~ 4 Å GaAs on one micron of SVT GaN:Mg. The final layer is ~800 Å GaAs. Preliminary

indications imply that the electrical properties of the digital alloy structure are not improved over the SVT p-GaN alone.

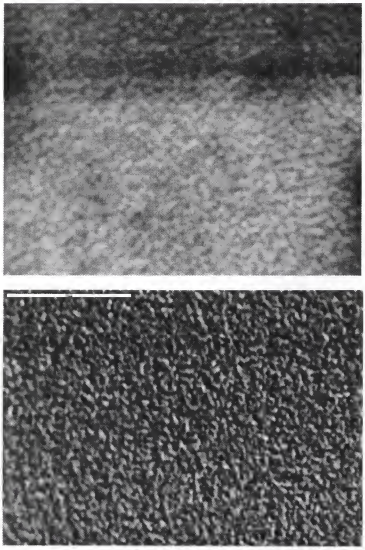

Figure 7-19. SEM micrographs at 10kX of as-received SVT GaN:Mg (top) and the GaAs:C/GaN:Mg contact structure (bottom). Surface roughness from the starting material translates to the epi-GaAs layer. The white bar represents 5 microns.

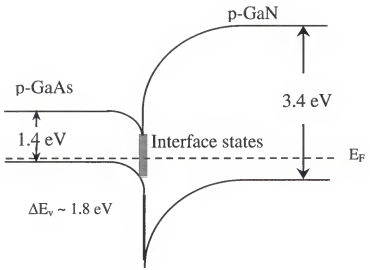


Figure 7-20. Schematic band diagram of p-GaN and p-GaAs heterostructure. Most of the off-set is accommodated by the GaN due to Fermi level pinning in the GaAs.

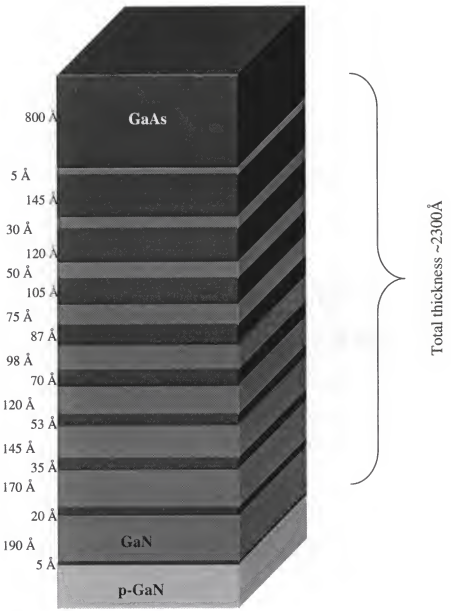


Figure 7-21. Schematic of digital alloy structure used to mitigate band offset between p-GaAs and p-GaN

# CHAPTER 8
# CONCLUSIONS, IMPLICATIONS, AND FUTURE WORK

The work done for this dissertation focused primarily on the growth of InN epitaxial films to serve as an intermediate semiconductor layer for improved ohmic contacts to nitride-based devices. As previously reported for growth of GaN,[93] a nitridation step prior to growth initiation was found to be essential for adequate InN epitaxial growth. The nucleation of an AlN buffer layer is facilitated by the presence of a nitridated layer in the substrate which leads to improved InN epitaxy. While oxygen backgrounds could be reduced through the use of solution TMI rather than solid TMI, it was discovered that high electron concentrations in the as-grown film persist regardless of nitrogen plasma condition, substrate type or In precursor used. Because of this, InN films are not suitable for p-type contact layers but have been shown to be suitable for n-type contacts possessing reasonable thermal stability.

An investigation of GaN/AlGaN HBTs was conducted. HBT operation measurements show that these devices have low gains at room temperature, typically $\leq 3$. As more acceptors in the base region become ionized with increased temperatures, base resistance is decreased and gain improves to ~ 10 at 300° C. Device performance is limited by base resistance and junction leakage. Contamination in the AlGaN emitter may contribute to junction leakage. MOCVD growth rates of GaN rapidly diminish with additions of the aluminum precursor TMA giving rise to increased contamination levels.

An examination of Al precursors indicate gas-phase adduct formation leads to complex interactions that inhibit nutrient arrival to the growth front. Solutions to this problem may include altering reactor geometry to limit gas-phase interactions or synthesis of novel Al precursors that are not susceptible to such interactions.

Attempts were made to develop improved p-type contacts based on p-GaAs layers. Unfortunately, the band offset between p-GaN and p-GaAs appears to preclude the use of a simple single-layer contact scheme. In addition, low miscibility between group V constituents necessitates the construction of a digital alloy to simulate a continuously graded layer. Results from early attempts indicate this is an area that requires additional work. Future efforts would identify optimal digital alloy layer thickness and quantity as determined by I-V measurements.

Ideally, ISL contact structures would be fabricated on actual devices. As other problems are addressed, such as Mg carry over into the emitter, integration of performance enhancing technologies can begin that will optimize nitride-based device operation.

The development of nitride based devices for high-temperature and high-power applications are in the earliest stages of evolution. The complexity of the problems facing researchers of nitride semiconductors requires a significant cross-disciplinary interaction including chemists, physicists, electrical engineers and materials scientists. Evidence of this can be found when perusing the many co-authors listed for most papers cited in the references of this work. Device optimization will proceed most efficiently by a parallel developmental approach. For example, research with individual aspects of device improvement such as thermally stable ohmic contacts should proceed concurrently with

optimization of device structure growth. As these separate endeavors lead to refinements, a fusion of these improvements will occur, leading to improved device performance. Continued gains in the understanding of nitride materials and nitride-based devices will necessitate further collaboration between numerous research groups.

Advancement of nitride-based devices is occurring at a remarkable rate even though progression comes via painstaking incremental steps. As these devices make their debut on the marketplace, consumers will have access to solid-state white-light emitters, high-density optical data storage devices and improved electric utility service. Military applications will include high temperature engine sensors, biohazard detectors and long-range field radios. Undoubtedly, as of yet unforeseen applications will emerge that benefit consumer, military and scientific needs. These advances will, in turn, lead to further improvements in research capabilities.

## REFERENCES


1. J. W. Mayer and S. S. Lau, *Electronic Materials Science: For Integrated Circuits in Si and GaAs*, Macmillan, New York (1990).

2. G. T. Heydt and B. J. Skromme, In *Mat. Res. Soc. Symp. Proc., Power Semiconductor Materials and Devices* **483**, 3 MRS Publishing, Warrendale, PA (1998).

3. S. J. Pearton, In *GaN and Related Materials*, p. 512, Gordon and Breach Science Publishers, Amsterdam (1997).

4. J. B. Casady and R.W. Johnson, *Solid-State Electron*. **39,** 1409 (1996).

5. N. Lovergine, P. Prete, G. Leo, L. Calcagnile, R. Cingolani, A. M. Mancini, F. Romanato, and A. V. Drigo, *Crystal Research and Technol*. **33**, 183 (1998).

6. S. Strite and H. Morkoc, *J. Vac. Sci. Technol*. B **10,** 1237 (1992).

7. S. Nakamura, Mater. Sci. Eng. B, *Solid-State Mater. Adv. Technol*. **50** (1-3) 277 (1997).

8. J. Han, M. H. Crawford, R. J. Shul, J. J. Figiel, M. Banas, L. Zhang, Y. K. Song, H. Zhou, and A. V.Nurmikko, *App. Phys. Lett*. **73**, 1688 (1998).

9. M. A. Khan, J. N. Kuznia, and A. R. Bhattatai, *Appl. Phys. Lett*. **62**, 1786 (1993).

10. EMRS 1997 Spring Meeting, Symposium L: *III-V Nitrides, Semiconductors and Ceramics: From Material Growth to Device Applications*, Elsevier, Amsterdam, (1998).

11. S. J. Pearton, R. J. Shul, E. Wolfgang, F. Ren, and S. Tenconi, Editors, *Mat. Res. Soc. Symp. Proc.* **483**, MRS Publishing, Warrendale, PA (1998).

12. S. J. Pearton, Editor *GaN and Related Materials*, Gordon and Breach Science Publishers, Amsterdam (1997).

13. L. L. Smith, R. F. Davis, M. J. Kim, R. W. Carpenter, and Y. Huang, *J. Mater. Res.* **11**, 2257 (1996).

14. M. Murakami and Y. Koide, In *Critical Reviews in Solid State and Materials Sciences*, **23** (1) p. 1-60 (1998).

15. J. S. Foresi and T. D. Moustakas, *Appl. Phys. Lett.* **62**, 2859 (1993).

16. M. E. Lin, Z. Ma, F. Y. Huang, Z. F. Fan, L. H. Allen, and H. Morkoc, *Appl. Phys. Lett.*, **64**, 21 (1994).

17. A. T. Ping, M. Asif Khan, and I. Adesida, *J. Elec. Mater.*, **25**, 819 (1996).

18. J. D. Guo, C. I. Lin, M. S. Feng, F.M. Pan, G. C. Chi, and C. T Lee, *Appl. Phys. Lett.* **68**, 235 (1996).

19. Z. Fan, S. Mohammad, W. Kim, O. Aktas, A. E. Botchkarev, and H. Morkoc, *Appl. Phys. Lett.* **68**, 1672 (1996).

20. M. W. Cole, D. W. Eckart, W. Y. Han, R. L. Pfeffer, T. Monahan, F.Ren, C. Yuan, R. A. Stall, S. J. Pearton, Y. Li, and Y. Lu, *J. Appl. Phys.* **80**, 278 (1996).

21. S. Miller and P. H. Holloway, *J. Elec. Mater.* **25**,1709 (1996).

22. L.L. Smith, R. F. Davis, M. J. Kim, R. W. Carpenter, and Y. Huang, *J. Mater. Res.* **11**, 2257 (1996).

23. Y. F. Wu, W. N. Jiang, B. P. Keller, S. Keller, D. Kapolnek, S. P. Denbaars, U. K. Mishra, and B.Wilson, *Solid-State Electron.* **41**,165 (1997).

24. C. B. Vartuli, S. J. Pearton, C. R. Abernathy, J. D. Mackenzie, M. L. Lovejoy, R. J. Shul, J. C. Zolper, A. G. Baca, M. Crawford, K. A. Jones, and F. Ren, *Solid-State Electron.* **41**, 531 (1996).

25. J. T. Trexler, S. J. Pearton, P. H. Holloway, M. G. Mier, K. R. Evans, and R. F. Karlicek, *Mater. Res. Soc. Proc., III-V Nitrides* **449**, 1091(1997).

26. Y. Koide, H. Ishikawa, S. Kobayashi, S. Yamasaki, S. Nagai, J. Umezaki, M. Koike, and M. Murakami, *Appl. Surf. Sci.* **117-118**, 373 (1997).

27. H. Ishikawa, S. Kobayashi, Y. Koide, S. Yamasaki, S. Nagai, J. Umezaki, M. Koike, and M. Murakami, *J. Appl. Phys.* **81**, 1315 (1997).

28. T. Mori, T. Kozawa, T. Ohwaki, Y. Taga, S. Nagai, S. Yamasaki, S. Asami, N. Shibata, and M. Koike, *Appl. Phys. Lett.* **69**, 3537 (1996).

29. D. J. King, L. Zhang, J. C. Ramer, S. D. Hersee, and L. F. Lester, *Mater. Res. Soc. Proc., GaN and Related Materials* **468**, 421 (1997).

30. T. Kim, K. Jinseok, C. Suhee, and T. Kim, *Mater. Res. Soc. Proc., GaN and Related Materials* **468**, 427 (1997).

31. M. C. Yoo, J. W. Lee, J. M. Myoung, K. H. Shim, and K. Kim, *Mater. Res. Soc. Proc., III-Nitrides, SiC and Diamond Materials for Electronic Devices* **423**, 131(1996).

32. T. Kim, M. C. Yoo, and K. Taeil, *Mater. Res. Soc. Proc., III-V Nitrides* **449**, 1061 (1997).

33. J. M. Woodall, J. L. Freeouf, G. D. Petit, T. N. Jackson, and P. Kirchner, *J. Vac. Sci. Technol.* **19**, 626 (1981).

34. C. H. Chen, H. Liu, D. Steigerwald, W. Imler, C. P. Kuo, M. G. Crawford, M. Ludowise, S. Lester, and J. Amano, *J. Electr. Materials* **25**, 1004 (1996).

35. J. W. Mathews and A. E. Blakeslee, *J. Cryst. Growth* **27**, 118 (1974).

36. D. Lide, Editor, *Handbook of Chemistry and Physics*, CRC Press, Boston (1990).

37. H. Kroemer, In *Molecular Beam Epitaxy and Heterostructures*, ed. L. L. Chang and K. Ploog, NATO ASI Series E, No. 87, Matinus Nijhoff, Dordrecht, The Netherlands (1985).

38. J. D. MacKenzie, PhD Dissertation, Univ. of Florida, Gainesville (1998).

39. P. van der Wagt, *http://snowmass.stanford.edu/*, Harris Group Web Page, Stanford Univ. (1996).

40. S. M. Sze, *Physics of Semiconductor Devices*, John Wiley & Sons, New York (1981).

41. M. W. Wang, J. O. McCaldin, J. F. Swenberg, T. C. McGill, and R. J. Hauenstein, *Appl. Phys. Lett.* **66**, 1974 (1995).

42. H. J. Hovel and J. J. Cuomo, *Appl. Phys. Lett.* **20**, 71 (1972).

43. T. L. Tansley and C. P. Foley, *Electronics Lett.* **20** (25/26), (1984).

44. B. T. Sullivan, R. R. Parsons, K. L. Westra, and M. J. Brett, *J. Appl. Phys.* **64**, 4144 (1988).

45. T. Matsuoka, H.Tanaka, T. Sasaki, and A. Katsui, from *Int. Symp. GaAs and Related Compounds*, Karuizwa, Japan, (1989).

46. T. J. Kistenmacher, S. A.Ecelberger, and W. A. Bryden, *J. Appl. Phys.* **74** (3) (1993).

47. S. Strite, D. Chandrasekhar, J. D. Smith, J. Sariel, H. Chen, N. Teraguchi, and H. Morkoc, *J. Crystal Growth* **127**, 204 (1993).

48. Y. Sato and S. Sato, *J. Crystal Growth* **146**, 262 (1995).

49. S. M. Donovan, J. D. MacKenzie, C. R. Abernathy, S. J. Pearton, P. C. Chow, and J. van Hove, *J. Electr. Matls.* **26**, 1292 (1997).

50. O. Brandt, H. Yang, B. Jenichen, Y. Suzuki, L. Daweritz, and K. H. Ploog, *Phys. Rev. B* **52**, 2253 (1995).

51. M. E. Lin, G. Xue, G. L. Zhou, J. E. Green, and H. Morkoc, *Appl. Phys. Lett.* **63**, 932 (1993).

52. T. Lei, M. Fanciulli, R. J. Molnar, T. D. Moustakas, R. J. Graham, and J. Scanlon, *Appl. Phys. Lett.* **59**, 944 (1991).

53. H. J. Lee, H. Ryu, C. R. Lee, and K. Kim, *J. Crystal Growth* **191**, 621 (1998).

54. T. S. Cheng, L. C. Jenkins, S. E. Hooper, C. T. Foxon, J. W. Orton, and D. E. Lacklison, *Appl. Phys. Lett.* **66**, 1509 (1995).

55. S. M. Donovan, J. D. MacKenzie, C. R. Abernathy, S. J. Pearton, P. Holloway, F. Ren, J. M. Zavada, and B. Chai, *Gallium Nitride and Related Materials II*. Materials Research Society Symposium, San Francisco, CA, April 1997.

56. R. G. Wilson, B. L. H. Chai, S. J. Pearton, F. Ren, P. Wisk, *J. Vac. Sci. Technol.* **B11**, 179 (1993).

57. A. Yamamoto, M. Tsujino, M. Ohkubo, and A. Hashimoto, *J. Crystal Growth* **137**, 415 (1993).

58. S. Denbaars, In Electrochemical Society Meeting, Los Angeles, 1996.

59. T. L. Tansley and R. J. Egan, *Physical Review B* **45**, 942 (1992).

60. D. W. Jenkins and J. D. Dow, *Physical Review B* **39**, 3317 (1989).

61. J. H. Oh, F. Fukuchi, H. C. Kang, and M. Konagi, *J. Crystal Growth* **164**, 425 (1996).

62. T. J. deLyon, J. M. Woodall, P. D. Kircher, D. T. MacIntruff, G. J. Scilla, and F. Cardone, *J. Vac. Sci. Technol.* **B9**, 136 (1991).

63. T. P. Chin, P. D. Kirchner, J. M. Woodall, and C. W. Tu, *Appl. Phys. Lett.* **59**, 2865 (1991).

64. T. Yamada, *J. Crystal Growth* **95**, 145 (1995).

65. J. M. van Hove, P. P. Chow, M. F. Rosamond, G. L. Carpenter, and L. A. Chow, *J. Vac. Sci. Technol.* **B12**, 1200 (1994).

66. C. R. Abernathy, J. D. MacKenzie, W. S. Hobson, and P. W. Wisk, *Appl. Phys. Lett.* **65**, 2205 (1994).

67. M. Spencer, In Fall Meeting of the Materials Research Society, Boston, MA (1995).

68. C. R. Abernathy, J. D. MacKenzie, S. J. Pearton, and W. S. Hobson, *Appl. Phys. Lett.* **66**, 1969 (1995).

69. W. Schoenfeld, M. J. Antonell, J. Choi, and C. R. Abernathy, In *Proceedings of the 27th State of the Art Program on Compound Semiconductors,* Electrochem. Soc., Pennington, NJ (1997).

70. C. R. Abernathy, J. D. MacKenzie, S. R. Bharatan, K. S. Jones, and S. J. Pearton, *Appl. Phys. Lett.* **66**, 1632 (1995).

71. H. Ito, K. Kurishima and N. Watanabe, *J. of Crystal Growth* **158**, 430 (1996).

72. M. Copel, M. C. Reuter, E. Kaxiras, and R. M. Tromp, *Phys. Rev. Lett.* **63**, 632 (1989).

73. N. Grandjean, J. Massies, and M. Leroux, *Appl. Phys. Lett.* **69**, 2071 (1996).

74. S. M. Donovan, J. D. MacKenzie, C. R. Abernathy, S. J. Pearton, F. Ren, K. Jones, and M. Cole, *Appl. Phys. Lett.* **70**, 2592 (1997).

75. S. E. Hooper, C. T. Foxon, T. X. Cheng, L. C. Jenkins, D. E. Lacklison, J. W. Orton, T. Bestwick, A. Kean, M. Dawson, and G. Duggan, *J. Crystal Growth*, **155** 157 (1995).

76. M. E. Lin, G. Xue, G. L. Zhou, J. E. Greene, and H. Morkoc, *Appl. Phys. Lett.* **63** 932 (1993).

77. F. Ren, C. B. Vartuli, S. J. Pearton, S. M. Donovan, J. D. Mackenzie, R. J. Shul, J. C. Zolper, M. L. Lovejoy, A. G. Baca, M. Hagerott-Crawford, and K. A. Jones, *J. Vac. Sci. Technol.* A **15** (1997).

78. S. M. Donovan, J. D. MacKenzie, C. R. Abernathy, S. J. Pearton, F. Ren, K. Jones, and M. Cole, *Solid-State Electron.* **42**, 1831 (1998).

79. F. Ren, J. Han, R. Hickman, J. M. Van Hove, P. P. Chow, J. J. Klaassen, J. R. LaRoche, K. B. Jung, H. Cho, X. A. Cao, S. M. Donovan, R. F. Kopf, R. G. Wilson,

A. G. Baca, R. J. Shul, L. Zhang, C. G. Wilson, C. R. Abernathy, and S. J. Pearton, submitted to *Solid-State Electron.* (1999).

80. J. C. Zolper, *Solid-State Electron.* **42**, 2153 (1998).

81. M. S. Shur and M. A. Khan, in *High Temperature Electronics*, pp 297-321, ed. M. Willander and H. L. Hartnagel, Chapman and Hall, London (1996).

82. E. R. Brown, *Solid-State Electron.* **42**, 2119 (1998).

83. See for example S. Nakamura, *IEEE J. Selected topics in Quantum Electron.* **3**, 345 (1997).

84. S. Nakamura, M. Senoh, S. Nagahama, N. Iwasa, T. Yamada, T. Matsushita, Y. sugimoto, and H. Kiyoku, *Appl. Phys. Lett.* **70**, 616 (1997).

85. J. M. Van Hove, R. Hickman, J. J. Klaassen, P. P. Chow, and P. P. Ruden, *Appl. Phys. Lett.* **70**, 282 (1997).

86. F. Ren, J. R. Lothian, S. J. Pearton, C. R. Abernathy, P. W. Wisk, T. R. Fullowan, B. Tseng, S. N. G. Chu, Y. K. Chen, L. W. Yang, S . T. Ru, R. S. Brozovich, H. H. Lin, C. L. Henning, and T. Henry, *J. Vac. Sci. Technol.* **B 12**, 2916 (1994).

87. C. H. Chen, H. Liu, D. Steigerwald, W. Imler, C. P. Kuo, M. G. Crawford, M. Ludowise, S. Lester, and J. Amano, *J. Electron. Mater.* **25**, 1004 (1996).

88. J. Han, J. J. Figiel, M. H. Crawford, M. A. Banas, M. E. Bartram, R. M. Biefeld, Y. K. Song, and A. V. Nurmikko, *J. Crystal Growth* **195**, 291 (1998).

89. A. C. Jones and P. O'Brien, in *CVD of Compound Semiconductors*, VCH, Weinheim, Germany (1997).

90. L. V. Interrante, G. A. Sigel, M. Garbauskas, C. Hejna, and G. Slack, *Inorg. Chem.* **28**, 252 (1989).

91. G. T. Dang, A. P. Zhang, F. Ren, S. M. Donovan, C. R. Abernathy, W. S. Hobson, S. N. G. Chu, X. A. Cao, R. G. Wilson, and S. J. Pearton, submitted to *Solid- State Electron.* (1999).

92. S. A. Ding, S. R. Barman, K. Horn, H. Yang, B. Yang, O. Brandt, and K. Ploog, *Appl. Phys. Lett.* **70**, 2407 (1997).

93. S. Keller, B. P. Keller, Y. F. Wu, B. Heying, D. Kapolnek, J. S. Speck, U. K. Mishra, and S. P. DenBaars, *Appl. Phys. Lett.* **68**, 1525 (1996).

## BIOGRAPHICAL SKETCH

Sean Donovan was born here in Gainesville on Nov. 23, 1967, Thanksgiving day. After moving up and down the eastern U. S. including a transfer from Athens, GA, to Arlington, MA prior to his senior year of highschool, a track scholarship brought him back to Gainesville and the University of Florida. An unusual undergraduate career started poorly with academic probation being imposed after freshman year. Improvements were demonstrated while in the College of Health and Human Performance but undercurrents of academic and athletic dissatisfaction preceded a switch to the College of Engineering and a farewell to the track team after three years. A bewildering academic progression then led to a Bachelor of Science with high honors from the Materials Science and Engineering Department in Dec. 1992, and subsequent enrollment at the Massachusetts Institute of Technology.

Slightly longer than two years were then sacrificed at MIT working on a woefully misguided, poorly conceived project involving GaAs growth on Si. This provided impetus for a second return to Gainesville and the miraculous discovery of Prof. Cammy Abernathy's lab group.

Under her watch, Sean developed professionally by attending several conferences and authoring or co-authoring more than 20 publications. A semester at Sandia National Labs in Albuquerque, NM, during the fall of '98 was an invaluable experience as well.

With the advantage of Prof. Abernathy's insightful guidance over the past 4+ years, Sean hopes to find gainful employment while not besmirching the professor's immaculate and richly deserved reputation.

I certify that I have read this study and that in my opinion it conforms to acceptable standards of scholarly presentation and is fully adequate, in scope and quality, as a dissertation for the degree of Doctor of Philosophy.

Cammy R. Abernathy, Chairperson
Professor of Materials Science and Engineering

I certify that I have read this study and that in my opinion it conforms to acceptable standards of scholarly presentation and is fully adequate, in scope and quality, as a dissertation for the degree of Doctor of Philosophy.

Stephen J. Pearton
Professor of Materials Science and Engineering

I certify that I have read this study and that in my opinion it conforms to acceptable standards of scholarly presentation and is fully adequate, in scope and quality, as a dissertation for the degree of Doctor of Philosophy.

Stan Bates
Associate Engineer of Materials Science and Engineering

I certify that I have read this study and that in my opinion it conforms to acceptable standards of scholarly presentation and is fully adequate, in scope and quality, as a dissertation for the degree of Doctor of Philosophy.

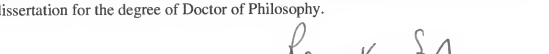

Rajiv K. Singh
Professor of Materials Science and Engineering

I certify that I have read this study and that in my opinion it conforms to acceptable standards of scholarly presentation and is fully adequate, in scope and quality, as a dissertation for the degree of Doctor of Philosophy.

Fred Sharifi
Associate Professor of Physics

This dissertation was submitted to the Graduate Faculty of the College of Engineering and to the Graduate School and was accepted as partial fulfillment of the requirements for the degree of Doctor of Philosophy.

December 1999

M. J. Ohanian
Dean, College of Engineering

Winfred M. Phillips
Dean, Graduate School

LD
1780
1999
D687